MANIPULATION OF OPTICAL COUPLING BETWEEN PLASMONIC NANOCAVITIES AND 2D EXCITONS

LO TSZ WING

PhD

The Hong Kong Polytechnic University

2021

The Hong Kong Polytechnic University
Department of Applied Physics

Manipulation of optical coupling between plasmonic nanocavities and 2D excitons

LO TSZ WING

A thesis submitted in partial fulfillment of the requirements for the degree of Doctor of Philosophy

July 2020

CERTIFICATE OF ORIGINALITY

I hereby declare that this thesis is my own work and that, to the best of my knowledge and belief, it reproduces no material previously published or written, nor material that has been accepted for the award of any other degree or diploma, except where due acknowledgement has been made in the text.

_____ (Signed)

Lo Tsz Wing (Name of student)

Abstract

The large binding energies of excitons (up to 500 meV) in two-dimensional (2D) transition metal dichalcogenides (TMDCs) enable thermally robust excitonic responses even at room temperature, which is highly desired for many optoelectronic applications. In particular, the hexagonal lattice of 2D TMDCs exhibits strong spin-orbital coupling (SOC) and inversion symmetry breaking, which gives rise to pronounced valley coherence for important valleytronic applications.

The strong SOC and inversion symmetry breaking in TMDCs also results in energy splitting of their conduction bands (CBs), leading to the existence of optically bright (X_O) and dark intra-valley excitons (X_D). The bright excitons originate from the combination of electrons and holes with antiparallel spins, and can be coupled directly with in-plane polarized photons. On the other hand, the dark excitons originate from the combination of electrons and holes with parallel spins, and have a near-zero in-plane dipole moment and thus a considerably longer lifetime than bright excitons, resulting in an optically inactive property under conventional normal-incidence illumination. Despite these fascinating optical properties, the low quantum yield (QY) of photoluminescence (PL) in TMDCs has significantly limited their optical and optoelectronic applications. Many studies have discovered that defect-mediated non-radiative recombination restricts the QY of pristine exfoliated TMDC monolayers (ML) to ~1 %.

In this thesis, by coupling various plasmonic nanostructures with 2D TMDCs, I discovered and discriminated different physical mechanisms responsible for the nanoscale light-matter interaction between 2D excitons and plasmonic nanocavities, and achieved significantly enhanced PL from both bright and dark excitons. Firstly, I studied the strong coupling phenomena between single gold core-silver shell nanocuboids (Au@Ag NC) and the bright excitons of WS_2 and MoS_2 monolayers under thermal tuning. By fitting the temperature-dependent dark-field scattering spectra of the Au@Ag-WS_2 and Au@Ag-MoS_2 systems with a classical coupled oscillator model (COM), I observed that the thermal evolution of their coupling strengths were opposite. Such a counter-intuitive observation revealed an indirect coupling channel between the plasmon mode of the Au@Ag NC and the bright and dark excitons of WS_2 and MoS_2, which is often ignored in previous studies on TMDC-based plasmon-exciton coupling interactions.

Secondly, I employed a gold (Au) nanoparticle-on-mirror (NPoM) nanocavity to enhance the PL emission of bright excitons and explored the enhancement mechanism. In this study, a CVD-grown MoS_2 ML was transferred to an alumina (Al_2O_3)-coated gold mirror through a standard wet transfer method, and the sample was then covered with another Al_2O_3 layer before drop-casting of Au nanospheres to form Al_2O_3–MoS_2–Al_2O_3-sandwiched Au NPoM nanocavities. The thicknesses of both Al_2O_3 spacers were precisely controlled by the number of cycles of atomic layer deposition (ALD) to

optimize the plasmon-enhanced PL from MoS_2, showing a 7-fold PL intensity enhancement at 5 nm thick Al_2O_3. Finite-difference time-domain (FDTD) simulations were conducted to quantify the contribution of plasmonic near-field enhancement, antenna efficiency and Purcell effect on the enhanced bright exciton emission.

Lastly, I used a single plasmonic NPoM nanocavity to induce significant radiation from the spin-forbidden dark excitons of WSe_2 at room temperature, and unravelled an interesting mechanism based on polarization-dependent plasmon-exciton coupling. In this study, the NPoM nanocavity was utilized to sandwich a mechanically exfoliated pristine WSe_2 ML that supported a higher-lying bright exciton state and a lower-lying dark exciton state. To ensure the formation of a compact NPoM nanocavity, a template-stripped gold film was used to as a flat metal mirror supporting good adhesion with a WSe_2 ML, which strongly quenched the bright exciton emission but, in the meanwhile, largely enhanced the dark exciton emission when coupled to an Au nanosphere on top. The sample was then exposed to directional argon ion bombardment in an inductively charged plasma (ICP-RIE) etching machine. Since the metal nanoparticle functioned as a shadow mask to shelter the underlying WSe_2 ML during the etching process, only the WSe_2 outside the nanoparticle region was removed. PL spectroscopic measurements of the etched system showed that the PL intensity from the dark excitons was comparable with the bright excitons when resonantly interacting with the gap plasmon cavity mode. I used a double-Lorentz fitting on the PL spectra, suggesting a 60 meV energy difference between these two excitonic states. The numerical aperture (NA) dependent

PL and enhanced radiation decay rate unambiguously verified the out-of-plane dipole nature of the dark exciton states.

The results presented in this thesis provide an effective paradigm for manipulating the electromagnetic coupling between surface plasmons and 2D excitons through ultra-compact plasmonic nanocavities at room temperature. This study paves way for further understanding the excitonic dynamics of 2D TMDCs and employing them in quantum information and nanoscale optoelectronic devices.

List of Publications and Conference Presentations

Journal publications based on this thesis work:

(# equally contributed, * corresponding author)

1. **Lo, T. W.**#; Zhang, Q.#; Qiu, M.; Guo, X.; Meng, Y.; Zhu, Y.; Xiao, J. J.; Jin, W.; Leung, C. W.; Lei, D. Y.* "Thermal Redistribution of Exciton Population in Monolayer Transition Metal Dichalcogenides Probed with Plasmon–Exciton Coupling Spectroscopy." ***ACS Photonics*** 2019, 6, 411–421.
2. Qi, X.; **Lo, T. W.**; Liu, D.; Feng, L.; Chen, Y.; Wu, Y.; Ren, H.; Guo, G.; Lei, D. Y.*; Ren, X.* "Effects of Gap Thickness and Emitter Location on the Photoluminescence Enhancement of Monolayer MoS_2 in a Plasmonic Nanoparticle-Film Coupled System." ***Nanophotonics*** 2020, 9, 2097–2105.
3. **Lo, T. W.**; Chen, X.; Zhang, Q.; Leung, C. W.; Lei, D.* "Plasmonic brightening of dark excitons in monolayer WSe_2 with single metallic particle-on-mirror nanocavity at room temperature." ***To be submitted*** 2021.

Journal publications during my PhD study but not included in this thesis:

1. Xu, C.; Chen, Y.; Cai, X.; Meingast, A.; Guo, X.; Wang, F.; Lin, Z.; **Lo, T. W.**; Maunders, C.; Lazar, S.; et al. "Two-Dimensional Antiferroelectricity in Nanostripe-Ordered In_2Se_3." ***Phys. Rev. Lett.*** 2020, 125 (4), 47601.

2. Ou, W.; Zhou, B.; Shen, J.; **Lo, T. W.**; Lei, D. Y.; Li, S.; Zhong, J.; Li, Y. Y.; Lu, J.* "Thermal and Nonthermal Effects in Plasmon-Mediated Electrochemistry at Nanostructured Ag Electrodes." ***Angew. Chemie Int. Ed.*** 2020, 59 (17), 6790–6793.
3. Chen, P.; **Lo, T. W.**; Fan, Y.; Wang, S.; Huang, H.; Lei, D. Y.* "Chiral Coupling of Valley Excitons and Light through Photonic Spin – Orbit Interactions." ***Adv. Opt. Mater.*** 2020, 1901233, 1–22.
4. Xu, Y.; **Lo, T. W.**; Zhang, L.; Lei, D. Y.* "The Preparation, Characterization and Application of Ultra-Smooth, Low-Loss Plasmonics Noble Metal Films." ***Sci. Sin. Phys. Mech. Astron.*** 2019, 49 (12), 124206.
5. Yip, C. T.#; **Lo, T. W.**#; Zhu, S.; Jia, G. Y.; Sun, H.; Lam, C.; Lei, D. Y.* "Tight-Binding Modelling of Excitonic Response in van Der Waals Stacked 2D Semiconductors." ***Nanoscale Horizons*** 2019, 4, 969–974.
6. Gan, X.; Zhao, H.; **Lo, T. W.**; Ho, K. H. W.; Lee, Y. S. L.; Lei, D. Y.*; Wong, K.* "2H/1T Phase Transition of Multilayer MoS_2 by Electrochemical Incorporation of S Vacancies." ***ACS Appl. Energy Mater.*** 2018, 1, 4754–4765.
7. Ho, K. H. W.; Shang, A.; Fenghua, S.; **Lo, T. W.**; Yeung, P. H.; Yu, Y. S.; Zhang, X.; Wong, K.; Lei, D. Y.* "Plasmonic Au/TiO_2-Dumbbell-On-Film Nanocavities for High-Efficiency Hot-Carrier Generation and Extraction." ***Adv. Funct. Mater.*** 2018, 28, 1800383.
8. Zhang, Q.; Li, G. C.; **Lo, T. W.**; Lei, D. Y.* "Polarization-Resolved Optical Response of Plasmonic Particle-on-Film Nanocavities." ***J. Opt. (United Kingdom)*** 2018, 20 (2), 024010.

9. Liu, J.; **Lo, T. W.**; Sun, J.; Yip, C. T.; Lam, C. H.; Lei, D. Y.* "A Comprehensive Comparison Study on the Vibrational and Optical Properties of CVD-Grown and Mechanically Exfoliated Few-Layered WS_2." ***J. Mater. Chem. C*** 2017, 5 (43), 11239–11245.

Acknowledgments

During my four-year PD study, many people support me to overcome all the challenges.

First of all, I would like to express my sincere thanks to my first supervisor Dr. Dangyuan Lei who provided me the opportunity to pursue my PhD study in PolyU, and he provided me comprehensive guidance to my research study. Also, I was able to learn multidiscipline knowledge ranging from condensed matter physics to plasmonic nanophotonics, as Dr. Lei has many fruitful discussions with me. I would also like to say thank you to my second supervisor Dr. Chi Wah Dennis Leung. He provided me much technical support and research advices in the last year of my PhD study.

Besides, I would like to express my sincere gratitude to all my collages. Dr. Qiang Zhang and Dr. Meng Qiu have provided me much theoretical understanding and modelling of the experimental results to enrich the discussion. Dr. Cho Tung Yip, Dr. Guang-Can Li, Dr. Yulong Fan, Mr. Kwun Hei Willis Ho, Mr. Yongjun Meng, Mr. Peigang Chen, and Mr. Jin Liu have collaborated with me to perform various experiments from nonlinear optics to photothermal effects. It extends my knowledge based on a wide range of research studies.

Lastly, I would like to express my sincere thanks to my family and they are just so important to me. Their endless love and support shelter me from all thunderstorms.

Without my family, I couldn’t stand for those tough moments in my PhD study.

Table of Contents

Chapter 1 Introduction and Literature Review

1.1 Coupling Regime Between Quantum Emitter and Cavity

The coupling between quantum emitters (QE) and photons depends on not only the intrinsic properties of QE but also the surrounding photonic environment that modifies the local density of state (LDOS) of the optical field experienced by the QE[1,2]. Fermi's golden rule in quantum optics denotes that the density of coupled photon state justifies the probability of absorbing\emitting photons during the atomic-vacuum coupling[1]. Consequently, resonant cavities that exhibit intense LDOS at resonant frequency manifest a wide range of optical phenomena and applications.

In the weak coupling regime, where the energy exchanging rate is slower than the dissipation of the modes, the spontaneous radiative decay rate of QE is altered by the photonic structure (Figure 1.1 (a) and (b))[3]. Through proper engineering of the photonics systems, both acceleration of emission and suppression of radiation in the on-resonant cavity and off-resonant cavity photonics systems can be realized, respectively[3]. The acceleration of QE radiation in optical cavity was firstly recognized by Purcell in 1940s[1,4,5]. He revealed that a resonant optical cavity with the same resonance as QE's emission supports intense LDOS at the cavity resonant

frequency which promotes the radiative relaxation of QE. This famous Purcell enhancement equation $F = 3/(4\pi^2)\lambda^3 Q/V$ quantitively reflects that high quality factor (Q-factor) and small mode volume are two crucial elements to facilitate the interaction between the optical cavity and QE for accelerating the radiative decay of QE. Interestingly, even though Purcell description fails on a strong coupling regime, the Q-factor and mode volume relation on strong coupling are still valid even in this condition[6].

In the strong coupling condition, where the energy exchange rate is considerably higher than the dissipation of the modes, two distinct hybridized modes that possess coherent and reversible oscillations between light and matter states are formed (Figure 1.1 (c) and (d)). The spectral distinction of hybridized states is termed vacuum Rabi splitting. Those nonclassical modes, which exhibit partial light modes (low nonlinearity and high transportability) and partial matter states (high nonlinearity and low transportability) features, realize the novel and anomalous phenomena such as Bose-Einstein condensates[7,8], nonlinear optical switching[9], and polariton lasers[10–12]. These quantum properties open new ways of photonics applications such as single photon switches and quantum computing, etc. In recent years, manipulating the photonic environment of quantum emitters in the strong coupling regime to control the potential landscape has been recognized in realizing many intriguing light-driven nanochemistry phenomena[13].

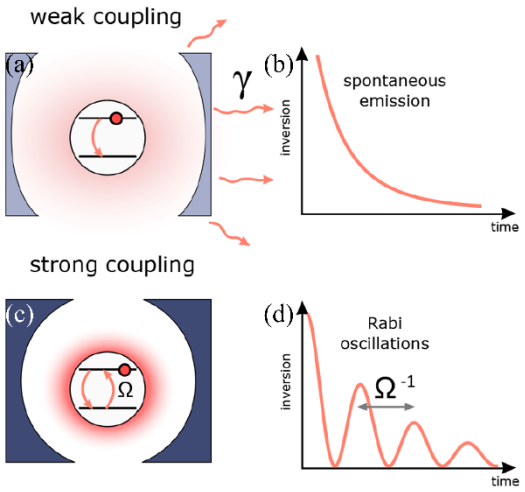

Figure 1.1 (a) Schematic representation of a dielectric optical cavity coupled with QE in weak coupling condition, the energy has been dissipated into surrounding bath before finishing the oscillation between two modes; (b) Population of the QE state under the spontaneous emission condition; (c) Schematic diagram of an optical cavity coupled with QE in strong coupling condition, EM oscillation between the QE and cavity occurs before energy dissipation; (d) Population of the QE state under the Rabi oscillation[3].

To facilitate the coupling between photons and matter in visible and near infrared range, a high Q-factor dielectric cavity was firstly utilized to optimize the photon-matter interaction time between before the optical field dissipation. Several previous studies, including distributed Bragg reflector (DBR) microcavity[7,8] or defects in photonics crystal[14], have already demonstrated the realization of strong coupling with QE such as quantum dots (QD). With the constraint of dielectric cavities, the modal volume of the light field has been restricted to the size of the diffraction limit. The demanding low loss cavity and emitters usually request cryogenic condition to suppress the intrinsic loss of both modes. Those issues constrain the size of cavities, operation temperature, and bandwidth of cavities, which restrict the potential functionality such as nanochemistry manipulation[13],

etc.

Plasmonic cavities, which shrunk light deeply beyond the diffraction light, have become one of the research focuses on light-matter interaction in recent years. Even the wider bandwidth of plasmon modes exhibits larger energy loss in both radiation and ohmic loss. The radiative dominated losses (~50%) in plasmonic cavity[15] provide better extraction of the photon from the nanocavities which is highly desirable for nano-optics application. The broader linewidth of plasmon mode also furnishes certain flexibility of variation in QE's resonance frequency. Meanwhile, the ultra-small mode volume of plasmonic cavities indicates less demand on low loss cavities and QE, which is highly desirable for realizing strong coupling even at room temperature conditions for unusual applications such as nanochemistry manipulation[13].

1.2 Surface Plasmon Polariton

Surface plasmon polariton (SPP), a coupled mode of optical field and collective oscillation of free electrons, is confined at the interface between metal and dielectric material. Benefited from the bosonic surface wave nature of SPP, the local field is strongly confined at the interface beyond the diffraction limit and decays exponentially along the surface normal. This property attains intense near-field enhancement which magnifies diverse optical phenomena, including surface-enhanced photoluminescence or surface-enhanced Raman scattering (SERS).

Through solving the Maxwell equation with boundary condition across the interface between semi-infinite dielectric metal and dielectric material, the famous classical dissipation relation of SPP mode is obtained as following:

$$k_{\mathrm{SPP}} = \frac{\omega}{c}\sqrt{\frac{\varepsilon_1 \varepsilon_2}{\varepsilon_1 + \varepsilon_2}}$$

(Eq. 1.1)

Where k, ω, c, ε_1 and ε_2 denote the momentum of SPP, frequency of SPP, speed of light, the permittivity of metal, and permittivity of dielectric, respectively. We consider the dielectric medium as air and the metal's properties as described by Drude model:

$$\varepsilon = 1 - \frac{\omega_p^2}{\omega^2}$$

(Eq. 1.2)

We can derive an analytical solution of dispersion relation for SPP as shown:

$$\omega^2 = c^2 k^2 + \frac{\omega_p^2}{2} + \sqrt{c^4 k^4 + \frac{\omega_p^4}{4}}$$

(Eq. 1.3)

From the above equation, the dispersion relation of SPP demonstrates dramatic distinction with the dispersion relation of propagation photon in free space, as shown in Figure 1.2 (a). Under certain conditions with the conservation of momentum, a resonant absorption of light is realized (Figure 1.2 (b) and (c)). At small momentum regime, the dispersion relation of SPP is in proximity with the light cone such that the LDOS is limited at those frequencies. At the large

momentum regime, the dispersion curve of SPP rapidly bends toward the value of $\omega_P/\sqrt{2}$ which implies significant LDOS for various optical phenomena.

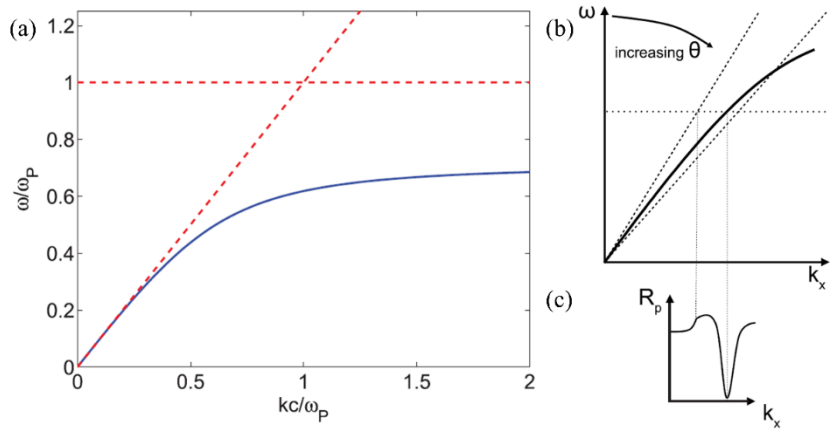

Figure 1.2 (a) Dispersion relation of SPP along the planar surface between air and Drude metal; (b) Dispersion relation of SPP under the incident angle tuning; (c) The corresponding reflectance at a certain frequency as shown in (b)[16].

It is worth noting that the dispersion relation of SPP is always beyond the light cone in the same dielectric medium. Based on Noether's theory, the violation of momentum conservation between light in dielectric and SPP at the same plane indicates that direct coupling between incident electromagnetic wave in dielectric and SPP is unrealizable along a translational symmetric surface. Consequently, several schemes, including near-field coupling, prism coupling, and grating coupling have been proposed to achieve momentum matching.

1.3 SPP Coupling Scheme

Prism coupling, which employs the evanescent wave from the total internal reflection inside the prism, accomplishes the momentum matching condition between the light propagation and SPP[16]. In the Otto scheme[17], as shown in Figure

1.3 (a), a single prism is placed slightly above a metal substrate with an air gap. When the light is incident on the prism/air interface, total internal reflection occurs. The evanescent component of the total internal reflected wave is capable of decaying through the air gap and excite SPP at air/metal interface. Considering the larger momentum of propagating light in a prism, the coupling between those light mode and SPP mode is accomplishable at a certain incident angle for momentum matching[17]. In Kretschmann scheme[18], as demonstrated in Figure 1.3 (b), thin metal mirror is directly deposited on prism surface to form prism/metal interface. Likewise, the total internal reflection induces an evanescent wave that exponentially decays through the thin metal mirror. SPP at the adjacent metal/air interface is then excited by the evanescent wave[18].

Grating coupling utilizes the periodicity of grating to alter the corresponding dispersion relation of SPP for momentum matching with propagating light wave[19]. Similar to the electronic band structure of the crystal, SPP in grating exhibits periodic dispersion relation, as illustrated in Figure 1.3 (c)[16]. The periodicity of the dispersion is defined by the reciprocal of grating geometry as $G = 2\pi/a$[20]. This periodic dispersion relation further results in opposite extrema at the adjacent SPP bands that open up the bandgap in the dispersion relation. The extrema, which shows zero slope at the dispersion relation, implies an intense optical density of state.

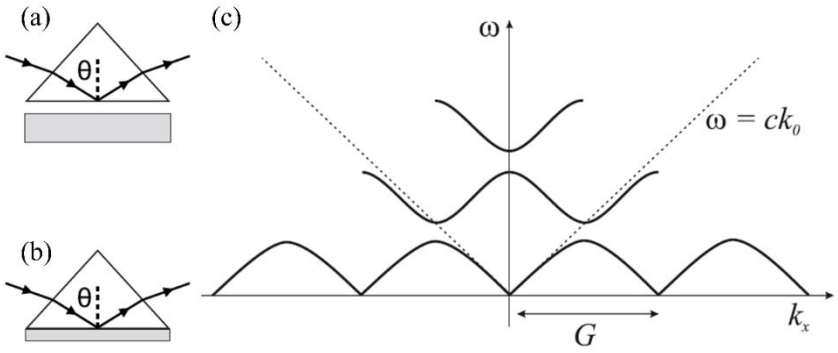

Figure 1.3 (a) Schematic diagram of Otto schemed prism coupling; (b) Schematic diagram of Kretschmann schemed prism coupling; (c) Dispersion relation of SPP in grating coupling. The dashed line denotes the dispersion relation of light cone[16].

1.4 Localized Surface Plasmon Resonance

Metallic nanostructure in subwavelength scale, which traps light and focuses it in a localized region, sustains localized surface plasmon resonance (LSPR)[21,22]. Owing to the breaking of transitional symmetry of nanostructure, LSPR of the nanostructure is free to couple with propagating light wave without considering the momentum conservation issue. More intriguingly, since the scattering/extinction cross section of a plasmonic structure at LSPR is even larger than the actual geometric cross section, light-matter interaction is strongly facilitated by the highly confined field[21,22]. The most fundamental resonance of LSPR is the electric dipole resonance that mimics half-wavelength resonance in the optical cavity. The local field of the plasmonic cavity is confined at the two ends to form hot spots which extends only in tens of nm. Through plasmon hybridization (which will be discussed in the next session) of these antennas pairs, plasmonic hot spots are even able to be shrunk into nm scale.

Among different optical resonances in various geometries, only the spherical and cylindrical nanostructures have analytical solutions in the corresponding optical spectra. Mie resonances of a metallic nanosphere, an elementary series of LSPR, provides an intuitive insight in unveiling the nature of LSPR[23]. Based on the multipole expansion on Mie's theory (as shown in Figure 1.4), the optical features of nanosphere/nanocylinder including scattering, extinction and absorption can be expressed as a series of superposition of various resonance modes as[23]:

$$C_{sca} = \frac{2\pi}{k}\sum_{n=1}^{\infty}(2n+1)(|a_n^2| + |b_n^2|)$$

(Eq. 1.4)

$$C_{ext} = \frac{2\pi}{k}\sum_{n=1}^{\infty}(2n+1)(Re(a_n) + Re(b_n))$$

(Eq. 1.5)

$$C_{abs} = C_{ext} - C_{sca}$$

(Eq. 1.6)

The scattering, extinction and absorption coefficients are termed C_{sca}, C_{ext} and $C_{abs,}$ respectively. The coefficients a_n and b_n, which are obtained from resolving the boundary conditions of the spherical or cylindrical nanostructures, indicate the fraction of N^{th} optical resonance in the corresponding responses at a certain wavelength.

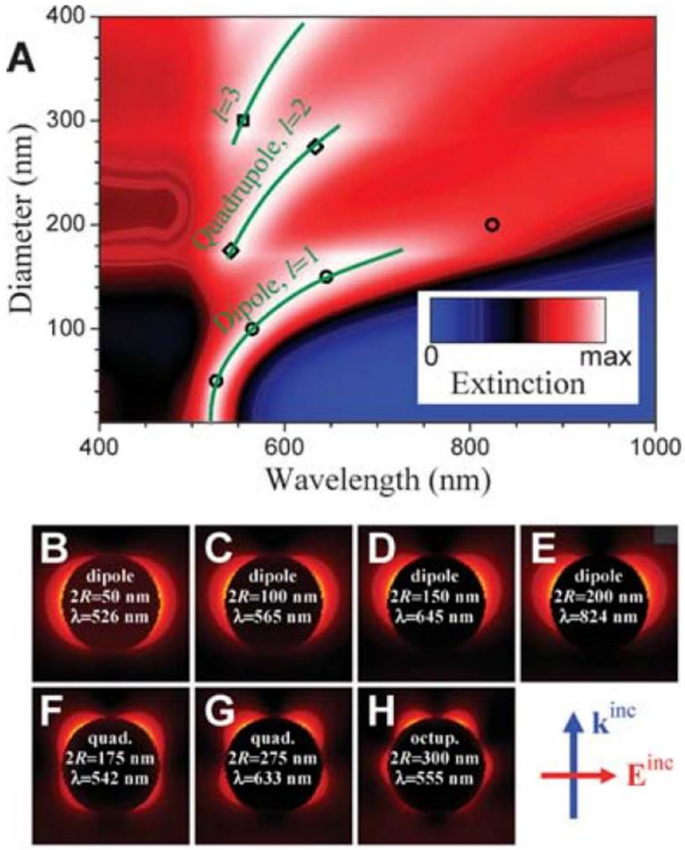

Figure 1.4 (a) Extinction spectrum of gold nanospheres with diameter evolution from 0 to 400 nm compared with the prediction of Mie's theory; (b-h) Near field distribution of gold nanospheres with different sizes and resonances[23].

Over the past decades, the Mie scattering theory has been generalized to core-shell nanospheres[24] or multiple-layered nanocylinders[25], which preserve the same symmetry properties as nanospheres and cylindrical structures. It is also extended to lattice systems (e.g. periodic nanospheres or cylinders systems) to unveil the potential in studying lattice systems. Even the classical electromagnetic responses of different nanostructures are fully described by Maxwell equations. Finding all the analytical solutions for LSPR in all optical systems is unrealizable and inefficient in actual applications. Numerical methods, including finite element

method (FEM) and finite-difference time-domain method (FDTD), have been developed to discretize Maxwell's equations for solving an approximate solution in integral form or time domain for studying the optical phenomenon of different nanostructures.

To capture the insight of LSPR, quasi-static approximations have been employed to study the optical resonance phenomenon in noble metal nanospheres. Following the long wavelength and small particle assumption ($a/\lambda \ll 1$), the nanosphere structure experiences an optical field that can be approximated as a uniform static electric field. In this quasi-static picture, the corresponding polarizability of the excited nanosphere can be analytically resolved as[21]:

$$\alpha = 4\pi a^3 \frac{\varepsilon_1 - \varepsilon_2}{\varepsilon_1 + 2\varepsilon_2}$$

(Eq. 1.7)

Through resolving the polarizability, the scattering cross section and absorption cross section can be directly expressed as:

$$C_{sca} = \frac{k^4}{6\pi}|\alpha|^2 = \frac{8}{3}\pi k^4 a^6 \left|\frac{\varepsilon_1 - \varepsilon_2}{\varepsilon_1 + 2\varepsilon_2}\right|^2$$

(Eq. 1.8)

$$C_{abs} = k\, Im(\alpha) = 4\pi k a^3 Im\left(\frac{\varepsilon_1 - \varepsilon_2}{\varepsilon_1 + 2\varepsilon_2}\right)$$

(Eq. 1.9)

From the above equations, it can be observed the clear resonance features when the dielectric constants of metal and dielectric obey the famous $\varepsilon_1 = -2\varepsilon_2$ relation. This emphasizes the importance of LSPR in strong interaction with light.

1.5 Plasmon Hybridization

To further tailor plasmonic properties for different functionalities, engineering the plasmonic nanostructures through plasmon coupling has been proposed. Owning to the strong Coulomb interaction between nearby plasmonic structures, the modes of individual nanostructure are significantly perturbed by the coupling process while the structures are in proximity. In 2004, Peter Nordlander analogized the EM coupling between plasmon modes in each nanostructure as the quantum interaction of electron cloud in nearby atoms in his plasmonic hybridization model.[26] Considering the dimer nanoparticles system (which mimics a two-atom system) in the hybridization model, the same dipole modes in individual nanoparticles hybridize into bonding and anti-bonding modes, which are the in-phase and anti-phase coupling of the original eigenmodes (Figure 1.5) [27]. This manifests superradiant and nonradiant characteristics in the above hybridized plasmonic modes respectively. The superradiant mode is also termed the bright mode which exhibits significant net dipole moment for radiative coupling with plane wave in free space. Besides the optically active nature of the bright mode, the plasmonic hot spot in between the gap of dimer structures is one of the most facilitating properties in dimer structure. Upon the resonant excitation of superradiant mode, an external field larger than geometric cross section is shrunk into an ultrasmall mode volume, which serves as a compact nanocavity for promoting light-matter interaction.

The nonradiant mode is frequently named as a dark mode that carries zero net

dipole moment. Due to the nearly zero-dipole moment, the dark plasmon mode is inactive towards plane wave excitation. However, some special approaches, such as electron beam focusing, evanescent wave and vector beam, can also realize the excitation of such a dark mode[28]. The plasmonic hybridization model is also generalized to multiple nanostructures coupling or even lattice-plasmon systems for revealing an intuitive physical picture of modes interaction[29].

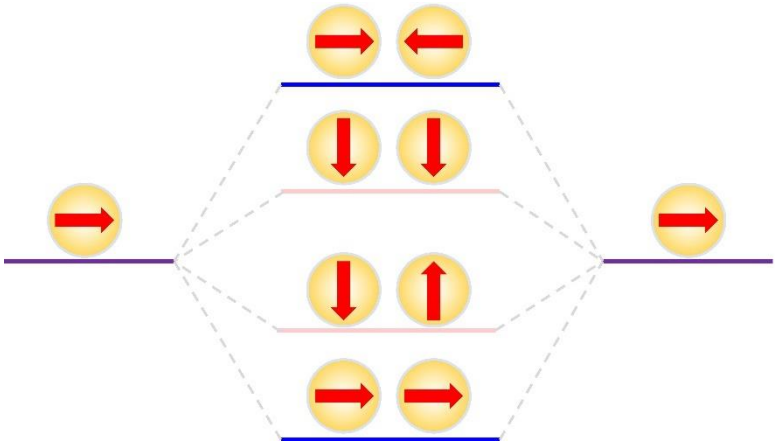

Figure 1.5 Hybridization model of dimers through the longitudinal and transverse coupling.

To capture the insight of the plasmon hybridization model, the EM coupling phenomenon between the dimer nanospheres under the concept of model is revealed. In the plasmon hybridization model, the conduction electrons are considered as incompressible charged liquid, which are bounded by a uniform geometrically defined positive charge ion core background as described in the Jellium model[30]. This plasmon hybridization model is linked to only instantaneous electrodynamics response, which is valid on the deep sub-wavelength scale system. Under the hydrodynamics model, the resonance of intrinsic plasmon modes in metallic nanosphere is expressed as:

$$\omega = \omega_p \sqrt{\frac{l}{2l+1}}$$

(Eq. 1.10)

where ω_p and l correspond to bulk plasmon frequency and angular momentum of spherical harmonic such as dipolar (l = 1) and quadrupole (l = 2), etc. In general, those eigen plasmon modes can hybridize with each other to form different mixing modes. The energy detuning between eigen plasmon modes suppresses the hybridization phenomenon between hetero plasmon modes. By considering only the plasmon hybridization in eigen dipole modes (l = 1) in dimer, the dipole modes are either polarized along the dimer axis or perpendicular to it. For the case of dimer axis parallel to the polarized dipole modes, the strong EM coupling induces large energy splitting in the bonding mode and anti-bonding mode. For dimer axis perpendicular to the polarized dipole modes, the relatively weak EM coupling prompts small energy splitting in the bonding mode and anti-bonding mode.

1.6 Functionality of Metal Nanoparticle on Mirror (NPoM) System

As mentioned previously, with the dual (or multiple) nanostructures neighboring each other, a localized plasmonic hot spot is formed inside the gap regime. This plasmonic hot spot yields significant localized field enhancement or LDOS which amplifies various optical phenomena like surface enhanced Raman scattering (SERS)[31–33], surface enhanced photoluminescence (PL)[34] and even strong plasmon exciton polariton coupling (plexciton)[6,35]. With the limitation of current electron beam lithography technologies, the edge-to-edge spacing between dimers can only

be narrowed down to sub-10 nm regimes which restricts the confinement of plasmonic hot spot (Figure 1.6 (a) and (b))[36]. As a result, metal nanoparticle on mirror (NPoM) has been proposed to replace lithographic dimer structure own to the capability of realizing sub-nm scale gap as shown in Figure 1.6 (c) and (d)[37]. In this section, the properties of NPoM are further discussed to reveal the origin of gap plasmon in NPoM.

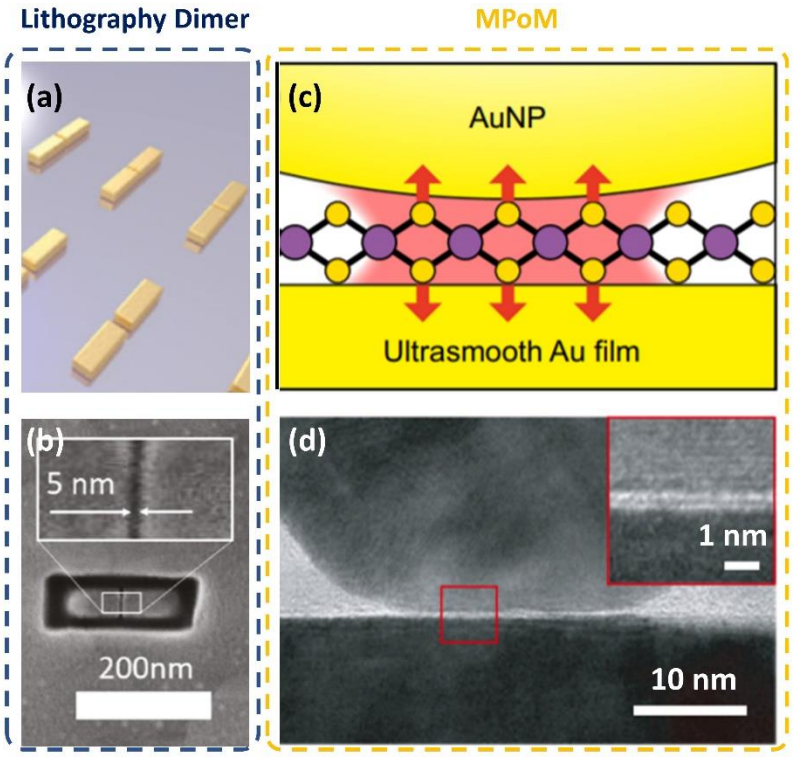

Figure 1.6 (a) Schematic diagram of lithography dimer structures; (b) SEM images of the lithography dimer structures[36]; (c) Schematic diagram of NPoM structure with WSe_2 spacer; SEM images of the NPoM structure[37].

When a metallic nanoparticle stands on top of the metallic mirror and exhibits plasmon oscillation, image charge oscillation is sequentially induced at the metallic mirror and couples back with the original plasmon mode in metallic

nanoparticle[38,39]. Under far-field excitation, transverse mode and vertical gap mode are typically featured[40–42]. Distinguished from the transverse mode which manifests transverse antibonding mode, the gap plasmon mode displays plasmonic hot spot[43]. The potential of utilizing the ultrasmall nanocavity in the gap mode of NPoM is the key feature of NPoM structure. A precise deposing optical active material such as QE, photochromic molecule[44] (Figure 1.7 (a)), thermoresponsive polymer[45] (Figure 1.7 (b)) and even two dimensional (2D) material[35] (Figure 1.7 (c)) has been envisioned at the heart of fundamental cavity quantum electrodynamics (CQED), optical switching, nano actuator and surface plasmon amplified stimulated emission of radiation (spaser) applications. In this perspective, in comparison with other chemically synthesized dimer structures, NPoM presents self-assemble properties and high conformity of plasmonic hot spots, which are desirable for scalable fabrication and usage. Own to the new scheme of developing the template stripping metal film, a large scale ultrasmooth metallic film tat has been implemented, openimg up the new opportunity for extreme nanophotonics such as sub-nanometer plasmonic rules[46,47], plasmonic nonlocal effect[48] and even plasmonic quantum tunneling effect[49].

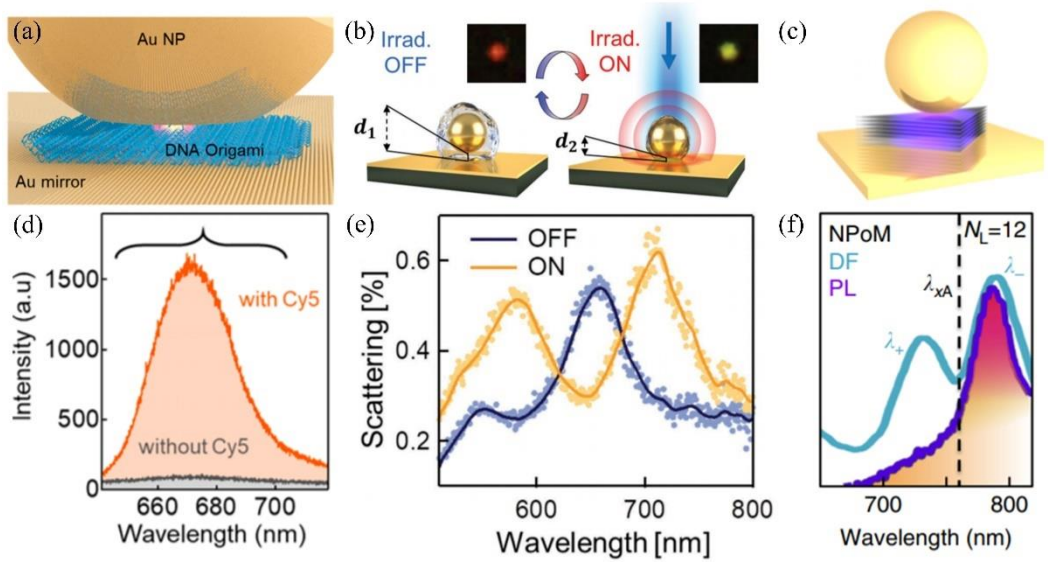

Figure 1.7 (a) NPoM dye molecule Cy5 assembled by DNA Origami[44]; (b) NPoM coated with poly(N-isopropylacrylamide) (PNIPAM) for actuator function[45]; (c) NPoM with TMDC[35]; (d-f) PL and Scattering spectrum for above structures.

1.7 Transition Metal Dichalcogenide (TMDC)

The group VI semiconducting class of few layers transition metal dichalcogenides (TMDC) have launched intense interests due to their promising properties for photonics and optoelectronic applications. With the enhanced quantum confinement and small dielectric screening effect in two-dimensional material (Figure 1.8 (a) and (b)), the strong Coulomb interaction in TMDC thus presents profound excitonic responses (Figure. 1.8 (c))[50,51]. Especially when TMDC is thinned down to ML, its direct bandgap nature facilitates excitonic emission at K (K-) point of Brillouin zone which carries valley polarization for providing a new degree of freedom for electronics and photonics application[52]. The two-dimensional (2D) hexagonal lattice of TMDC consists of internal layer transitional

metal atoms (e.g., Mo, W) sandwiched with two layers of chalcogen atoms (e.g., S, Se). The breaking of inversion symmetry in the 2D hexagonal crystal lattice with strong spin-orbital interaction induces two degenerated energy states at valleys K (K-), which serves as valley pseudospins[53–55].

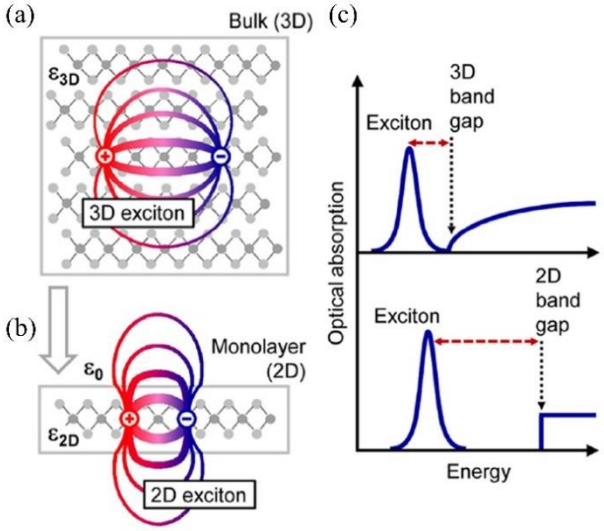

Figure 1.8 (a) schematic diagram od exciton in bulk TMDC; (b) schematic diagram od exciton in 1L TMDC; (c) the binding energy comparison between exciton in 3D and 2D system[50].

1.8 Coulomb-Bound Electron-Hole Pairs

Owing to the many-body effects such as Coulomb interaction between multiple electrons in matter, the transition of an electron from the valence band (VB) to the conduction band (CB) experiences the interaction from the remaining electrons in the conduction band[56]. This complex understanding of the many-body system can be simplified as a CB electron coupling with the VB hole through Coulomb interaction. The influence of interaction between electron and hole is categorized into direct and exchange interaction ,which contribute to both long-range and short-range coupling. In the semiclassical approach, the long-range coupling is

considered as the classical attractive Coulomb interaction between the negatively charged electrons and positively charged holes. Accordingly, the negative potential energy in Coulomb interaction induces electron-hole pair bound states which are frequently termed as neutral excitons (X_O). In common with the hydrogen model, excitons in TMDC consist of series of principal orbitals such as 1s, 2s, 3s, etc[50], depending on the spacing between the electron and hole. However, distinct from the traditional 2D hydrogen model, the energies of principal orbitals series in TMDC deviate from the tendency of any 2D hydrogen-like system as shown Figure 1.9 (a-c)[50]. This discrepancy originates from the considerable variation of experienced effective dielectric function for different orbitals of exciton as shown in Figure 1.9 (d). The non-uniform dielectric environment induces a variation of the experienced effective dielectric function. While the distance between electron and hole is small (at low principal orbitals), a larger fraction of electric field leaks out of the TMDC layer. It illustrates a more significant reduction of dielectric screening. While the spacing becomes larger, the majority of electric field maintains inside the TMDC layers and experiences less “antiscreening” effect. The experimental results at large principal orbitals thus match with the initial prediction of 2D hydrogen model.

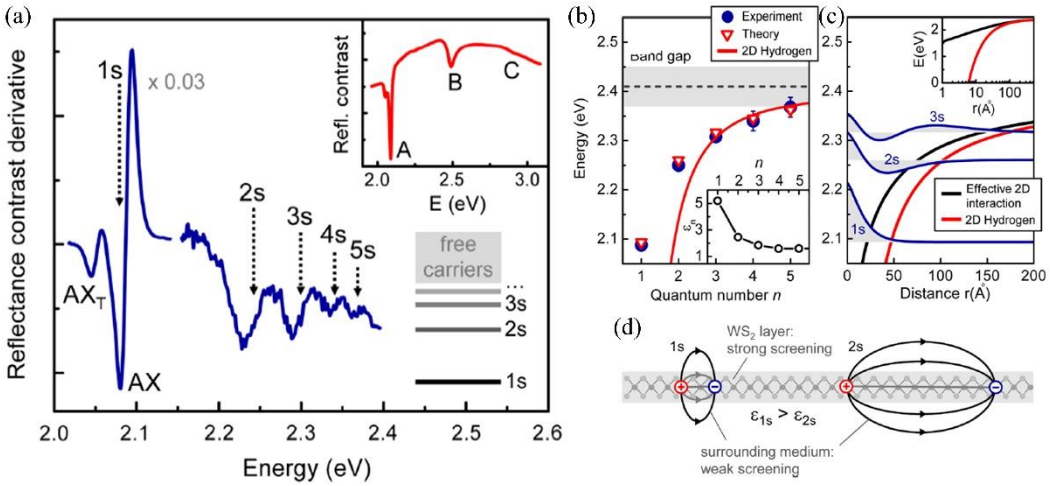

Figure 1.9 (a) the nonhydrogenic Rydberg series of neutron exciton in WS_2; (b) energy of Rydberg series in both experimental and theoretical studies, comparison with traditional 2D hydrogen model; (c) comparison of exciton energy in traditional 2D hydrogen model and screen 2D system; (d) the schematic diagram of effective dielectric media experienced by the nonhydrogenic Rydberg series of different orbitals of X_O[50].

Apart from the principal quantum number in the excitonic Rydberg series, the azimuth quantum number also plays a crucial role in the excitonic responses of TMDC. Two-photon photoluminescence (TPL) spectroscopy experimentally probed the existence of 2p, 3p states of neutron exciton (X_O) which have angular momentum dependent energy and are optically forbidden under single-photon process due to parity restriction (Figure 1.10 (a) and (b))[57–59]. Resulting from the intense density of state at those orbitals and breaking of centrosymmetry, the TPL has a giant emission feature under two photons resonant excitation at p states. This feature unveiled that the importance of different optical selection rules in various optical transition processes.

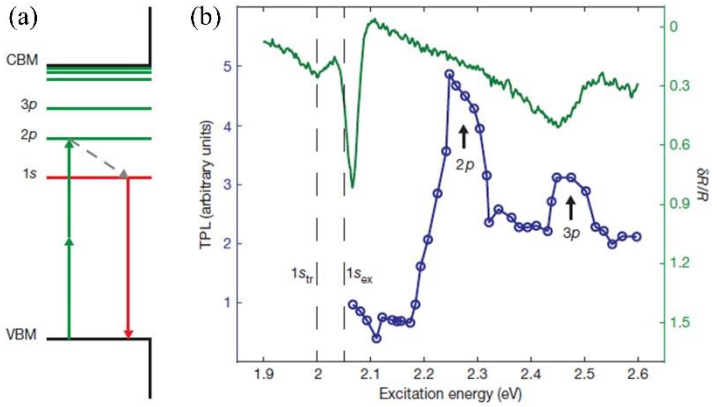

Figure 1.10 (a) the schematic diagram of the energy level of probing dark states under Two-photon photoluminescence (TPL) spectroscopy; (b) the two-photon photoluminescence (TPL) along different excitation frequency under equal power pumping[57].

Despite the similarity in the direct Coulomb interaction of exciton and a hydrogen atom, the exchange Coulomb interaction has no direct semiclassical analogue in understanding the underlying physics. This property originates from the fermionic nature of electrons and holes in exciton which should obey the Pauli exclusion principle to form antisymmetric wavefunction of excited carriers with respect to the remaining carriers. To mimic the direct Coulomb interaction, exchange Coulomb interaction can also be expressed in both short- and long-range interaction. The short-range exchange Coulomb interaction which, has a high dependence on the spin and valley states on electron/holes, introduces fine energy splitting in the bright and dark exciton states (will be discussed in the next section). Meanwhile, the long-range exchange interaction in TMDC, which behaves like a backaction of induced EM field with corresponding exciton, enables the interchanging of excitons at opposite valleys to justify the relaxation path of excitons.

1.9 Dielectric Function of TMDC

The dielectric function, which is a mesoscopic cognition of electromagnetic properties in materials, connects the experimentally observed phenomenon to the theoretical understanding of band structure in materials. The understanding of the dielectric function of TMDC launches the opportunity in numerous functionalities such as photonics, optoelectronics application, etc. To access the in-plane dielectric function of TMDC, a microscope study on the reflection or transmission spectra is one of the most convenient methods to explore the corresponding mesoscopic properties[60–62]. After measuring the reflection (transmission) of white light from TMDC and substrate, Kramers-Kronig constrained analysis is subsequently applied on the measured spectra to obtain the dielectric function of TMDC.

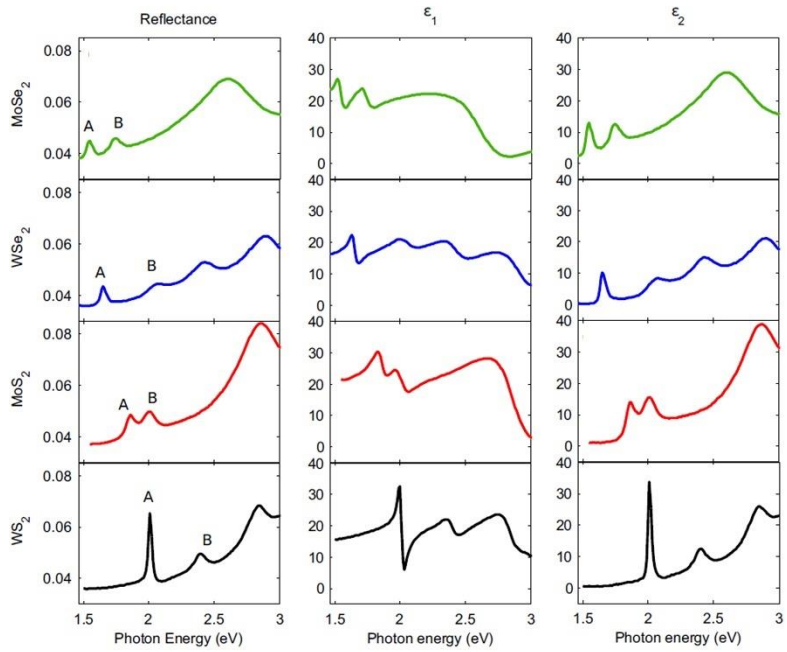

Figure 1.11 The reflectance of WS_2, MoS_2, WSe_2, $MoSe_2$ on SiO_2 substrate and the corresponding dielectric function $\varepsilon_1 + i\varepsilon_2$[60].

As shown in Figure 1.11, every reflection spectrums of the group V TMDC including WS_2, MoS_2, WSe_2 and $MoSe_2$ demonstrate two resonant peaks which are considered as the A and B excitons at the K(-K) valley[60]. Those two experimental observed resonant absorptions show a nice agreement with the density functional theory (DFT) calculated spin-orbital coupling splitting in valence band at K(-K) valley. For the other profound resonant features in group V TMDC, the origin is still highly debatable. Daichi Kozawa *et al.* proposed the "C exciton" in MoS_2 originated from the parallel band edges of CB and VB across Γ and K points in the bandstructure[63]. This band nesting phenomenon potentially induces considerable joint density of states (JDOS) which intensify the absorption of light at a certain wavelength. Meanwhile, the large background dielectric constant in both 1L and bulk group V TMDC is one of the most underrated optical features in TMDC. To contemplate the high anisotropy of the dielectric function of the TMDC, with the proper design of the geometry, a multiple layers TMDC Mie resonator with anapole mode resonance[64,65] or multiple layers TMDC dielectric grating[66] are able to be realized. These resonances of nanostructure are capable of coupling with the corresponding intrinsic exciton to form anapole exciton polariton or plasmon-exciton polariton, which support novel functionality for nanophotonics applications.

1.10 Dark and Bright Excitons

In TMDC ML, the exciton-photon coupling phenomenon is dominanted by the bright exciton at the K(-K) valleys, which couples with σ+(σ-) polarized photon due to the C_{3h} group symmetry in the crystal lattice. Under the scattering-induced spin-flipping and changing of momentum by scatters including multiexcitons, electrons, phonons or defects, dark excitons are potentially induced under the near-resonance excitation at near incidence. Especially when the TMDC is non-resonantly excited, the relaxation process induces multiple channels to various excitonic states, including dark exciton states.

The derivation of spin configuration between bright and dark exciton governs the properties in corresponding emission. The bright exciton emerges from the optical transition at K(-K) valleys which corresponding CB and VB have the same spin polarization. Deviated from bright exciton, the dark exciton arises from K(-K) valleys that corresponding CB and VB have antiparallel spin polarization[67–70]. The symmetry analysis by G. Wang et al. on ML TMDC revealed that bright excitons, including A and B bright exciton, have dipole moments in the in-plane direction (xy plane) as shown in Figure 1.12 (a, c), while dark exciton has dipoles in the out-of-plane direction (z plane) as shown in Figure 1.12 (b, d)[71]. It signifies that the spin-forbidden dark exciton still has a nonzero transition dipole moment, which originates from the spin-orbital mixing phenomenon in the valence band. The near tangential collection of PL from WX_2 thus has the finest collection efficiency of

those dark exciton emissions. Coupling the out-of-plane dipole of dark excitons with a strong out-of-plane field in SPP is an alternative to observe dark exciton emission (Figure 1.12 (e))[72]. Through encapsulating the WSe_2 with h-BN layers on a silver mirror, dark exciton interacts with the near field of SPP mode for out-coupling to surface normal (Figure 1.12 (f)).

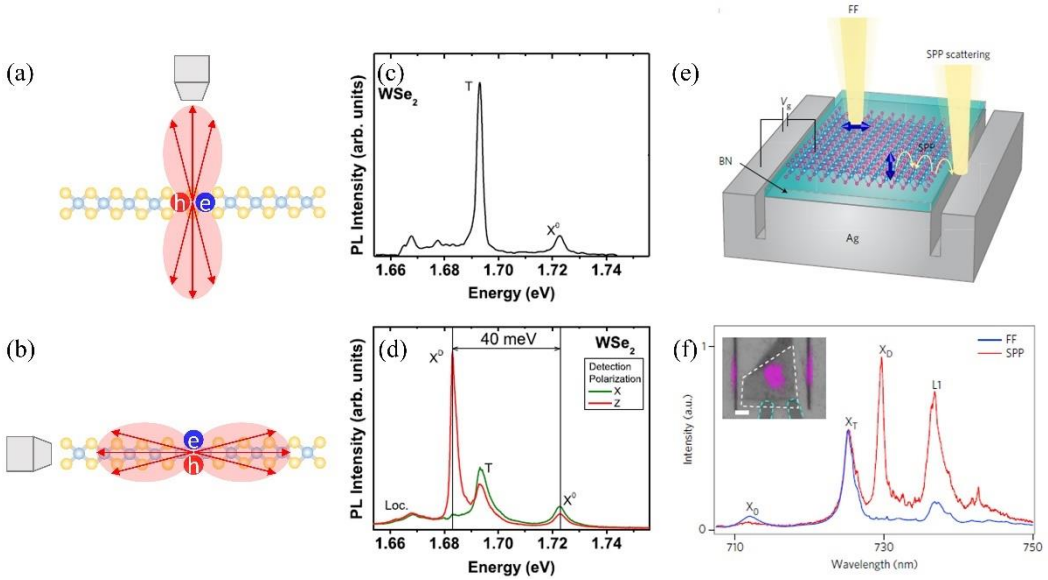

Figure 1.12 (a,b) Schematic diagram of normal collection of bright exciton emission and tangential collection of dark exciton emission; (c,d) Corresponding spectrum of (a,b) configuration[71]; (e) Schematic diagram of SPP coupled dark exciton emission; (f) Corresponding spectrum of SPP coupled dark exciton emission[72].

Hybridizing the characteristics of bright exciton and dark exciton through an intense in-plane magnetic field is a novel approach in direct probing the existence of dark exciton. In TMDC ML, the spin-orbital interaction (SOI) induced splitting is at the order of hundreds of meV for holes in VB and tens of meV for electrons in CB[69,70,73,74]. This phenomenon induces an effective magnetic field (B_{eff}) for electrons and holes generally proportional to corresponding SOI. Based on order

of magnitude difference in B_{eff}, the tiling of spin by an external magnetic field (B_{ext}) is pronounced in CB but inconspicuous in VB (Figure 1.13 (a-c)). Under the non-parallel spin states in CB and VB for dark excitonic transition, the breaking of orthogonality suggests the allowance of mixing bright exciton's property with dark exciton's which intensifies the dark exciton oscillator strength and inclines the emission into normal direction.

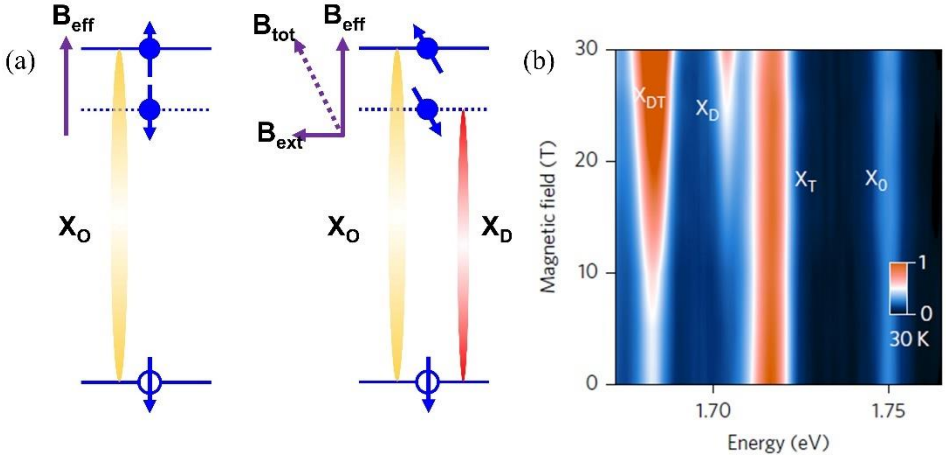

Figure 1.13 (a) Schematic diagram of admixing the properties of bright and dark exciton through in-plane magnetic field tiling of spin states in CB; (b) Experimental observation of PL under varying magnetic field[69].

Chapter 2 Nanostructure Preparation and Metal Mirror Fabrication

In this thesis, I introduce gold core-sliver shell nanocuboid (Au@Ag NC in Figure 2.1 (b)) and gold particle on metal mirror (NPoM in Figure 2.1 (a)) as the two major plasmonic nanocavities to study the potential in coupling phenomenon with TMDC including MoS_2, WS_2 and WSe_2. The first section of this Chapter is about the sample preparation on nanostructure, including TMDC synthesis, exfoliation, and metal mirror deposition. The second part introduces the characterization of nanostructure, including morphology under various conditions. The last part of this Chapter discusses the working principle and details of different optical spectroscopy setups in the experiments.

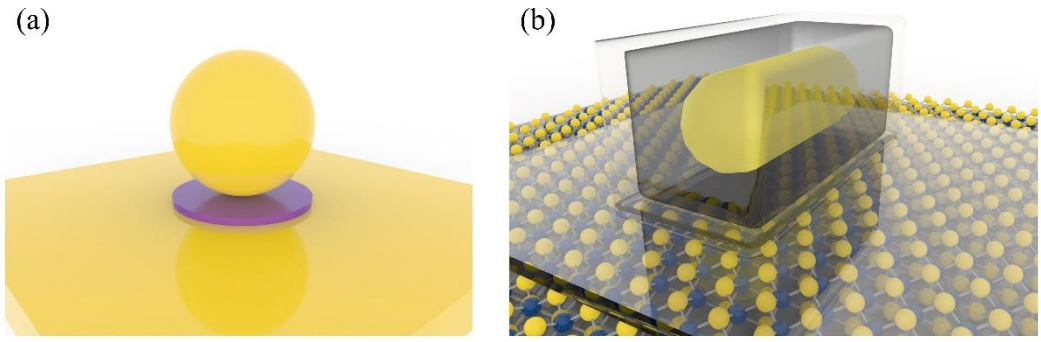

Figure 2.1 (a) Schematic diagram of reactive ion etching (RIE) of WSe_2-NPoM structure; (b) WSe_2/MoS_2-Au@Ag NC structure with encapsulation from Al_2O_3 layers to form a high chemical resistivity and refractory nanostructure.

2.1 Deposition of Metal Mirror

To fabricate the NPoM nanostructure, the gold mirror was firstly deposited through the electron beam vapor deposition. As shown in Figure 2.2, electron beam

deposition employs a magnetic field to guide the electron beam generated from the electron gun to hit the source material. Under the high vacuum in the chamber, the source material is heated up and directly evaporates into vapour. The stream of material vaporizes and deposits on the substrates and form a thin film. The thickness and surface roughness of thin films are two elemental parameters to assess the quality of the metal mirror. The vacuum condition in the chamber significantly lengthens the mean free path of the residual gas which has less collision with the stream of rare material. Under this suspended scattering between stream of rare material and residual gas, the smoothness of the metal mirror subsequently improves. Optimizing the deposition rate is another approach in forming a smooth metal mirror with minimized surface roughness. Even the vacuum level is high inside the chamber, an unavoidable chemical reaction between a stream of rare material and residual gas still exists. A faster deposition rate suppresses the duration of possible chemical reaction and improve the film uniformity. However, an overly rapid deposition rate induces bombardment of the previously formed crystal grains and restricts the growth of grain size. The smaller grain size thus induces larger roughness on the film surface. A certain deposition rate is necessary for obtaining the optimized smoothness of thin films.

To advance the surface smoothness of metal mirror for approaching SPP limits and realizing extreme optics studies, a template stripping technique was investigated to form ultra-smooth metal mirror which can be further patterned into other

nanostructures[75–77]. This scheme utilizes the poor adhesion between noble metal and traditional substrates such as glass and silicon wafer to facilitate the exfoliation of metal mirror from the smooth template substrates. Once the noble metal mirror is deposited on the template, adhesion glue is successively coated on the exposed metal surface and is stuck with an actual substrate. Benefited from the mature semiconductor fabrication technology, a template such as a silicon wafer might have a root mean square (RMS) roughness of ~ 0.2 nm. The template stripping noble metal mirror thus has a roughness of ~ 0.3 nm (Figure 2.3 (b)).

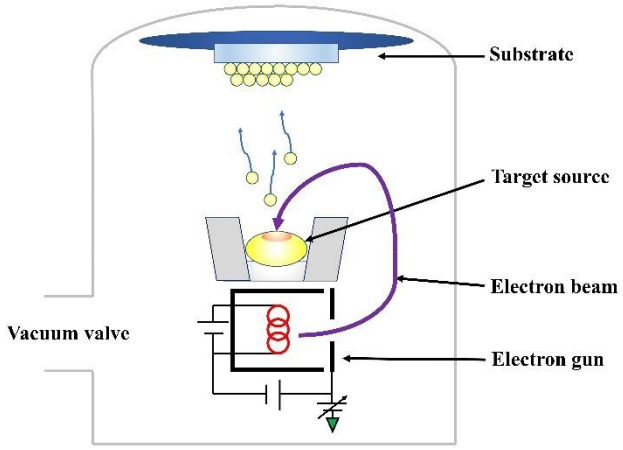

Figure 2.2 Schematic diagram of electron beam evaporation of gold mirror.

In the actual experiment, the electron beam deposition of the gold mirror was conducted in a commercial system (Denton Vacuum). A silicon wafer was loaded on the sample holder with a rotation rate of 5 rpm to get a uniform deposition. A 24 K gold target was mounted on the target holder. The chamber was pumped down to 8 x 10^{-8} Torr through 15 minutes pumping by mechanical pump and 2 hours pumping by turbomolecular pump. The electron beam was focused on the target crucible under an operation current at 53 mA. This corresponds to a deposition rate

of ~ 1.5 $Å s^{-1}$. After ~ 23 minutes of deposition, a 200 nm-thick gold mirror was formed. A UV-sensitive photopolymer (Norland Optical Adhesive 61, Norland Products) was dropped on the exposed gold surface and glued with another silica substrates (Figure 2.3 (a)). The photopolymer was sequentially cured by 30 minutes exposure of UV light. The metal mirror was lastly peeled off from the silicon template with the help of a razor blade.

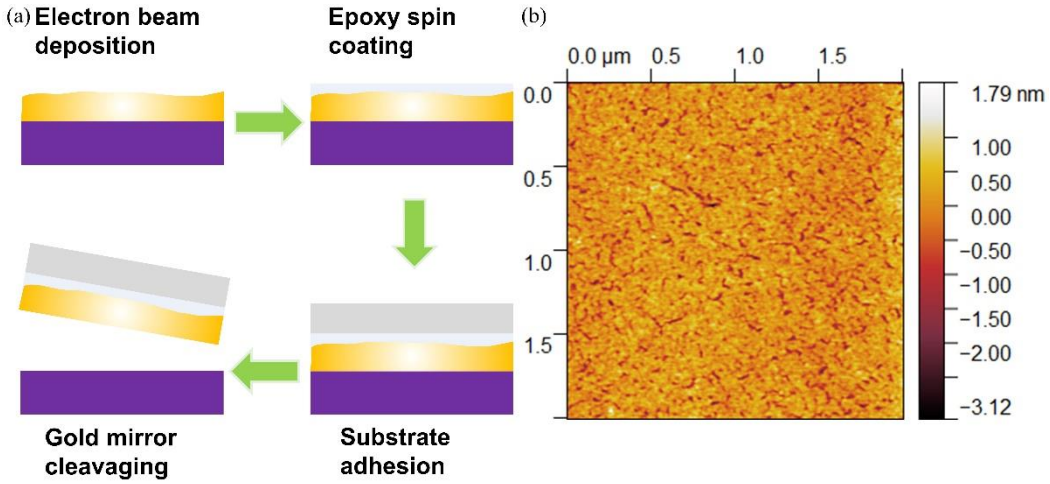

Figure 2.3 (a) Schematic diagram of template stripping method of the gold mirror from silicon substrate; (b) Our template stripped 200 nm gold mirror with root mean square roughness of ~ 0.32 nm.

2.2 Micromechanical Exfoliation of TMDC on Gold Mirror Surface

Similar to graphite structure, TMDC crystals consist of multilayers of TMDC ML which are attracted together through weak van der Waals force. Due to the orders of magnitude difference in strength between covalent bond in intralayer attraction and van der Waals force of interlayer attraction, ML TMDC can be exfoliated from the bulk crystal without damaging the intralayer structure. The idea of mechanical

exfoliation of TMDC are classified as using normal force or lateral force in exfoliation processes[78]. In this thesis, I only consider the traditional normal force method, which is also the method initially demonstrated by the Nobel laureates Andre Geim and Konstantin Novoselov. In their classical experiment, Scotch tape was applied to stick on the high ordered pyrolytic graphite (HOPG) and repeatedly thinned down the HOPG crystals through utilizing the normal force to cleavage the HOPG. By repeating the process several times, ML TMDC potentially existed on the Scotch tape. After the direct adhesion of Scotch tape on the substrate, ML TMDC was left on the substrate.

Even though the traditional Scotch tape method is intuitive and simple, this micromechanical cleavage method leaves numerous residues on the substrate or even TMDC flakes by cause of the strong adhesion from the soft polymer in Scotch tape, as shown in Figure 2.4 (a). Those residues might influence the optical measurements and pollute the samples which obstruct the formation of ideal WSe_2-NPoM nanostructures. To fabricate clear WSe_2-NPoM nanostructures, I utilized a Gelfilm (GelPak) as a stamp for transferring the WSe_2 flakes from Scotch tape to gold mirror substrate. After several times of folding and exfoliation on Scotch tape, instead of direct adhesion the tape on the substrate, we adhered Gelfilm on those few-layered TMDC on Scotch tape. Quick removal of Gelfilm in the normal direction sequentially permitted the exfoliation of large area TMDC flake from the tape. The Gelfilm was then adhered to a gold mirror, followed by a gentle removal

of Gelfilm for better TMDC gold mirror adhesion. Since Gelfilm is a viscoelastic material that has a rigid polymer structure, significantly fewer residues would be adhered on WSe_2 flake or substrates (Figure 2.4 (b)).

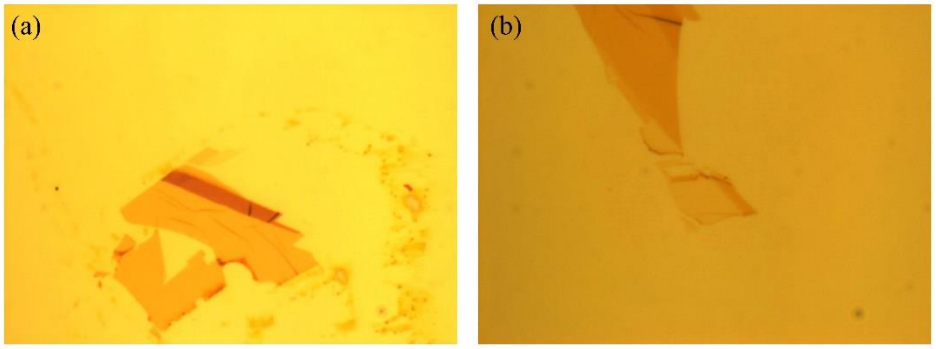

Figure 2.4 (a) WSe_2 on Au mirror structure prepared by traditional Scotch tape mechanical exfoliation method; (b) WSe_2 on Au mirror structure prepared by modified Scotch tape mechanical exfoliation method with Gelfilm in the transfer process.

2.3 Preparation of Single Nanostructure

The gold core-sliver shell nanocuboid (Au@Ag NC) and gold nanosphere (AUNS) were synthesised by NanoSeed Ltd. (Hong Kong) through the wet chemical method. The AUNS sample has an average size of 120±10 nm diameter. The Au@Ag NC sample has a gold core nanorod with 32±3 nm diameter and 83±7 nm length, while the corresponding silver shell is 7 nm thick in the side region and 5 nm thick in the end region. The surface of both nanostructures is surrounded by a single layer of cetyltrimethylammonium bromide molecules (CTAB) which is positive charged to avoids aggregation of nanostructure through repulsion. To remove the excess CTAB, the solution of Au@Ag NC and AUNS was centrifuged at the speed of 5000 rps for 20 minutes and 15 minutes, respectively. After removing the previous solution, a double amount of deionized (DI) water was

added back to the solution for dilution. The Au@Ag NC was dropped on WS_2/Al_2O_3 and MoS_2/Al_2O_3 samples. The AUNS was dropped on WSe_2-Au mirror structure. After around 30 seconds of immersing in AUNS solution, the samples were tilted to remove the residual solution and absorbent paper was used to absorb the remaining droplets on the samples.

2.4 Atomic Layer Deposition

Atomic layer deposition (ALD) is a layer-by-layer chemical vapor reaction process to fabricate thin films in nanoscale. In the deposition process, two gas phase precursors are necessary to perform layer by layer deposition. To prevent chemical reaction of precursors before adhesion on substrate, the inflow of precursors is restricted as sequential, non-overlapping pulses with noble gas as nitrogen purging to remove unreacted gas phase precursors inside the chamber as shown in Figure 2.5. Controlling the numbers of cycles in ALD induces a precise deposition of amorphous phase nano thin films.

In my experiment, I utilized ALD to deposit alumina (Al_2O_3) layers to encapsulate the Au@Ag NC. The main function of alumina layers was to prevent chemical reaction between Au@Ag NC and sulfur atoms in WS_2 or ambient environment. It also suppressed the potential of Au@Ag NC deformation under rising temperature. The spacer layer wais limited to ~ 0.8 nm for compensating coupling between Au@Ag NC and WS_2 and potential sulfurization. The upper layer was set

as ~ 2 nm which has proven refractory properties even at several hundred centigrade[79].

The deposition of alumina layers was done in a commercial ALD system (Savannah G2, Ultratech). The entire ALD process was held at 80ºC to ensure no deformation or sulfurization in WS_2 and Au@Ag NC. For the inflow of alternating gas, pulse duration of both gases was limited to 0.015 s for every 10 s of reaction time. During the switching between those gas phase precursors, 5 sccm nitrogen was flushed into the chamber to remove the remaining precursors. It took 7 cycles (27 cycles) to deposit 0.5 nm (2 nm) thick alumina layers.

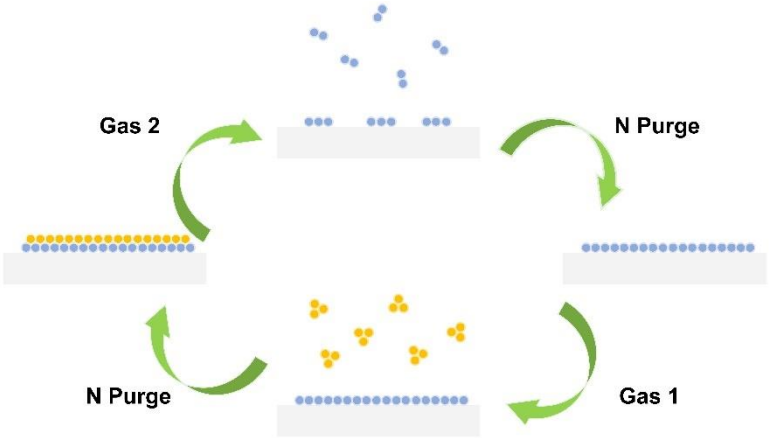

Figure 2.5 The mechanism of atomic layer deposition through n-th cycles of chemical deposition.

2.5 Reactive Ion Etching

The reactive ion etching (RIE) is a traditional dry etching technology, which drives plasma ions to engrave the surface of the sample anisotropically. A regular 13.56 MHz radio frequency (RF) electric field ionizes the gas source to form the plasma. Through biasing the top and bottom electrodes in the chamber, ions are driven

toward the sample subsequently. It gives a fine anisotropic etching of nanostructures.

We exposed WSe_2-NPoM in the directional argon plasma in the multifunction RIE-ICP platform (TRION, Phantom RIE ICP), as shown in Figure 2.6. To achieve high anisotropicity propose, we only applied the RIE function of the platform to obtain a high anisotropic etching. The power of the 13.56 MHz RF generator was regularized at 10 W to suppress the over-etching of the remaining parts in WSe_2. The operating pressure of the chamber was maintained at 10 mTorr with a flow of 2 sccm argon gas to generate low yield of argon ions for precise directional etching. Considering the atomic thin WSe_2 ML, we held the etching process for a total of 10 s, which included 5 s warm up process and 5 s steady argon ion bombardment.

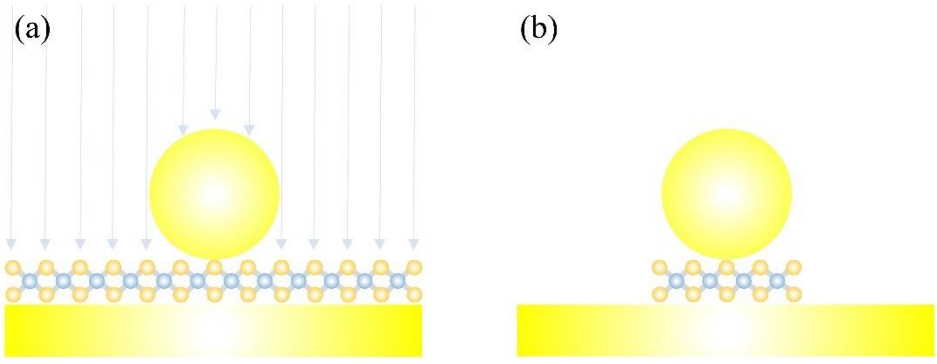

Figure 2.6 (a) Schematic diagram of RIE etching of WSe_2 outside the AUNS shadow mask; (b) the finalized structure of WSe_2-NPoM.

2.6 Dark Field Spectroscopy

Relied on the nearly free background noise from the dark field (DF) spectroscopy, DF scattering of plasmonic structures has become one of the most elementary

methods to study the corresponding optical responses. The main discrepancy between BF and DF microscopy is the illumination scheme of samples. In DF microscope, a near grazing incidence of light illuminates on samples and leaves from the collection path of microscope to construct a scattering imaging with nearly free background signal. Commercial DF microscopies are catalogized into reflected and transmitted modes of illumination. In the reflected mode of DF microscopies, a white light beam initially passes through the ordinary path of BF with filtering from a ring-like light stop. That light is reflected on the ring-like condenser by a beam splitter. Those light beam then loosely focuses on the sample. In the transmitted mode of DF microscopies, the light also experiences the ring shaped spatial filter. The beam transmits through the glass slide and is then focused on the sample by a condenser.

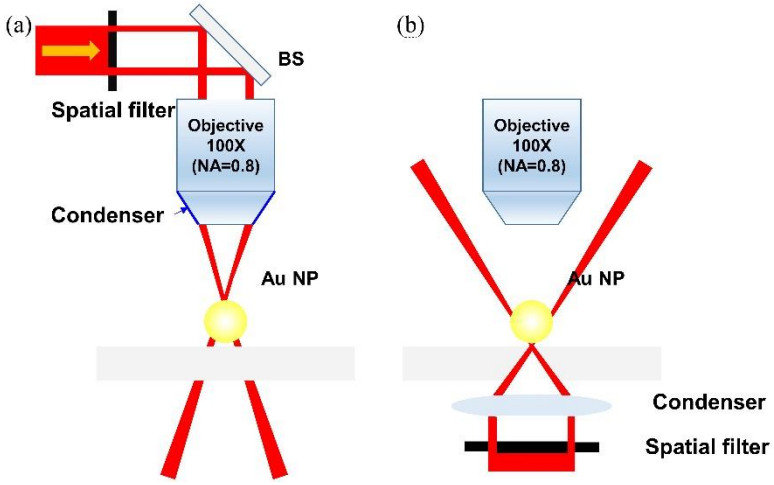

Figure 2.7 (a) Working principle of reflected mode of DF microscopy; (b) Working principle of transmitted mode of DF microscopy.

In the actual DF experiments, the DF measurements are conducted in a customized microscope system (BX 51, Olympus) coupled with a 100X DF objective (LM-

Plan, NA 0.8) under a reflected mode configuration. The white light was modulated into a cylindrical beam through a spatial filter and focused on the sample through the condenser in the outer shell of the DF objective, as shown in Figure 2.7 (a). The backscattered radiation from a single nanoparticle was collected through the same objective. The collected scattering radiation was then split into two paths. One path of light formed the image through the eyepieces and the other path of the light beam was focused on the spectrometer (Princeton Instruments, SP2300i) equipped with TE-cooled CCD (Pixis, 400 BR-eXcelon). The two-dimensional array of CCD was adopted to measure spectra not only from a single point but also from a line of spectra. In obtaining these spectra, we restricted the images of nanoparticles within the microscale width slit region. It isolated the desired nanoparticles region from the background. The spectrometer was then changed to spectrum mode by rotating the grating to the appropriate orientation for dispersion of light. A line of spectra was then captured by the TE-cooled CCD.

2.7 Photoluminescence Spectroscopy

The photoluminescence (PL) spectroscopy was conducted in a commercial confocal Raman mapping system (Witec, UHTS 600 VIS). The 532 nm diode laser was guided into the microscope system through a photonic crystal fiber. The green laser was focused by a 100x/50x fluorescence objective (Epiplan-Neofluar, NA 0.9/NA 0.55) to form a ~ 1 μm laser spot. The ~ 100 nm scale WSe_2-NPoM was

carefully adjusted to overlap with the laser spot. The photoluminescence from the WSe_2-NPoM was collected by the same objectives and coupled to spectrometer through photonic crystal fiber. A 150 lines/mm grating was used to disperse the signal for width range measurements.

Chapter 3 Revealing the Role of Dark Exciton in Unusual Temperature Tendency of Electromagnetic Interaction between Plasmonic Cavity and Exciton in TMDC

The electromagnetic interaction between modes in photonics cavities and quantum states in materials has prompted various fundamental studies especially in quantum optics. While the energy exchange interaction rate between excitons and plasmonic nanocavities overcomes the damping rate in the corresponding eigenstates, a strong coupling phenomenon is formed and produces a hybrid state called “plexciton”, which acquires mixed properties of both light as well as matter[1,16,80]. The plexciton serves as a fundamental constituent for quantum electrodynamics studies such as quantum entanglement[80–82], polariton laser[10–12] and Bose-Einstein condensation[7,8,83]. The promising potential of nanophotonics applications, including quantum communication[82], single-photon switches, nonlinear optics[84] and threshold-less lasing etc., raises strong motivation in related research studies. To realize strongly coupled plasmon and exciton states, facilitating coupling strength and suspending dissipation are two elemental requirements[5]. The ratio of Q-factor to mode volume (Q/V) defines a cavity’s ability to boost the interaction with QEs. Plasmonic nanocavities, which confines light into subwavelength scale, can amplify the light-matter interaction so as to

form plexciton states.

As mentioned in previous chapters, TMDC MLs possess unusual excitonic properties in comparison with conventional QEs such as dye molecules[6,84], j-aggregates[85–88] and QDs[14,89]. Benefited from small dielectric screening and large quantum confinement, effects from the atomically thin crystal structure, the robust exciton dominates the optical response in TMDC[51,60,90,91]. The combining of the breaking inversion symmetry and pronounced spin-orbit coupling (SOC) results in energy splitting of valence and conduction bands (VBs and CBs) based on spin states[52,92]. As a direct consequence of spin splitting in CB, the bright (X_O) and dark (X_D) excitons in TMDC MLs consist of antiparallel spin states for exciton-hole pairs and parallel spin states for exciton-hole pairs respectively[68,69,93]. Based on the symmetry analysis, the bright exciton is optically sensitive to out-of-plane propagating light when the dark exciton is weakly sensitive to in-plane propagating light[71,72,94]. Consequently, dark exciton's contribution to nanophotonics systems is frequently omitted.

In this Chapter, I examine the role of dark exciton in plexciton systems through a comparative DF study of the thermal tuning response on two distinct polariton systems including MoS_2-Au@Ag NC and WS_2-Au@Ag NC. In comparison with smooth gold nanorod (AUNR) core, the open Au@Ag NC plasmonic nanocavity contains sharp corners which confine the optical field into a smaller mode to better

interact with bright excitons of MoS_2/WS_2 ML, as schemed in Figure 3.5 (a). The first two sections (3.1 and 3.2) of this Chapter focus on the discussion about temperature dependent intrinsic optical properties of TMDC and Au@Ag NC, respectively. After understanding those characteristics of individual systems, section 3.3 extends the discussion into the hybrid systems including WS_2-Au@Ag NC and MoS_2-Au@Ag NC for comparison. The analysis of numerical studies on those hybrid systems are presented in section 3.4 to exploit the underlying physics of the similarity and difference in those plexciton systems. The conclusion will be lastly drawn by introducing an intuitive two-level model to explain the distinctions between WS_2-Au@Ag NC and MoS_2-Au@Ag NC.

3.1 Reflectance of Pristine TMDC ML Under Various Temperature

To start the study, I tested the thermal sensitive excitonic properties of pristine MoS_2 and WS_2 ML through differential reflectance($\Delta R/R_0$). Figure 3.1 (a) and (b) present the series of the thermal tendency of the measured $\Delta R/R_0$ (where R_0 and ΔR represent the reflection of light from the sapphire substrate and the difference of reflection from substrate and TMDC ML) of MoS_2 and WS_2 ML between 1.7 to 2.3 eV[92]. The $\Delta R/R_0$ of MoS_2 (WS_2) ML illustrates two (one) resonances in the experimental spectrum, which corresponds to resonant light absorption by bright A- and B-excitons in MoS_2 (A-exciton in WS_2). These excitonic resonances are highly asymmetric in the measured spectra due to the occurrence of intense JDOS along the band structure. Considering the 3 orders of magnitudes difference

between atomically thin ML and optical wavelength, it is highly desirable to apply thin-film approximation to directly link $\Delta R/R_0$ of TMDC ML with the imaginary part of the dielectric function as following (see Appendix for derivation):

$$\frac{\Delta R}{R_O} = -\frac{\pi E}{310} a_{nm} \frac{b}{r_O} \left[\sum_{n=1}^{N} f_n \frac{E_n^2 \Gamma_n E}{(E_n^2 - E^2) + E^2 \Gamma_n^2} \right] \tag{3.1}$$

where E indicates corresponding energy in eV, a_{nm} indicates TMDC ML's thickness in nanometer, b and r_0 are relative permittivities of air and sapphire (see the appendix), and the bracket term consists of N Lorentz resonances to describe the multiple excitonic resonances.

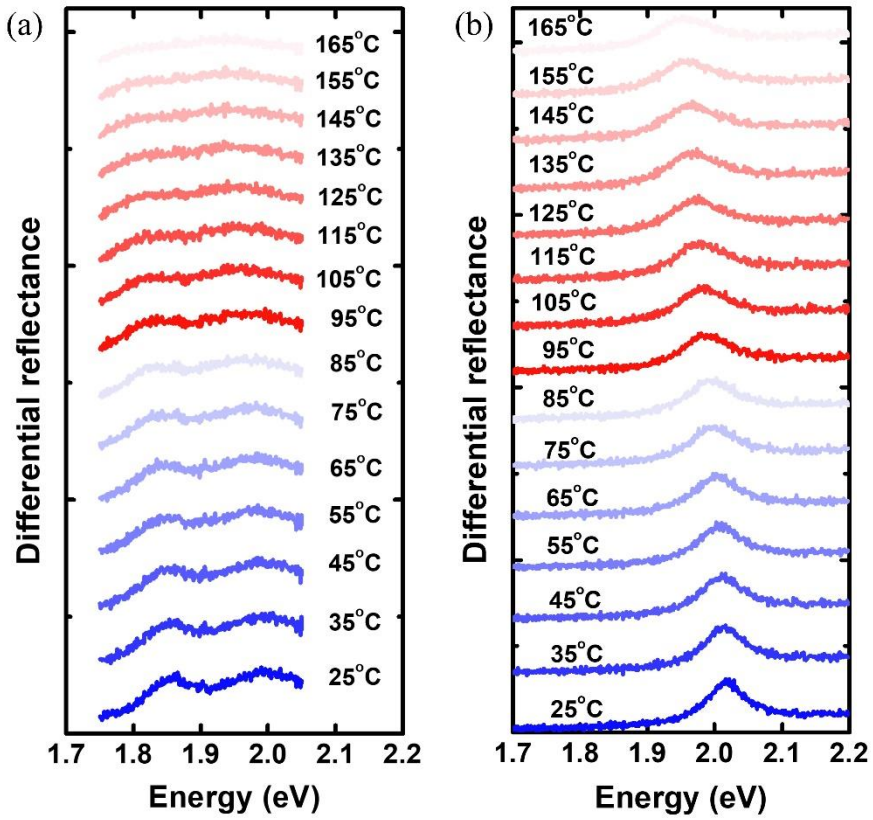

Figure 3.1 $\Delta R/R_0$ from pristine (a) MoS_2 ML and (b) WS_2 at a varying temperature condition.

The two (one) resonances in $\Delta R/R_0$ for the MoS_2 (WS_2) ML are relevant to

resonant absorption of light by intense oscillator strength of bright A- and B-excitons in MoS_2 (A- exciton only in the case of WS_2). Considering the large JDOS in the band structure at a higher energy level, these resonances of $\Delta R/R_0$ appear to be highly asymmetric. To accurately describe features in TMDC ML, those spectra in MoS_2 (WS_2) spectra in Figure 3.1 (a) ((b)) are fitted by eq 1 which includes three Lorentz resonance (two Lorentz resonances in the case of WS_2) for exploring excitonic features such as exciton resonance $E_{A/B}$, excitonic damping $\Gamma_{A/B}$, and excitonic oscillator strength $f_{A/B}$ for corresponding states under thermal tuning. The extracted parameters of $E_{A/B}$ and $\Gamma_{A/B}$ are shown in Figure 3.2. The confidence interval of each fitting parameter was introduced in each figure as fitting errors to visualize most possible distribution of each parameter in Figure 3.2. In general, the uncertainty of extracted parameters in MoS_2 was more significant than the WS_2's, since MoS_2 has more excitonic resonances in the observed range. I applied similar sensitivity analysis on the remaining results in this Chapter.

The thermal tendency of fitting extracted excitonic energies for both TMDC ML obey the mathematical description of the thermal tendency of conventional semiconductor under O'Donnell model[95]:

$$E_{A/B}(T) = E_{A/B}(0) - s\langle\hbar\omega\rangle\left\{coth\left[\frac{\langle\hbar\omega\rangle}{2k_BT}\right] - 1\right\} \tag{3.2}$$

where $E_{A/B}$ (0), s, $\langle\hbar\omega\rangle$ and k_B represent the resonance of exciton at 0 K, the coupling coefficient of exciton−phonon interaction, means phonon energy, and

Boltzmann constant, respectively. Meanwhile, the extracted linewidths follow a single-phonon anti-Stokes scattering[96,97]:

$$\Gamma_{A/B}(T) = \Gamma_{A/B}(0) + \alpha T \tag{3.3}$$

where $\Gamma_{A/B}(0)$ and α corresponds to the intrinsic dissipation of TMDC ML at 0 K and exciton−phonon coupling strength, respectively. As observed in Figure 3.2 (c) and (d), the extracted temperature dependent linewidths for both MoS_2 and WS_2 nicely comply with the single-phonon anti-Stokes scattering model. The nice agreement between experimental results and phenomenological model (Eq. 3.2 and Eq. 3.3) shown in Figure 3.2 reveals that the fitting parameters extracted excitonic features are trustworthy and matches with the physical understanding. It undoubtedly affirms the accuracy of the Lorentz model in studying the thermal tendency of excitonic features. From results shown about pristine TMDC ML, it reveals the potential of utilizing the redshift exciton resonance under the elevated condition to tune the coupling with a plasmonic cavity for strong plexciton effect among different systems.

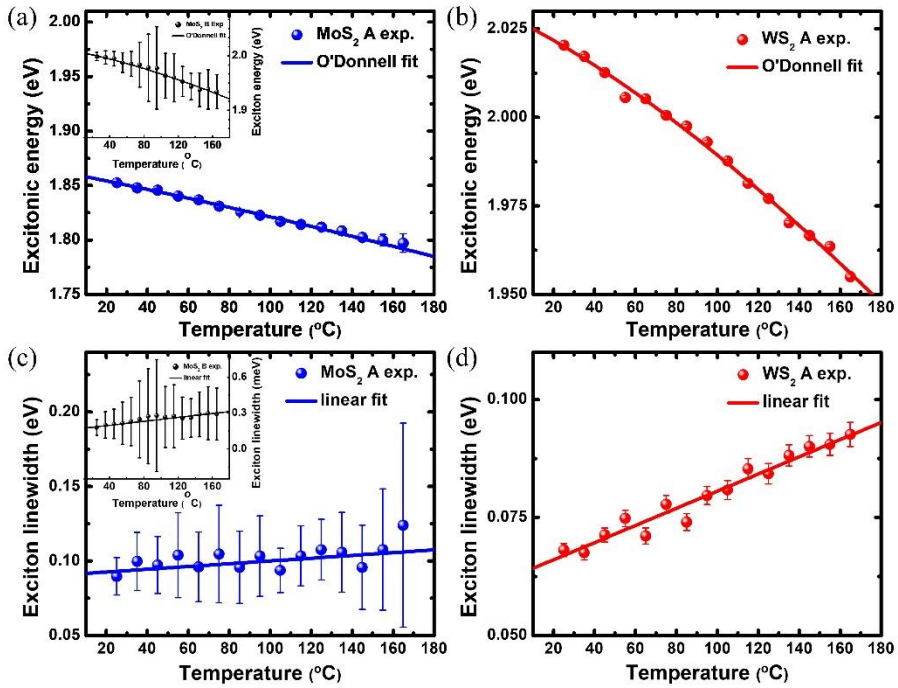

Figure 3.2 (a, b) Thermal tendency of A-exciton energy and (c, d) damping rate for (a, c) MoS_2 ML and (b, d) WS_2 ML, obtained from their differential reflectance spectra in Figure 3.1 using Eq. 3.1 (see symbols). Inserts in (a, b) show corresponding results for the B-exciton of MoS_2. Solid lines in (a, b) are fits with the O'Donnell model (i.e. Eq. 3.2) and that in (c, d) with Eq. 3.3.

3.2 Scattering of Au@Ag NC under Various Temperature

Distinct from excitonic energy, the plasmon energy of Au@Ag NC is inactive to thermal alteration. However, plasmon damping is considerably strengthened due to enhanced electron−phonon interaction (Figure 3.3)[98]. Transmission electron microscopy (TEM) was conducted to trace potential nanomorphological changes of Au@Ag NCs under elevated temperatures. To observe the real time changes of nanostructures, an electrical controlled *in situ* heating TEM grid was applied to increase the temperature of sample inside the chamber under direct TEM imaging. In each step of changing the temperatures, the sample was firstly increased to the desired temperature and kept for 10 minutes to ensure sample in steady condition.

At a certain temperature, a video was recorded to ensure any potential variations of nanostructures. Video recording of TEM images along various Au@Ag NCs disclosed on obvious nanoscale deformation or atomic redistribution process in the examined temperature range (Figure 3.4). This TEM imaging demonstrated consistency with the reversible measured thermal tuning scattering spectra. This evidenced that the measured broadening in plasmon linewidth emerged from the increased electron−phonon interaction.

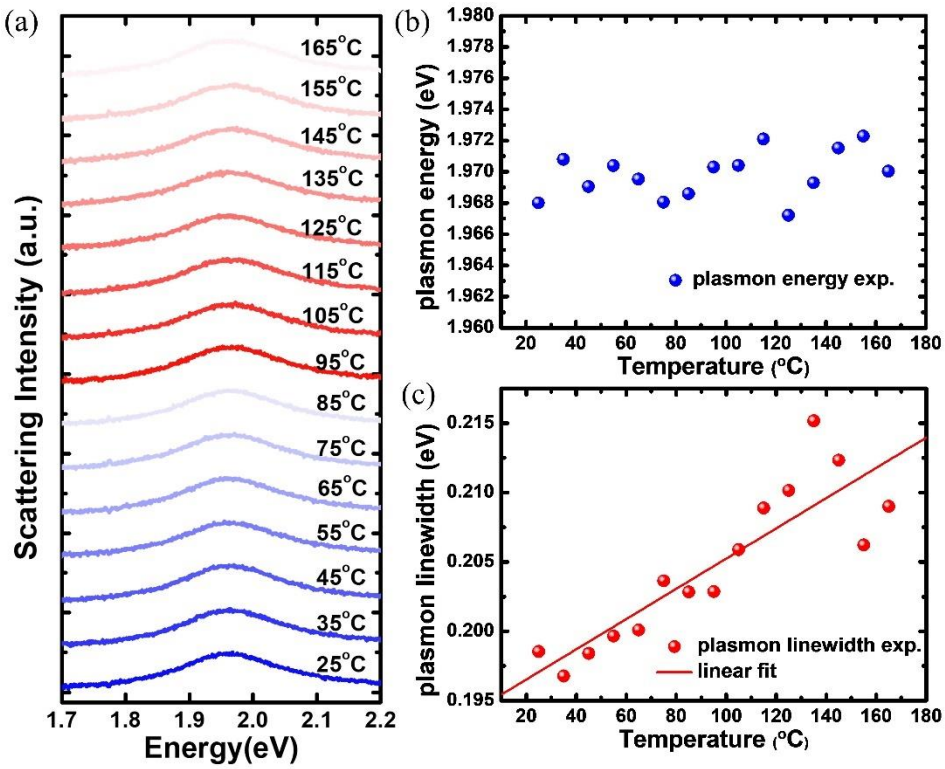

Figure 3.3 (a) Thermal tendency of scattering spectrum for a plasmonic Au@Ag NC on Al_2O_3; (b, c) Extracted plasmon energy (b) and resonance linewidth (c) from 3.3 (a).

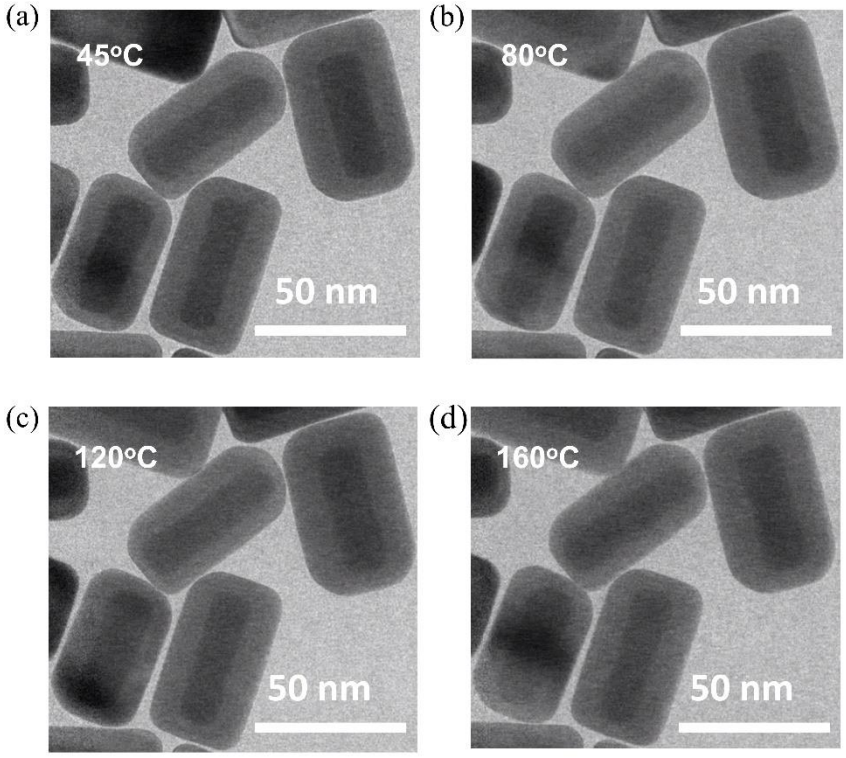

Figure 3.4 TEM images of Au@Ag NCs at (a) 45 °C, (b) 80 °C, (c) 120 °C, and (d) 160 °C. The sample was held at each temperature for 10 min to ensure the sample stability.

3.3 Spectral Decomposition of Plexciton States in WS_2-Au@Ag NC and MoS_2-Au@Ag NC Systems under Various Temperature

Through dispersing Au@Ag nanocavities on MoS_2/WS_2 ML distanced by a ~ 0.5 nm Al_2O_3 layer as illustrated in Figure 3.5 (a) and (c), plasmon-exciton coupling ensues and forms two mixed states with energies at ω+ and ω-, as revealed by those three resonances for MoS_2-Au@Ag NC in Figure 3.5 (d) and two resonances for WS_2-Au@Ag NC in Figure 3.5 (e). The series of scattering spectra under thermal tuning apparently reveal that the plasmon−exciton coupling is remarkably tailored by temperature. Based on the characteristics from pristine MoS_2/WS_2 ML and pure Au@Ag NC plasmonic nanocavity, thermal tailoring of MoS_2/WS_2-Au@Ag NC

polariton is dominated by the thermal sensitive excitons in TMDC ML. Under cavity-coupled excitons surpassing the quantum limit of cavity-coupled excitons systems, the polariton mechanism was equivalently precise in the description of the fundamental Jaynes−Cummings model (JCM) and phenomenological coupled-oscillator model (COM)[16,35,88,99–104]. Under the assumption in the model and the additional condition of suspending coupling between excitons in room temperature environment[62], the plasmon-exciton coupled system is simply treated as an external-field-driven oscillator (plasmon) coupled with internal oscillators (excitons) under a coupling strength κ. The Hamiltonian for single plasmon mode coupled with one exciton mode is written as:

$$\begin{pmatrix} E_{pl} - i\Gamma_{pl} & \kappa_A \\ \kappa_A & E_A - i\Gamma_A \end{pmatrix} \begin{pmatrix} \alpha \\ \beta \end{pmatrix} = E \begin{pmatrix} \alpha \\ \beta \end{pmatrix} \tag{3.4}$$

And for the case of two excitons modes, the Hamiltonian transforms to:

$$\begin{pmatrix} E_{pl} - i\Gamma_{pl} & \kappa_A & \kappa_B \\ \kappa_A & E_A - i\Gamma_A & 0 \\ \kappa_B & 0 & E_B - i\Gamma_B \end{pmatrix} \begin{pmatrix} \alpha \\ \beta \\ \chi \end{pmatrix} = E \begin{pmatrix} \alpha \\ \beta \\ \chi \end{pmatrix} \tag{3.5}$$

where E_{pl}, E_A, and E_B present the resonance energy of plasmonic mode, bright A- and B-excitons mode of TMDCs ML, respectively, and Γ_{pl}, Γ_A, and Γ_B are their relevant dissipation. The coupling strengths between plasmon mode and A/B-excitons modes are termed as κ_A and κ_B, respectively. In the above equation, α, β, and χ represents the eigenvectors of hybridized polaritons to illustrate the ratio of eigenmodes in those hybridized states. We applied the first Hamiltonian to describe WS_2-Au@Ag NC polariton and the second Hamiltonian to describe MoS_2-

Au@Ag NC polariton. The scattering spectra on WS_2 polariton system were fitted with the following equation:

$$\sigma_{sac} = AE^4 \left| \frac{E^2 - E_0^2 + i\Gamma_0 E}{(E^2 - E_0^2 + i\Gamma_0 E)(E^2 - E_{pl}^2 + i\Gamma_{pl} E) - 4\kappa^2 E^2} \right| \tag{3.6}$$

MoS_2 system with following relation:

$$\sigma_{sac} = A \left| \frac{(E_A - E - \frac{i\Gamma_A}{2})(E_B - E - \frac{i\Gamma_B}{2})}{-\kappa_A(-\kappa_A E_B + \kappa_A E + \frac{i\kappa_A \Gamma_B}{2}) + (E_A - E - \frac{i\Gamma_A}{2})(\kappa_B^2 - (E_B - E - \frac{i\Gamma_B}{2})(E_{pl} - E - \frac{i\Gamma_{pl}}{2}))} \right| \tag{3.7}$$

By fitting the spectra with the above equations, the resonance energy, linewidth, and coupling strength are obtained simultaneously.

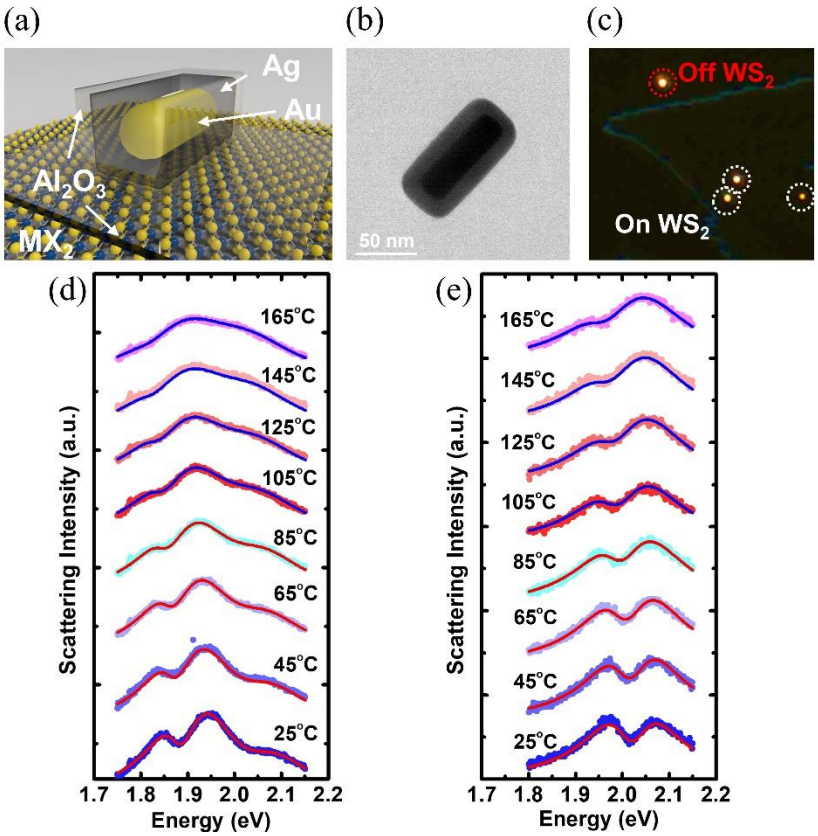

Figure 3.5 (a) Design of TMDC-Au@Ag NC with clothing of alumina layers; (b) TEM of single Au@Ag NC; (c) DF of Au@Ag NC on/off the WS_2 ML; Thermal tendency of scattering in (d) MoS_2-Au@Ag NC and (e) WS_2-Au@Ag NC.

During the COM fitting process from the above equations, the energies E_{pl}, E_A, and E_B have certain flexibility to alter slightly with respect to experimental results of eigen systems (Figure 3.4 (b) for E_{pl}, Figure 3.2 (a) and (b) for E_A and E_B), with the following adjustment. The actual values of each parameter in COM are listed in Tables A1 and A2 of Appendix. Figure 3.6 (a) and (b) illustrate the thermal tuning energy of A-exciton in MoS_2 and WS_2 ML, respectively, obtained through applying COM fitting on experimental results in Figure 3.5. By comparing the A(B) exciton energies of MoS_2 from both COM (Figure 3.6(a)) and $\Delta R/R_0$ (Figure 3.2 (a)), A 30 meV (35 meV) energy deviation was clearly shown. For WS_2 systems, the energy deviation became 20 meV (see Figure 3.6 (b) and Figure 3.2 (b)). The energy deviation was attributed to the fluctuation of excitonic energy from local doping by CVD-prepared TMDC or local strain applied from above Au@Ag NC.

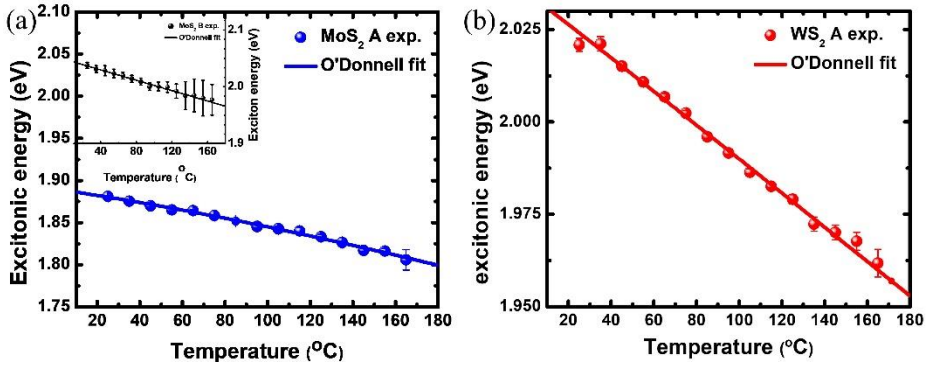

Figure 3.6 Thermal tendency of A-exciton energy for (a) MoS_2 and (b) WS_2 MLs, obtained from COM fitting on measurement in Figure 3.5. The insert (a) represents the fitted energy of B-exciton in MoS_2 ML. The lines denote relevant energy level under O'Donnell model.

To visualize the potential local variation of excitonic energy, a PL wavelength mapping was made for a WS_2 ML. Despite the high uniformity of optical image in CVD grown WS_2 (Figure 3.7 (a)), the PL mapping presented in Figure 3.7 (b) unveils considerable deviation in the PL energy along the ML flake. This may originate from local strain and doping effects of the non-ideal deposition process. Moreover, multiple DF scattering of several Au@Ag NCs deposited on several WS_2 ML flakes were measured (Figure 3.7 (c)). The Fano window of scattering spectra, which is linked with the resonance energy of A exciton, ranges from 1.99 to 2.03 eV at ambient conditions. Those experiments confirmed that variation of exciton energy along TMDC flake dominated the energy mismatch of exciton between $\triangle R/R_0$ and DF scattering. Lastly, it should be emphasized that the large background dielectric constant (~15-20) of underneath TMDC ML could shift the plasmon resonance of Au@Ag NC, specifically when the excitonic responses of TMDC ML has considerable spatial fluctuation. The Au@Ag NC plasmonic nanocavity applied in the study has an ultrasmall mode that interacts with the underneath TMDC ML within a few tens of nm^2, illustrating susceptible plasmonic responses on the fluctuation of local excitons. In the fitting values from COM, the thermal tuning of plasmon damping Γ_{pl} across the measured temperature regime approximates a linear relation as shown in Figure 3.3 (c), while the excitonic dissipation Γ_A and Γ_B follows the linear single-phonon anti-Stokes scattering in Figure 3.2 (c) for MoS_2 and 3.2 (d) for WS_2. To obtain a good fitting with scattering

measurement in Figure 3.5 (d) and (e), it is necessary to reduce excitonic damping observed from the $\Delta R/R_0$ to indicate the exciton damping in COM (35 and 10 meV shrinking of A-exciton dissipation for MoS_2 and WS_2, respectively). This shrinking of excitonic damping could be emerged from reduced inhomogeneous broadening and metal-induced dielectric screening in TMDC MLs by the Au@Ag NC.

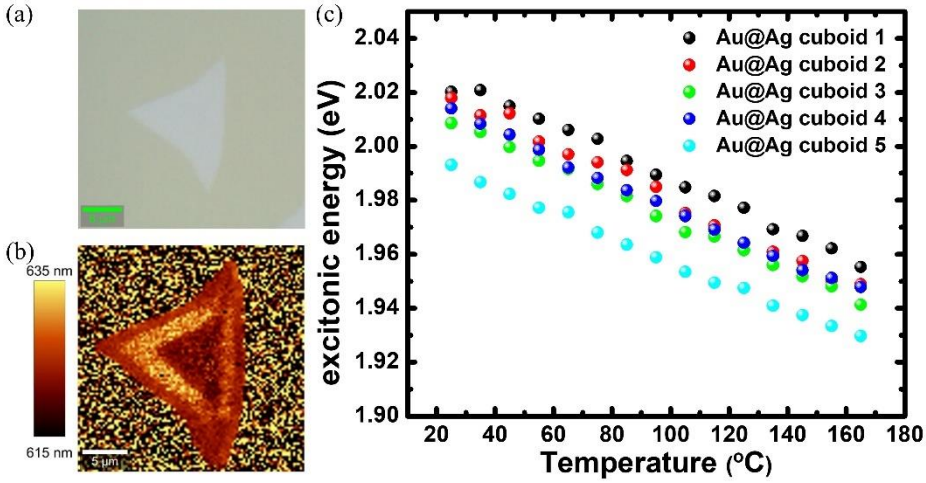

Figure 3.7 (a) BF image of a WS_2 ML flake under a 100× objective (NA 0.9); (b) PL mapping of the same flake under 532 nm CW laser excitation; (c) Energy of A-exciton in WS_2 ML obtained from COM fitting of scattering spectrums in different WS_2-Au@Ag NCs.

Through employing those principles in fitting, the coupling strength between plasmonic cavity mode and A-exciton mode for both TMDC MLs was explored, with results illustrated in Figure 3.8 (a) and (b). Surprisingly, the coupling strengths for MoS_2-Au@Ag NC and WS_2-Au@Ag NC illustrates reversed thermal tendency: by rising the temperature of the nanostructures from 25°C to 165°C, the MoS_2-Au@Ag polariton coupling strength falls from 31.2 meV to 18.1 meV, while WS_2-Au@Ag NC polariton coupling strength raises from 36.2 meV to 41 meV. In

principle, the vacuum Rabi splitting of polariton is defined as $\Omega_{Rabi} = 2\kappa$, which is the energy derivation of those two hybridized polariton states at zero detuning. To stress the potential thermal tendency of coupling strength κ in our polariton systems, Ω_{Rabi} was set as 2κ to quantify effective Rabi splitting on different temperatures. Nonetheless, such equivalent Rabi splitting is distinct from actual Rabi splitting since actual detuning is nonzero in the polariton systems. In the study, the thermal-induced evolution of the coupling strength in two polariton systems is more crucial than actual Rabi splitting. The relatively small energy derivation between the A- and B-excitons in MoS_2 ML prompts a dual coupling phenomenon with low Q-factor plasmon mode. The coupling strength polariton specifies the intuition in studying the originality of the anomalous thermal tendency of different systems. The coupling strength illustrated in Figure 3.8 reveals that effective Rabi splitting of the polaritonic coupling for MoS_2-Au@Ag NC diminishes from 62.4 meV at room temperature to 36.2 meV at 165°C; surprisingly, that for WS_2-Au@Ag NC ascents from 72.4 meV to 82 meV. To investigate the discrepancy, I employed a semiclassical model to theoretically study the thermal tendency of coupling strength κ[6]:

$$\kappa = \mu \sqrt{\frac{4\pi\hbar N c}{\lambda \varepsilon \varepsilon_o V}} \tag{3.8}$$

where μ, N, V, ε, ε_0, $\hbar$ and c correspond to transition dipole moment, the number of coupled excitons involved, the mode volume of the plasmonic nanocavity, ε indicates the dielectric constant of TMDC ML, the vacuum permittivity, Plank

constant and the speed of light. The V of the plasmonic Au@Ag NC open cavity and ε of TMDC MLs were assumed to be temperature insensitive[61,62,105]. Under the assumption of the thermal robust transition dipole moment of exciton, the polariton coupling strength is dominant by the thermal tendency in linear proportionality of a number of coupled bright excitons and excitonic oscillator strength, $f \propto N$. Combining previous argument and Eq. 3.8, it links proportionality between coupling strength and the square root of excitonic oscillator strength, i.e., $\kappa \propto f_{1/2}$. To check the mathematical relation, the coupling strength and exciton oscillator strength of two extreme temperatures 25 and 165 °C (κ_{165}/κ_{25} and $f_{165}/_{f25}$) are firstly compared. The κ_{165}/κ_{25} for MoS_2 (WS_2) polariton is approximately 0.58 (1.13), which is near the value 0.75 (1.06) of $(f_{165}/_{f25})^{1/2}$. This estimation probably affirms the conformity between coupling strength obtained from COM (Figure 3.8 (a) for MoS_2 and (b) for WS_2, respectively) and - oscillator strength obtained from $\Delta R/R_0$ (Figure 3.8 (c) for MoS_2 and (d) for WS_2).

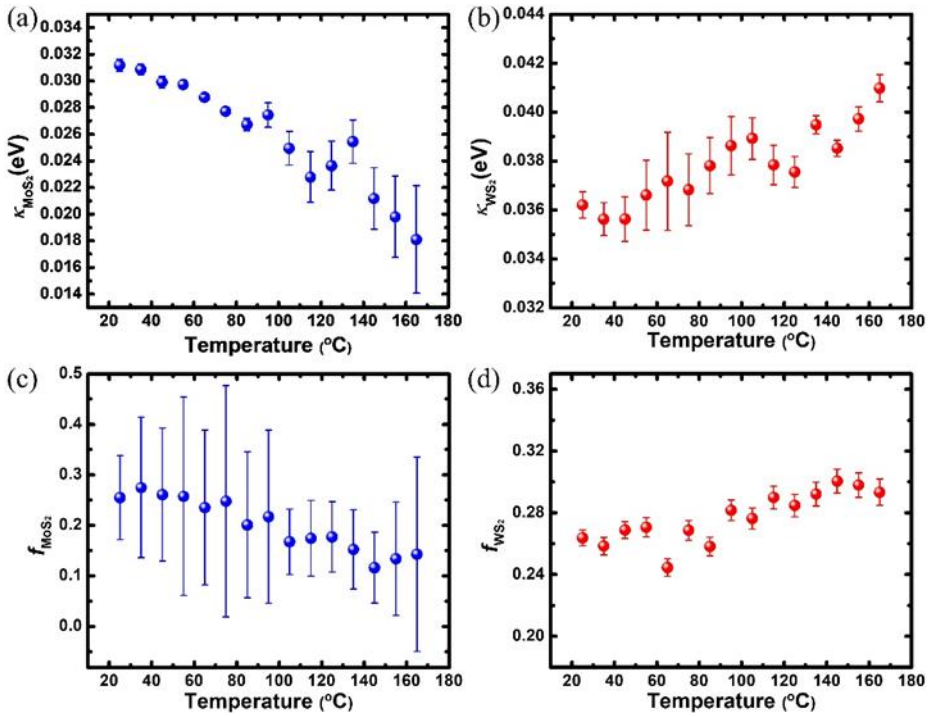

Figure 3.8 (a, b) Coupling strengths for (a) MoS_2-Au@Ag NC and (b) WS_2-Au@Ag NC hybrid systems obtained from COM. (c, d) oscillator strengths for bright A-exciton in (c) MoS_2 and (d) WS_2 MLs under elevating temperature obtained by Lorentz model fitting.

3.4 Numerical Study on WS_2-Au@Ag NC and MoS_2-Au@Ag NC Systems

Despite the nice conformity between coupling strength for polariton system and excitonic oscillator strength in TMDC MLs through the semiclassical model, there is still argument on the applicability of those initial approximations including thermally stable dipole moment and plasmonic mode distribution, and the validity of COM fitting under significant changes in a TMDC's dielectric properties at elevated temperatures. A numerical study is needed to validate the linkage between excitonic oscillator strength and polaritonic coupling strength under thermal tuning. For this reason, I performed numerical studies on the polariton states in the

WS_2/MoS_2-Au@Ag NC nanostructures through calculating the thermal tendency of scattering spectrums by finite element method (FEM). In the FEM simulation, the TEM imaging determined geometry and size parameters of Au@Ag NC are modelled with reasonable adjustment to account for the size inhomogeneity of actual nanostructures in order to match with measured scattering spectra. Without loss of generality, I only considered the variation of excitonic responses in TMDC MLs under elevated temperature and omitted the thermal enhanced plasmon dissipation in Au@Ag NCs. This simplified model is reasonable since the thermal enhanced plasmon dissipation occurs in both WS_2- and MoS_2 polariton systems, which would not emerge the reversal trends of coupling strength with temperature. Additionally, fixing the plasmonic response of Au@Ag NC prevents introducing additional uncertainty in the fitting process of COM, thereby giving an intuitive understanding of the thermal active excitonic response of the TMDCs in polariton systems. The dielectric function of WS_2 (MoS_2) ML was regarded as highly anisotropic dielectric material with a constant out-of-plane dielectric constant ε_{out} and an in-plane dielectric function $\varepsilon_{in}(E, T)$ with large background dielectric constant and thermal active single (double) Lorentz resonances term[106]:

$$\epsilon_{in}(E,T) = \epsilon_{\infty} + \frac{f_A(T)E_A^2(T)}{E_A^2(T) - E^2 - i\Gamma_A(T)E} \tag{3.9}$$

$$\epsilon_{in}(E,T) = \epsilon_{\infty} + \frac{f_A(T)E_A^2(T)}{E_A^2(T) - E^2 - i\Gamma_A(T)E} + \frac{f_B(T)E_B^2(T)}{E_B^2(T) - E^2 - i\Gamma_B(T)E} \tag{3.10}$$

With applying the previous mentioned uniaxial dielectric function of WS_2 ML, I firstly made a virtual control simulation on scattering properties from WS_2-Au@Ag NC polariton through tuning the excitonic oscillator strength (f_A) with fixing all the other excitonic properties (E_A = 2.024 eV and Γ_A = 0.055 eV were chosen to represent equivalent properties of WS_2 ML at 25 °C). By applying COM to fit the simulated scattering spectrums, I acquired the correlation between polariton coupling strength and exciton oscillator strength, which generally confirmed the $k \propto f^{1/2}$ relation as illustrated in Figure 3.10. Then, I further took into consideration of the thermal tendency of exciton energy and dissipation in the uniaxial dielectric function in TMDCs ML as illustrated by Eq. 3.9 and 3.10. Here, $E_{A/B}(T)$ follows O'Donnell's model (Eq. 3.2) in Figure 3.2 (a) and (b) with an energy shift $\Delta E_{A/B}$ based on the previous argument on the spatiality of exciton energy along the sample, and $\Gamma_{A/B}(T)$ obeys the linearity on temperature under single-phonon anti-Stokes scattering. The trend of oscillator strength $f_{A/B}$ for WS_2 (MoS_2) is modelled by a linear fit of values obtained from the measured $\Delta R/R_0$ spectra in Figure 3.8 (c) and (d). The actual values for the anisotropic dielectric function of WS_2 and MoS_2 ML used in the numerical study are enumerated in Table 1. We would like to stress that $\Gamma_{A/B}(0)$ for WS_2 ML is negative as the single-phonon anti-Stokes scattering model omits the excitonic damping's nonlinearity at low temperature, which leads to trival influence in ambient conditions. Employing the COM extracted values listed in Table 1 guarantees that thermal excitonic properties in numerical studies match with the experimental results.

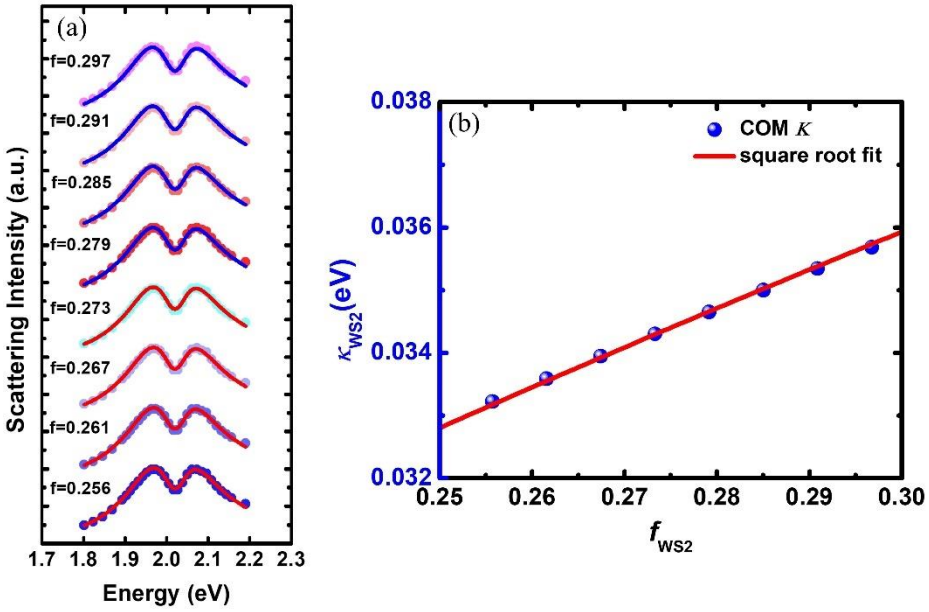

Figure 3.9 (a) Simulation of oscillator strength varying WS_2-Au@Ag NC with equal oscillator strength as WS_2-Au@Ag NC from 20 ºC to 165 ºC. (b) COM-extracted polariton coupling strength with respect to the exciton oscillator strength. The solid line denotes the square root fit with oscillator strength.

TMDC	ε_{out}	ε_{∞}	$E_{A/B}(0)$ [eV]	$s_{A/B}$	$\langle h\omega \rangle_{A/B}$ [eV]	$\Gamma_{A/B}(0)$ [eV]	$\alpha_{A/B}$	$\Delta E_{A/B}$ [eV]
WS_2	2.9	17.7	2.024	3.47	0.063	-0.064	4E-4	0.0214
MoS_2	2.8	21	1.89 / 2.02	3.15 / 7.61	0.06 / 0.111	0.091 / 1.38	1.38E-4 / 7.42E-4	0.03 / 0.037

Table 1. Parameters for Modeling the thermal active uniaxial dielectric function of WS_2 and MoS_2 ML

The simulated thermal tuning scattering spectra for both WS_2 and MoS_2 polariton systems are shown in Figures 3.10 (a) and 3.11 (a), in accord with the measured scattering spectra in Figure 3.5 (e) and (d), respectively. Afterwards, I applied the

COM to the simulation results to study the polariton (plasmon coupled A exciton) coupling strength with respect to the temperature. In the fitting procedure of COM, the plasmon resonance of Au@Ag NC nanocavity mode E_{pl} and dissipation rate Γ_{pl} were chosen as 2.007 eV for WS_2-Au@Ag NC polariton (1.957 eV for Au@Ag NC−MoS_2 polariton) and 0.235 eV for both systems to best fit the thermal tuning scattering spectra, while exciton resonance energy $E_{A/B}(T)$ and dissipation rate $\Gamma_{A/B}(T)$ were modelled by Eq. 3.2 and 3.3, respectively, with relevant values shown in Table 1. Apparently, the coupling strength for WS_2-based polariton obtained from COM fitting (see Figure 3.10 (b)) progressively grows with rising temperatures when coupling strength for MoS_2-based polariton (Figure 3.11 (b)) diminishes. Those simulated results of both WS_2- and MoS_2- based polariton demonstrated nice agreement with the experimental observations in Figure 3.8 (a) and (b). Curiously, $\kappa/f^{1/2}$ in these two polariton systems are generally unchanged, as illustrated in the insets of Figures 3.10 (b) and 3.11 (b), which agrees with the indication of Eq. 3.8. This strongly supports our observed anomalous reversal thermal tendency on WS_2/MoS_2 polariton systems. Moreover, the polariton coupling strengths obtained from COM fitting on the thermal tuning scattering spectra in the Au@Ag NC-WS_2 polariton system (Figure 3.10 (a)) and the control simulation (Figure 3.11 (a)) only demonstrate a very small deviation, which implies minor contribution of change of exciton energy and dissipation rate on the COM fitting. This result indirectly supports that $k \propto f^{1/2}$ dominates the thermal tendency of both polariton systems such that the variance of exciton energy and

dissipation alter little on the polariton coupling strength. Meanwhile, since the light-matter interaction is amplified by a plasmonic cavity, coupling strength performs an apparently larger signal-to-noise ratio (SNR) than oscillator strength. As a result, the coupling strength k in a polariton system might potentially serve as a probe to explore the spatial alteration of exciton oscillator strength f.

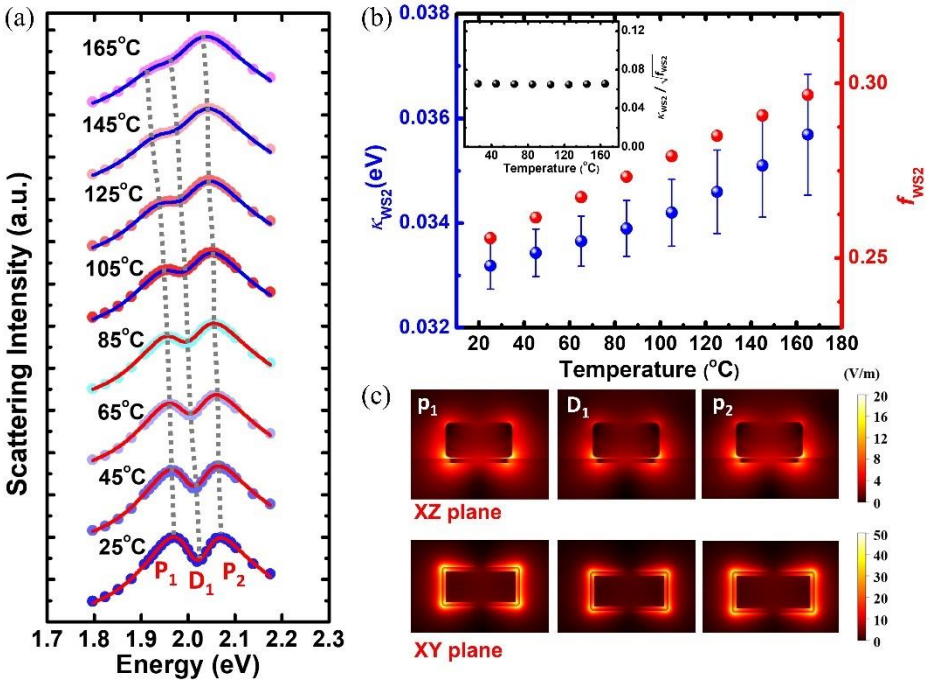

Figure 3.10 (a) Simulated thermal tendency of scattering spectrums for a single WS_2-Au@Ag NC ML nanosystem; (b) Model obtained coupling strength for the WS_2-Au@Ag polariton with respect to the temperature (blue dots). The thermal tendency of A-exciton oscillator strength of WS_2 (red dots) was modelled by a linear fit of the experimental results in Figure 3.8 (d). the ratio of coupling strength to the square root of oscillator strength is plotted in the inset; (c) Local-electric field distribution in the polariton systems at resonances P_1, D_1, and P_2 as marked in (a), with the upper part demonstrating the in-plane view and the bottom part showing the out-plane view of field distribution.

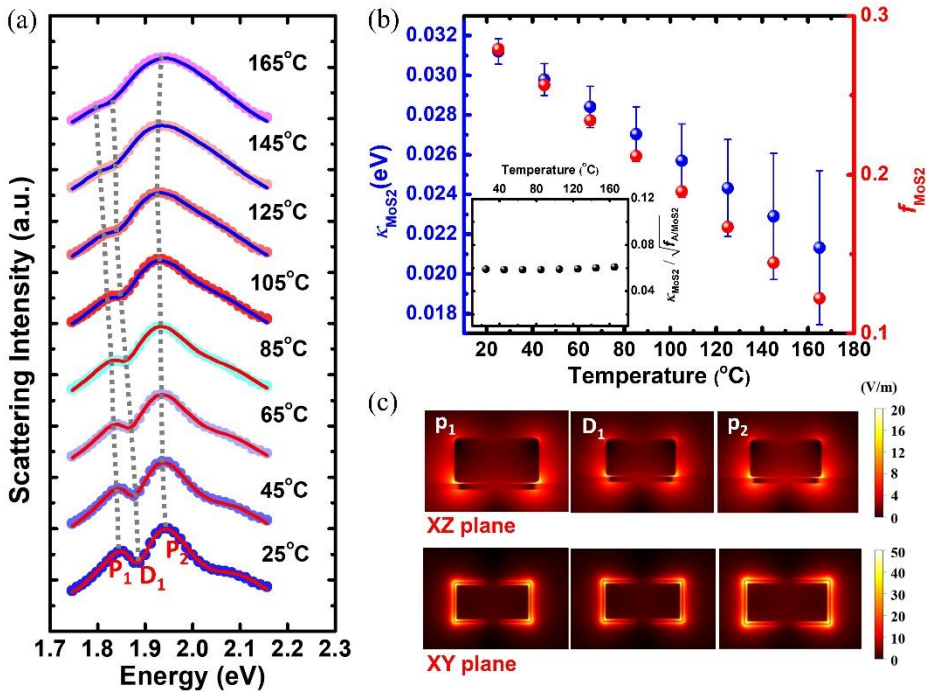

Figure 3.11 Similar simulation results to Figure 3.10 for a single MoS_2-Au@Ag NC.

Beyond previous spectral features, the strong polariton coupling in both hybridized nanostructures demonstrates novel features in their near-field distribution at hybridized resonances P_1, D_1, and P_2, as illustrated in Figures 3.10 (c) and 3.11 (c). At each resonance, the intense in-plane dielectric function of TMDC ML prompts the formation of image charges that interacts with the longitudinal dipole plasmon mode of Au@Ag NC, confining the corresponding mode volume at four cuboid corners in contact with TMDC ML and hence enhances the polariton coupling phenomenon. In short, owing to the cavity-enhanced exciton conductance, the near-field quenching effect exists in the Fano transparency window to dramatically suspend the corresponding local field[107].

After confirming the justifiability of the measured and simulated scattering spectrum, unveiling the origin in the opposite thermal tendency of oscillator strengths in MoS_2 and WS_2 ML became the center of this study. In general, the optical transition in a simple two-level system is governed by the densities of states in both ground and excited levels[108,109]. In the case of weak-field approximation, the external field modification of carrier density in the ground state is minor such that only the variation of carrier density in the excited state is necessary. Under this circumstance, the excitonic oscillator strength of this transition is linearly proportional to the transition dipole moment μ, exciton energy E_0 and exciton density N/V, i.e., $f \propto \mu E_0 N/V$[16]. The thermal tendency of exciton oscillator strength is thus jointly determined by those factors which might also be altered under elevated temperatures. Specifically, increasing the temperature usually results in a shrinking of N and E_0 due to raising dissociation of excitons and exciton−phonon interaction by thermal energy (~ 4% redshift in E_0 under the O'Donnell model with temperature changing from 25 ^oC to 165 ^oC), respectively. As a result, a weaker exciton oscillator strength is expected at higher temperatures. However, this general physical picture is unable to unveil the reversal thermal tendency for the A-exciton oscillator strength in WS_2 and MoS_2 and the corresponding polariton coupling strength, i.e., gradually raised coupling strength for the previous polariton system (about 10 % increases for the same temperature variation) yet rapidly fallen coupling strength for the latter polariton system (more than 30 % decreases).

To fully unveil the anomalous thermal tendency of the A-exciton oscillator strength in WS_2 and MoS_2, the dark excitons in both WS_2 and MoS_2 systems must be considered, which have a tens of meV energy derivation with respect to bright excitons[67,69,72,94]. As mentioned in the previous Chapter, these dark excitons are forbidden to interact with out-of-plane propagation light and are merely allowed to interact with in-plane propagating light[71]. This feature leads to an imperceptible optical transition of dark exciton in comparison with the bright excitons (as schemed by the green arrows in Figure 3.12). The dark exciton thereby is forbidden to couple with the longitudinal plasmon mode in those polariton systems. However, the population of bright excitons is altered by the existence of dark excitons due to the potential thermal redistribution of the population between those two states, as will be detailly discussed later. It implies that the presence of dark excitons potentially tailors the coupling strength of polariton systems in an indirect manner. Such influence of dark excitons on polariton systems has been unconsciously integrated in conventional COM through modifying the oscillator strength of A excitons. Consequently, the scattering spectra of those WS_2-/MoS_2 polariton systems are well described by COM without treating dark excitons as extra oscillators. Considering the tens of meV energy derivation (ΔE) between the bright and dark excitonic levels and the 26 meV (25°C) to 38 meV (165°C) average thermal energy (k_BT), the thermal-assisted transitions between those excitonic levels is considerable (as shown by the purple arrows in Figure 3.12), which

achieve equilibrium after thermalization of excitons. Assuming that the interaction between bright and dark excitonic states complies with a quasi-two-level system, it obeys a simple two-level Boltzmann distribution as $N_H = N_0 \exp(-\Delta E/k_BT)/(\exp(-\Delta E/k_BT) + 1)$ for the upper energy level and $N_L = N_0/(\exp(-\Delta E/k_BT) + 1)$ for the lower energy level. N_0, which denotes the population of total photoexcited excitons, is linearly proportional to the optical excitation. A similar analysis of exciton thermalization on two levels system was firstly conducted in a former study based on time-resolved PL in WSe_2 ML at cryogenic conditions[67]. The two-level Boltzmann distribution exhibits a decrease of density in the lower energy level and a corresponding increase of density in higher energy level under elevating temperature conditions. Earlier numerical studies discovered that the energy of dark exciton in MoX_2 ML (X = S or Se) is larger than the bright exciton's (see left panels of Figure 3.12 (a) and (b)), while dark exciton energy of the WX_2 ML is smaller than the bright exciton's (see right panels of Figure 3.12 (a) and (b))[67,69]. Correspondingly, under elevating temperatures, the bright excitons in MoS_2 has reduced oscillator strength and the bright excitons in WS_2 acquire oscillator strength. This physical picture qualitatively illustrates the reversal tendency results in WS_2/MoS_2 polariton and also introduces a unified image to explain former studies on thermal tuning oscillator strengths of MoS_2[106], $MoSe_2$[105], WS_2[101], and WSe_2[61] ML.

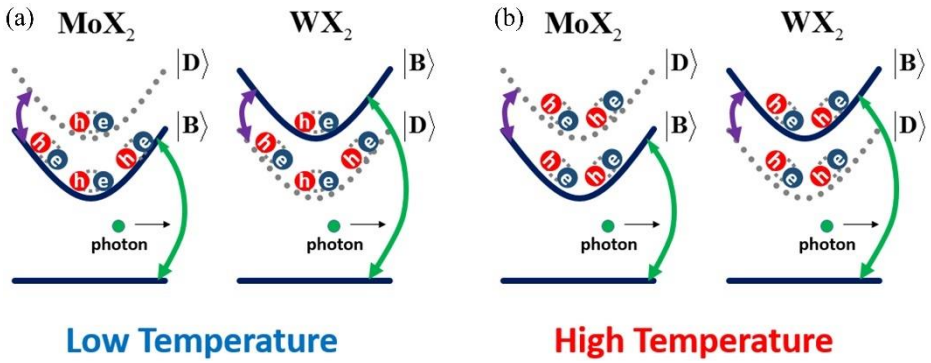

Figure 3.12 (a, b) Schematic representation of exciton densities of MoX_2 and WX_2 at low (a) and high (b) temperature. Solid black lines denote bright exciton states and gray dotted lines the dark exciton states. Solid green arrows represent the exciton radiation which is able to couple with plasmons mode. Solid purple arrows represent thermal induced transitions. Under rising temperature, the oscillator strength redistributes from low- to high-energy excitonic states, which consequently alters the density of bright exciton states coupled to the plasmonic nanocavity.

Through modelling the thermal tendency of coupling strength in the WS_2-Au@Ag NC polariton system shown in Figure 3.12 (b) with the simply two-level Boltzmann distribution, $N_H = N_0 \exp(-\Delta E/k_B T)/(\exp(-\Delta E/k_B T) + 1$, the relative energy of hidden dark excitonic state in WS_2 polariton system is approximately estimated. As shown in Figure 3.13, the energy derivation between bright and dark exciton states in WS_2 ML is 27 meV, which is around half of the former reported value (54 meV)[71]. The inconsistency between COM obtained value and the previously reported value might originate from the hidden coupling phenomenon between the bright exciton state and other states. Applying the model obtained ΔE values, investigating the variation of polariton coupling strength induced purely by the thermalization of excitonic population has been achievable. In the experimental temperatures (25 to 165°C), my model demonstrates a 12.4 %

coupling strength variation under the obtained energy deviation, which is considerably less than the 32.7 % variation from the reported energy deviation. It should be emphasized that as the energy derivation between two excitonic states is acquired through fitting the thermal tendency of coupling strength from COM, the dual fitting process may lead to the issues of accumulation of errors. This could be another potential reason for the difference of extracted energy deviation from the former experimental probed value at cryogenic temperatures[71].

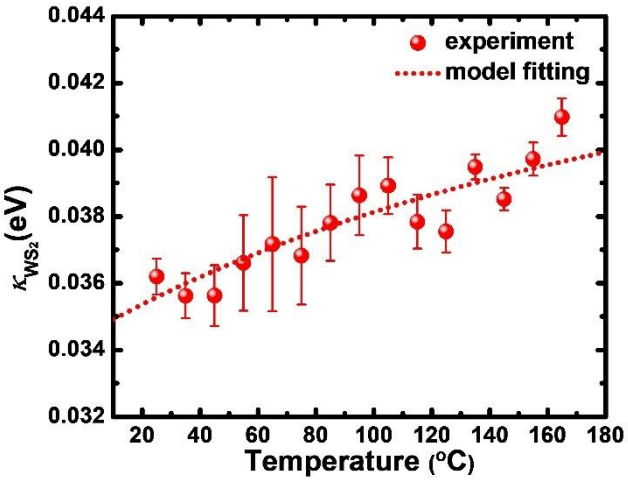

Figure 3.13 A two-level Boltzmann model fit of the temperature-dependent coupling strength shown in Figure 3.9 (b). The energy deviation between bright exciton and dark excitons, ΔE, is 27 meV.

Note that in the previous argument, the phenomenological model excludes the existence of charged exciton states (such as trion state) in discussing the thermalization of exciton to simplify the understanding. Since the trion state is a lower energy state than the bright exciton state in both WX_2 and MoX_2 ML, the occurrence of trions would intensify the bright exciton oscillator strength in both systems under elevating temperatures. This potential phenomenon contradicts the

measured reversal thermal tendency of exciton oscillator strength and polariton coupling strength for WS_2 and MoS_2 systems. To induce the presence of charged exciton states at room temperature or elevated temperature, significant doping on TMDC MLs through optical pumping, strong chemical doping, or electrical gating etc., is indispensable. Since no doping mechanisms were employed in the experiment, I excluded the influence of trion state to the model. Nevertheless, more detailed studies are required to quantitatively explore thermal tendency of oscillator strength TMDC MLs.

3.5 Conclusion

To conclude, I explored the thermal tendency of polariton coupling strength in MoS_2/WS_2-Au@Ag NC MLs, respectively. Employing the COM, I revealed reversal tendencies of the coupling strength for the two polariton systems, consistent with the thermal trend of A-exciton oscillator strength of pristine MoS_2/WS_2 ML. Applying COM parameters determined from experiment, numerical studies nicely agreed with the scattering spectrums of those two polariton systems and demonstrated a nearly constant $\kappa/f^{1/2}$ ratio as described in a cavity quantum electrodynamics model. Based on comprehensive studies on experiments and numerical studies, I introduced an intuitive two-level Boltzmann distribution phenomenological model which consists of energy arrangement of bright and dark excitons for performing reversal thermal energy (k_BT) activated redistribution of the excitons. This subsequently contributes to diminished

excitonic oscillator strength in MoS_2 ML yet raised excitonic oscillator strength in WS_2 ML, providing a unified physics picture of recently reported thermal tendency oscillator strengths of MoX_2 and WX_2. The results not only introduce a new vision for studying the thermal tendency of cavity−exciton strong coupling but also emphasize the importance of dark excitonic states in modulating the plasmon−bright-exciton coupling strength. It should be stressed that the reversal thermalization of excitonic density is essentially justified by the intrinsic exciton energy level of MoX_2 and WX_2 MLs and does not rely on the plasmonic properties of specific metallic nanostructures employed in the polariton system. It is expected that the thermal tailoring of plasmon bright-exciton coupling features is capable of exploring the fine structures of TMDC MLs. For example, it is potential to probe the local dark exciton energy more precisely by applying plasmon nanocavities with higher Q-factors and smaller model volumes to realize strong light-matter interaction.

Chapter 4 Studying Impact of Gap Thickness in Metal Nanoparticle on Mirror (NPoM) Structure on Bright Exciton Emission

Benefited from the direct bandgap nature of TMDCs ML, TMDCs perform facilitating properties in photonics and optoelectronics application, such as single-photon emitter, photodetectors and flexible optoelectronic diodes. However, the intrinsic quantum efficiency of pristine TMDC, such as MoS_2 ML, is usually less than 1 % owing to its considerable defect density. Therefore, various photonic approaches, such as dielectric cavity or plasmonic structure, have been proposed to enhance the PL emission of MoS_2 ML.

One of the most fundamental plasmonic nanostructures used for the PL enhancement of quantum emitter is the metallic nanosphere which behaves like optical nanoantennas. Through forming metal nanoparticle on-mirror (NPoM) structure, I present an extremely confined optical field inside the gap between the nanoparticle and mirror for enhancing light-matter interaction. The NPoM has demonstrated various potential applications such as nanoscale chemical reaction sensors, single-molecule polariton, and picocavity for surface-enhanced Raman scattering (SERS) of molecules, etc. Benefiting from the self-assembling nature of nanospheres on metallic mirror, NPoM is one of the simplest dimer structures to

form a sub-nanometer gap. However, in contrast to numerous researches on the various geometry of nanostructures, studies on the precise tuning of gap thickness are relatively limited. Considering the plasmonic hybridization between the dimer-like structure, the local field and density of state of NPoM have exponential relation to the thickness of the gap. As shown in previous studies, when the QE approaches the nanostructure, the PL usually experiences strong enhancement due to the strong local field enhancement and LDOS. While the QE is too close to the metallic surface (below 10 nm), the antenna efficiency diminishes and non-radiative decay dominates, which is termed photoluminescence quenching. These two effects compete in NPoM, highly depending on the thickness of the dielectric spacer. It is curious to utilize the potential of NPoM in PL enhancement of various excitonic states of TMDC through manipulating the gap thickness.

In this Chapter, I examine the critical role of dielectric spacer thickness in NPoM to intensify the PL of MoS_2. Different from tungsten-based TMDC (WX_2), molybdenum based TMDC (MoX_2) including MoS_2 consists of a bright exciton state with smaller energy than the dark exciton state. This property of MoS_2 advances the study of observation in plasmonic enhanced PL from purely bright exciton since the higher energy dark exciton is less favorable in radiation. Section 4.1 will briefly introduce the preparation process of MoS_2-NPoM structure. The spectroscopy results of both MoS_2-NPoM and MoS_2-AUNS systems will be introduced in section 4.2 to observe the experimental result of PL from those

structures with tuning the gap thickness. Section 4.3 will extend the study in numerical aspect through finite-difference time-domain method (FDTD) to explore potential reasons for optimizing PL at particular gap thickness. The conclusion will summarize the correlation between experimental and numerical results.

4.1 Sample Design

To conduct a statistical study on the MoS_2-NPoM system with various spacer thicknesses, I adopted the CVD grown MoS_2 ML in this experiment for large scale fabrication of the structure. I firstly tested the PL spectrum from reference sample MoS_2-SiO_2, as shown in Figure 4.1 (a), through wet-transferring MoS_2 MLs onto standard silicon wafer with 300 nm thick SiO_2. The MoS_2-NPoM system is shown in Figure 4.1 (d), where a gold mirror with a thickness of 150 nm is deposited between the MoS_2 ML and SiO_2 substrate through electron beam evaporation. The dispersed colloidal AUNS on top of MoS_2 ML has a diameter of 200 nm.

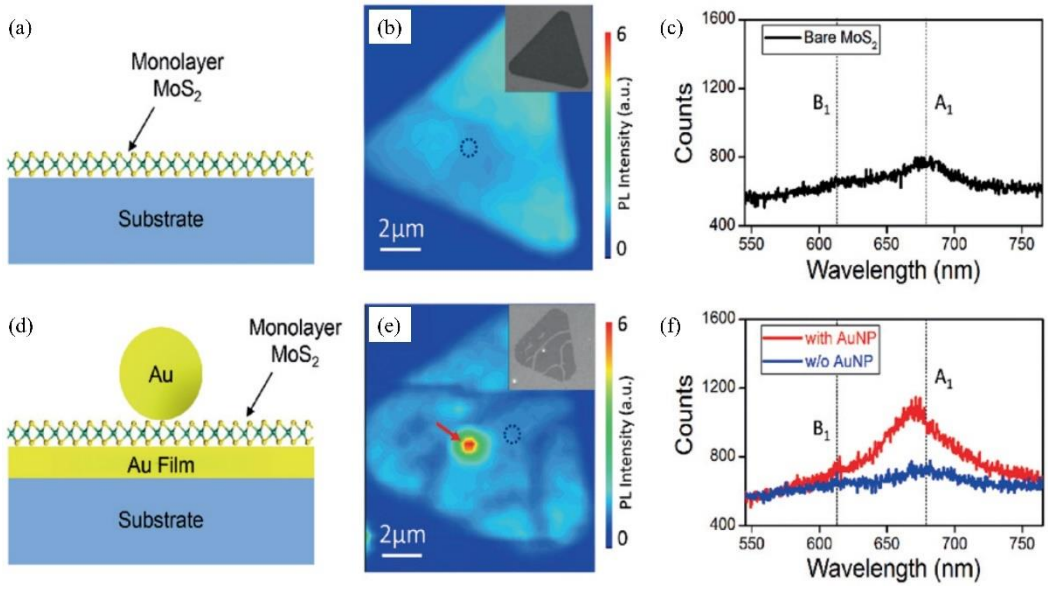

Figure 4.1 (a) Schematic representation of MoS_2 ML on a standard silicon substrate with 300 nm; (b) PL intensity map and SEM image of MoS_2 ML on a standard silicon substrate with 300 nm; (c) PL spectra of MoS_2 ML in (b) (black dashed circle); (d) Schematic representation of MoS_2-NPoM; (e) PL intensity map and SEM image of MoS_2-NPoM and MoS_2-Au mirror; (f) PL spectra of MoS_2 ML on the Au mirror with and without AUNSs (red and blue curves, respectively), corresponding to (e) (red arrow and black dashed circle, respectively).

4.2 Photoluminescence Spectroscopy on MoS_2-NPoM Structure

To explore the role of gap thickness in MoS_2-NPoM structure, the PL spectroscopy of both bare MoS_2-NPoM and MoS_2-AUNS were firstly examined (Figure 4.1). From a comparison of the PL mappings in Figure 4.1 (b) and (e), a near 6-fold PL enhancement was clearly observed at MoS_2-NPoM which was confirmed by the SEM image shown in insets of Figure 4.1 (b) and (e). The corresponding PL spectra of those local spots in Figure 4.1 (b) and (e) are shown in Figure 4.1 (c) and (f). The spectra (black curve) in Figure 4.1 (c) exhibits two peaks at 680 and 623 nm, which were termed as A and B exciton emission of MoS_2, are consistent with the previous studies for pristine MoS_2 ML[110]. The PL spectrum of MoS_2-NPoM exhibits a pronounced enhancement at the A exciton in comparison to MoS_2-Au mirror's. In this Chapter of study, I compared only the A exciton emission in studying PL enhancement. The counts at the A exciton emission were labelled as $N_{coupled}$ and N_{film} for the red and blue curves, respectively. To exclude the contribution the dark count N_{dark} of the spectrometer, the experimental observed PL enhancement factor is simply defined as $(N_{coupled}-N_{dark})/(N_{film}-N_{dark})$.

In our case, A ~ 600 value of dark count was observed through measuring the samples without laser excitation. To have a fair comparison, both the spectra of MoS_2-NPoM and MoS_2-Au mirror obtained from the same MoS_2 flake (red and blue curves) were used. In addition to the pronounced PL enhancement, a blue-shift of exciton emission was observed in MoS_2-NPoM in comparison to MoS_2-Au mirror. This might originate from plasmon induced dark exciton emission from the MoS_2-NPoM[71,72,94,111].

After realizing the PL enhancement effect of bare MoS_2-NPoM, I try to demonstrate the modification of the PL enhancement factor through introducing equal thickness dielectric spacer pairs between MoS_2 ML and the gold nanostructures. As illustrated in Figure 4.2 (a), two layers of Al_2O_3 with same thickness of t were deposited before and after MoS_2 ML was transferred onto the Au mirror. These formed spacers between MoS_2 and the plasmonic structures (i. e., Au mirror and AUNS), modifying the gap of NPoM structure, and hence thus modulated the local electric field in exciton excitation of MoS_2 and LDOS for enhancing exciton radiative decay. In Figure 4.2 (b-d), the measured PL for samples with different thickness are presented, where the thicknesses of Al_2O_3 spacer are t = 3 nm (Figure 4.2 (b)), t = 5 nm (Figure 4.2 (c)), and t = 7 nm (Figure 4.2 (d)), respectively. Similar to the previous bare MoS_2-NPoM, plasmonic enhanced PL was found in those local regions. As the previous spectrum of bare MoS_2-NPoM in Figure 4.1 (f) (t = 0 nm), the PL spectrums presented enhancement when AUNSs were involved. The A exciton emission experienced the best

enhancement when t = 5 nm. For t = 3 nm, since the PL from B exciton presented comparable PL to A exciton, the A exciton is not distinguishable.

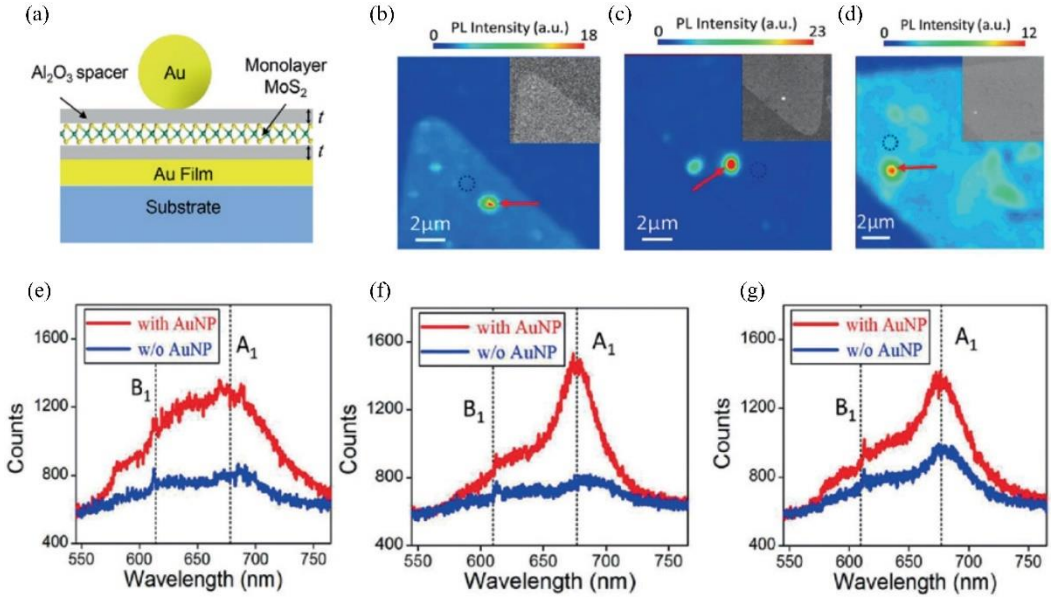

Figure 4.2 (a) Schematic representation of MoS_2-NPoM system with Al_2O_3 spacers. (b–d) PL intensity maps of MoS_2 ML samples. Insets: SEM image of each sample type. The thickness t of spacer is (b) 3 nm, (c) 5 nm and (d) 7 nm; (e–g) PL spectra of MoS_2 ML on Au mirror with and without AuNSs (red and blue curves), corresponding to the position in (b–d) (red arrow and black dashed circle, respectively).

The spacer thickness dependence of PL in MoS_2-NPoM is shown in Figure 4.3. The corresponding average PL enhancement factors are 4.38 for t = 0 nm, 6.89 for t = 3 nm, 7.74 for t = 5 nm and 2.22 for t = 7 nm, respectively. Thus, the enhancement factor of the MoS_2-NPoM system is maximized when the thickness of the Al_2O_3 spacer is 5 nm. Besides, I also redefine the enhancement factors as the average PL enhancement as shown in Figure 4.3. The full spectrum enhancement of average PL of the t = 3 nm samples was highest because of the broad spectra enhancement. However, in this study, since the focus was on the

enhancement phenomenon on only the A exciton emission rather than the full spectra enhancement, I would focus the discussion on the A exciton in the numerical study.

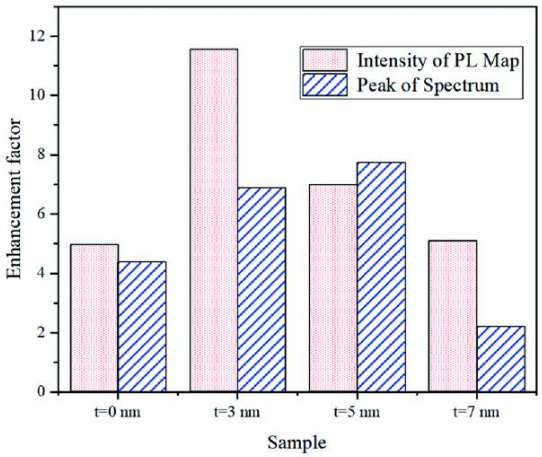

Figure 4.3 PL enhancement factors for the spectrums at the A exciton with different spacer thicknesses. The thickness of Al_2O_3 spacer was 0, 3, 5, and 7 nm. The red denotes the total intensity comparison of PL enhancement while the blue bar denotes the peak intensity comparison of PL enhancement.

4.3 Numerical Study on MoS_2-NPoM Structure with Tuning Al_2O_3 Layer

Figure 4.4 (a) presents the schematic diagram of numerical study in NPoM system with Al_2O_3 spacer (n = 1.5) thickness varying from 2 to 12 nm. For simplicity, MoS_2 ML was also treated as a dielectric spacer with a thickness of 1 nm in the numerical study[112]. Thus, the total spacer thickness altered from 3 to 13 nm to mimic the gap spacing variation of NPoM in the actual experiment. An in-plane dipole consisted of parallel or perpendicular polarization with respect to the

displace axis was used to denote the possible in-plane bright exciton emission from MoS_2 ML. In the actual experiment, the 532 nm laser was focused on the MoS_2-NPoM after passing through a 100X objective lens. However, as the excitonic responses in MoS_2 ML are highly susceptible to the in-plane polarized electric field, I concentrate the numerical study on the in-plane electric field component and also approximate the 532 nm Gaussian beam as a simple normal incidence plane wave. In the 532 nm excitation, the optical field distribution of MoS_2-NPoM is dominated by the transverse mode, as shown in Figure 4.4 (b). The optical mode confined in the gap is highly similar to electric quadrupole mode, which induces two hot spots in MoS_2 ML. The two hot spots, which consist of the intense out-of-plane electric field, show antiphase oscillation (Figure 4.4 (c)). When the gap widens, the localized electric field enhancement is reduced (Figure 4.4 (d)) due to the diminished coupling with the image charge in the gold mirror. There is equal contribution of PL from both orthogonal in-plane dipoles in the MoS_2-NPoM, since the degree of valley polarization in TMDC is minimal at room temperature. In addition, to approximate the plasmonic enhancement of PL from both A and B exciton, I employed Purcell effect $F(\omega)$ at 650 nm and antenna efficiency $\eta_a(\omega)$ to simulate the general plasmonic enhancement of radiation as following:

$$f_{em} = \frac{1}{(1-\eta_0(\omega))/F(\omega) + \eta_0(\omega)/\eta_a(\omega)}$$

(Eq. 4.1)

The intrinsic quantum efficiency $\eta_0(\omega)$ of MoS_2 is treated as 1 %[113]. As illustrated

in Figure 4.4 (e), the enhancement of in-plane dipole is limited when the width of gap in NPoM is at 3 nm. The PL enhancement rapidly raises as the spacer broadens until PL enhancement saturates at 9 nm. This could stem from the transition of NPoM's local field distribution from the quadrupole mode into the transverse dipole mode during the widening of the gap thickness. To review the details of optical mode distribution under 532 nm excitation, the in-plane view of electric field distribution is revealed in Figure 4.5, which shows the x- (Figure 4.5 (a)) and y- (Figure 4.5 (c)) components of the electric field for the 3 nm spacer thickness demonstrating more complex field patterns than that for the 13 nm spacer thickness (Figure 4.5 (b) and (d)) due to more intense mode hybridization in the former system. This strongly influences the excitation enhancement:

$$f_{ex} = \frac{|\mu \cdot E|^4}{|\mu \cdot E_o|^4}$$

(Eq. 4.2)

Through cooperative excitation enhancement f_{ex} and emission enhancement f_{em}, the total enhancement f_{tot} could be observed as:

$$f_{tot} = f_{ex} f_{em}$$

(Eq. 4.3)

As a result of quenched f_{em} and rising f_{ex} upon narrowing the spacing, the mean f_{tot} along the displace axis is optimized when the width of the spacer is near 8 nm (Figure 4.4 (e)), which is close to the experimental results (equivalent to 11 nm in simulation). Even though the simulation results only discuss the single diameter line distribution of emission enhancement rather than the total enhancement, it

provides a nice agreement with the experimental observation.

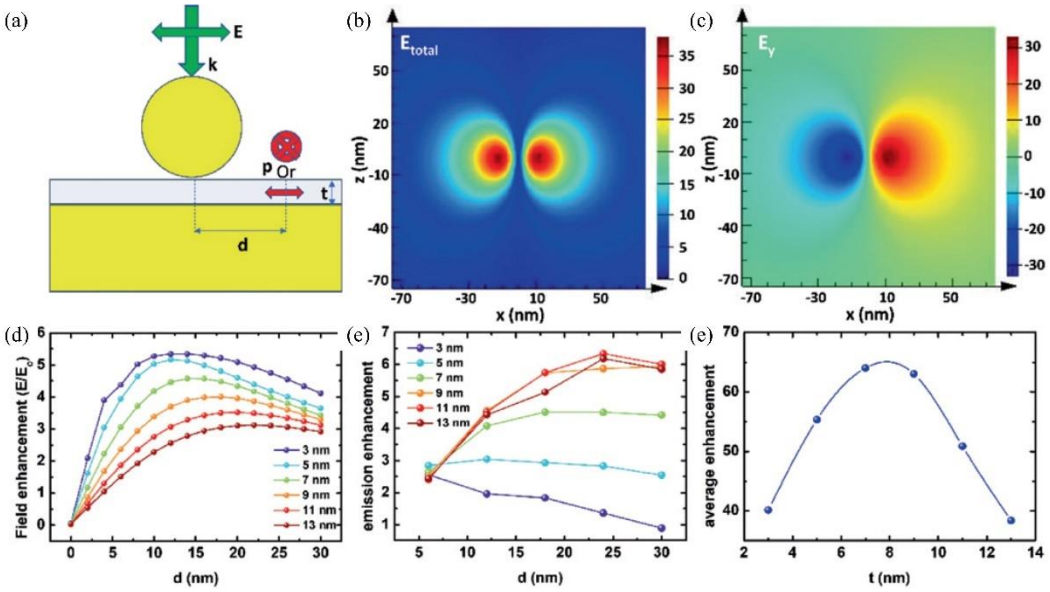

Figure 4.4 (a) Schematic diagram of MoS_2-NPoM simulation, green arrows corresponds to the direction of excitation and polarization of the 532 nm laser, while red arrows denote those two possible polarizations of in-plane dipole; (b) Near-field distribution of the middle region of the dielectric spacer at 532 nm excitation; (c) Near-field distribution of the out-of-plane field component; (d) Local field amplitude enhancement at 532 nm; (e) Dipole emission enhancement at 650 nm; (f) Average emission enhancement of the MoS_2-NPoM system as a function of spacer thicknesses.

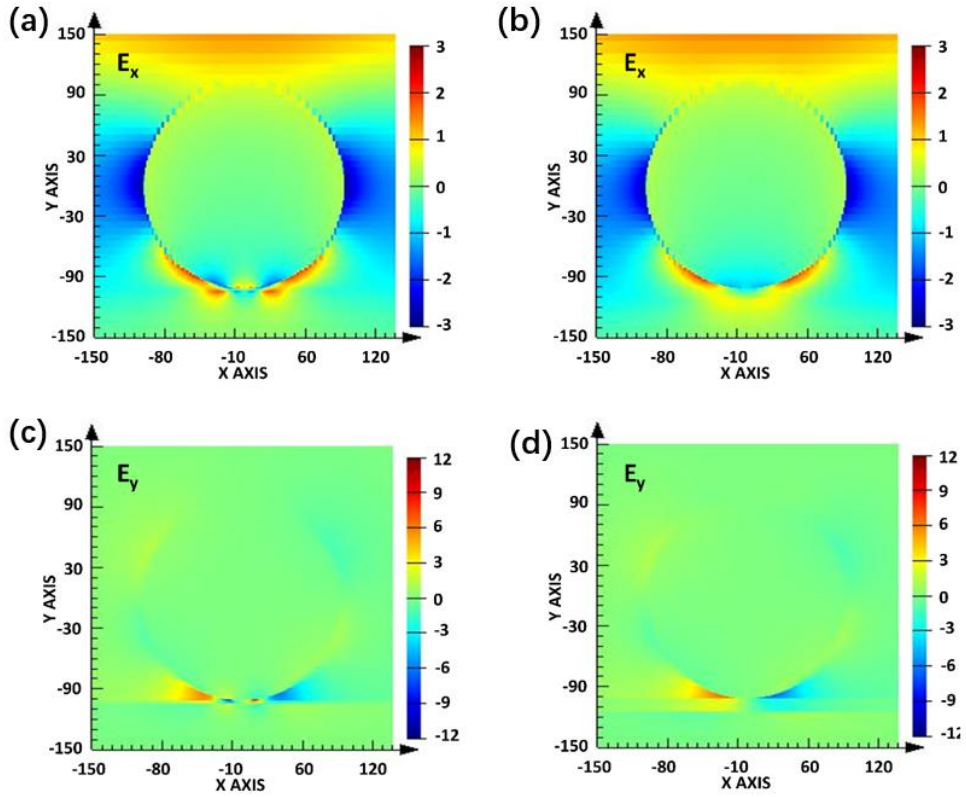

Figure 4.5 In-plane view of electric field distribution for (a) x-direction at 3 nm total thickness spacer system; (b) x-direction at 13 nm spacer total thickness system; (c) y-direction at 3 nm total thickness spacer system; (d) y-direction at 13 nm total thickness spacer system.

The potential reasons for the deviation between the simulated predictions and experimentally observed optimal spacer thickness is now discussed. The MoS_2-NPoM system in the numerical simulation is simply modelled as a perfect Au nanosphere placed on a perfectly flat Au mirror distanced by two smooth Al_2O_3 layers encapsulated MoS_2 ML. Those approximations deviate from the actual experimental conditions. The colloidal AUNS used in the experiment could consist of small facets inducing more complex resonances, such as cavity modes that hybridize with antenna modes in NPoM structure[114,115]. Meanwhile, the surface

roughness of Au mirror and Al_2O_3 layers might induce fluctuating features in the gap of NPoM and local strain in MoS_2[116], which both alters the PL enhancement and the even intrinsic quantum efficiency of MoS_2 ML.

4.4 Conclusion

I examined the PL enhancement of MoS_2 ML sandwiched in an NPoM nanocavity with tuning the thickness of Al_2O_3 spacer (i.e., the cavity gap thickness). The experimental reveals that a strong electric field does not always enhance the PL spectra distinctly. Through conducting a spacer thickness dependent PL measurement, I found the optimal thickness (t) of the Al_2O_3 spacer to be 5 nm. In the experiment, the MoS_2-NPoM system with a 5 nm spacer provided a 7.74 fold plasmonic enhancement of PL. Systematic numerical simulation revealed that the average PL enhancement of the system achieved maximum value at a spacer thickness of approximately 4 nm, which is close to the experimental result. The results could be widely applied in Purcell enhancement experiments with such NPoM configuration to enhance the radiation of in-plane dipole QEs.

Chapter 5 Probing the Dark Exciton Through Metal Nanoparticle on-Mirror (NPoM)

In TMDCs ML, as a result of broken inversion symmetry and strong SOI phenomenon, a spin-split of energy bands exists especially in the VB[93]. Considering the spin-split in CB is limited but nonzero, the electrons in the two corresponding states of the split CBs have spins with anti-parallel orientations[93]. These electrons in CBs are bound with the holes in relevant VB through Coulomb interaction, giving rise to the bright (X_O) and dark excitons (X_D)[93,111]. The recent symmetry analysis illustrates that bright and dark excitons consist of in-plane and out-of-plane dipoles, respectively[71]. Different from bright excitons, dark excitons have a much longer lifetime due to the non-radiative nature and the spin-flipping property during the transition process[94,117]. Such unique features of dark excitons have attracted enormous research interests for unusual photonics applications, such as coherent two-level systems for Bose-Einstein condensation[118] and quantum information processing[119]. However, the optical selection rules permit optical transitions when the spins state of carrier retains. Consequently, the loose dark exciton state emits an extremely low yield of photon, which is even unnoticeable at room temperature.

In this Chapter, I directly probe the PL from dark excitons of WSe_2 ML through

coupling with the gap plasmon mode in a NPoM nanocavity at ambient conditions. The gap plasmon mode consists of an intense vertical dipole moment that is able to efficiently interact with the out-of-plane dark excitons. In section 5.1, PL spectroscopy of reactive ion etched WSe_2 coupled with NPoM will be shown to reveal undiscovered radiation below the bright exciton energy as compared with unetched WSe_2 coupled with NPoM system. A double Lorentz fitting model was applied to quantify the corresponding resonance energy and intensity for bright and dark excitons which presented ~ 60 meV energy difference. The observed energy difference slightly deviates from the formerly reported values (40-50 meV) which might come from unanticipated local compressed strain due to the placing of Au nanoparticle or RIE etching process. In section 5.2, the results of numerical aperture (NA) dependent PL spectroscopy will be demonstrated to have direct evidence of coupling of out-of-plane dark exciton state and gap plasmon mode in NPoM. Section 5.3 will summarize the results of the experiments which demonstrates the distribution of a statistic with linewidth approximating the gap mode damping.

5.1 Dark Field Scattering and Photoluminescence Spectroscopy on WSe_2-NPoM Systems

Both former theoretical and experimental reports have accentuated the in-plane essence of bright exciton dipole and out-of-plane essence of dark exciton dipole as shown in Figure 5.1 (a)[71]. To simultaneously intensify the dark exciton emission

and quench the bright exciton emission, I applied gap plasmon mode of NPoM with a gap down to ~ 1 nm level to support intense LDOS for accelerating vertical dipole radiative decay. Figure 5.1 (b) illustrates the setup of the DF scattering and PL microscope system for measuring the optical features of unetched WSe_2-NPoM nanocavities and etched WSe_2-NPoM nanocavities as maintained in Chapter 2. The RIE process on WSe_2-NPoM was also conducted as according to the receipt in Chapter 2.

To realize intense LDOS for dark exciton radiation, a near resonance NPoM cavity was necessary to enhance the radiative decay. I employed DF scattering spectroscopy to examine the plasmonic properties of NPoM cavity with etched WSe_2 ML as shown in Figure 5.1 (c). The DF scattering for the etched WSe_2-NPoM nanocavity clearly reveals two resonance modes at 1.57 eV and beyond 2.05 eV which are gap mode and transverse mode, respectively. Note that no clear sign of Rabi splitting is observed in the DF scattering of the etched WSe_2-NPoM nanocavity under oblique white light illumination, indicating no strong plasmon-exciton coupling. On one hand, since the vertical plasmonic dipole moment associated with gap mode is orthogonal to bright excitons' in-plane dipole in WSe_2 ML, dipole orientation mismatch strongly inhibits effective electromagnetic coupling[35]. On the other hand, even though the gap plasmon mode of nanocavity has the same dipole alignment as that of the dark excitons in WSe_2 ML, the electromagnetic coupling between those two modes is inadequate to form strong

coupling since the transition dipole moment of the dark exciton is 2 to 3 orders of magnitude smaller than the bright exciton's[68,71,93]. The small transition dipole moment of dark excitons restricts the coupling strength with plasmonic nanocavity under weak illumination, leading to no polariton signature in DF scattering.

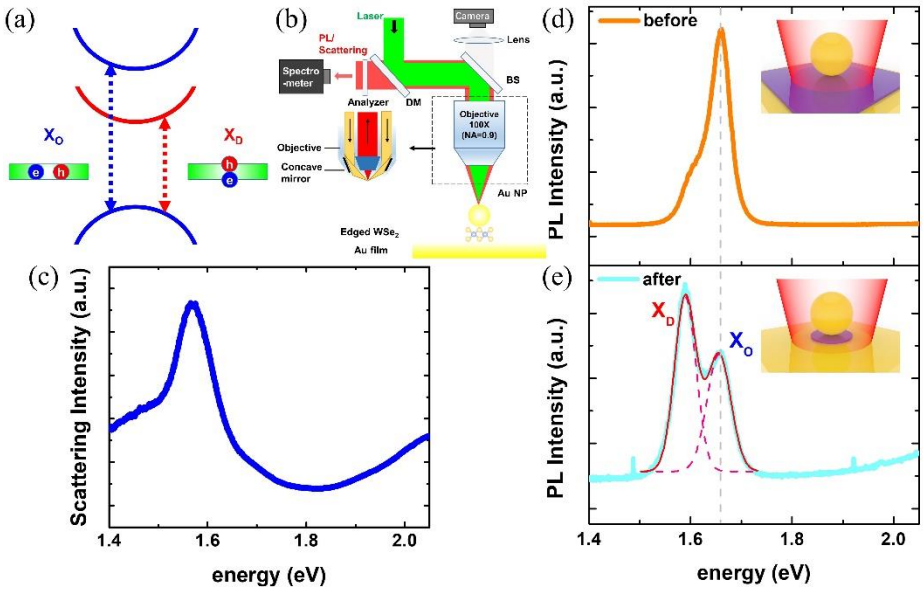

Figure 5.1 (a) Schematic diagram of dipole in bright- (left) and dark-exciton (right) with respect to TMDC ML. The energy diagram shows the spin configuration of bright exciton and dark exciton, respectively; (b) Schematic configuration of DF scattering and PL system. DM: dichroic mirror, BS: beam splitter; (c) Scattering spectra of the WSe_2-NPoM; (d, e) PL spectra from (d) unetched WSe_2-NPoM and (e) etched WSe_2-NPoM. Those inserts are those corresponding schematic diagrams of the nanostructure.

The local coupling efficiency of both bright and dark excitons at various position with NPoM strongly affects the overall PL spectrum. The spectra of single WSe_2-NPoM nanocavity before and after the etching process are demonstrated in Figure 5.1 (d, e) respectively. To prevent undesirable nonlinear emission from bi-exciton which exists in high power pumping[120–122], the optical density (OD) of 532 nm

excitation laser was diminished to 1.27 x 10^{10} W/cm^2. The PL spectrum of unetched WSe_2-NPoM in Figure 5.1 (d) illustrates a clear bright exciton emission at 1.66 eV with a small broad shoulder at a lower energy level. The broad shoulder might come from the mixing of dark exciton emission at both strongly enhanced section (gap regime) and weakly enhanced section (outside the gap) which present different emission features. To validate the physical origin, the weakly coupled part of WSe_2 ML flake was selectively etched out through directional argon ion bombardment in the RIE process. The etched WSe_2-NPoM demonstrates two apparent emissions at 1.66 eV and 1.6 eV (Figure 5.1 (e)). The 60 meV energy difference between those two states slightly differs from the previously reported energy difference (40-50 meV) between bright and dark exciton states[69,123]. This might come from the unexpected compressive strain in etched WSe_2 from the placing of AUNS[124] or during RIE etching process.

The ion beam irradiation process (such as electron irradiation or RIE) potentially induces chalcogen vacancies in WSe_2 for bounded exciton emission, which might be mixed up with dark exciton due to corresponding similar emission energy[125]. To verify the potential of defects bounded exciton emission from RIE-treated WSe_2, I examined the DF scattering and PL of the WSe_2-AUNS system on silica substrate as illustrated in Figure 5.2. Since the Au mirror has been changed to silica substrate (Figure 5.2 (a)), the DF scattering in Figure. 5.2 (b) presents only a broad electric dipole resonance beyond the interested regime. From the comparison of

PL spectroscopy on both unetched and etched WSe_2-AUNS systems on silica substrate (Figure 5.2 (c, d)), only the bright exciton emission presents in both spectra. This control experiment generally excluded the possibility of defect bounded exciton emission from RIE-treated WSe_2.

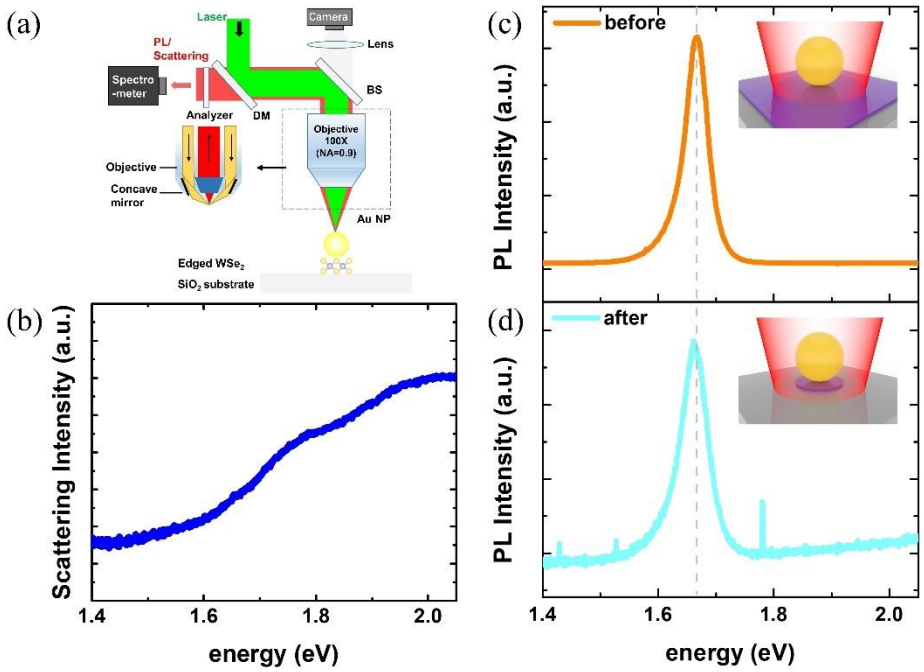

Figure 5.2 (a) Schematic configuration of DF scattering and PL system. DM: dichroic mirror, BS: beam splitter; (b) Scattering spectra of the WSe_2-AUNS system on silica substrate; (c, d) PL spectra from (c) unetched WSe_2-AUNS system on a silica substrate and (d) etched WSe_2-AUNS system on a silica substrate. Those inserts are those corresponding schematic diagrams of the nanostructure.

5.2 Directionality of Bright and Dark Exciton Coupled with Gap Plasmon Mode of NPoM

To reveal the detailed property of plasmonic nanocavity on the excitonic emission from WSe_2 ML, I then explored the directional emission properties of the etched WSe_2-NPoM through performing numerical aperture (NA) dependent PL spectroscopy. Figure 5.3 (a) and (b) show the PL spectrums of the same etched

WSe_2-NPoM nanocavity under 50X objective and 100X objective for both excitation and signal collective. As shown in the inset of Figure 5.3 (b), the ratio of dark exciton intensity to bright exciton intensity (A_D/A_O) changes from 0.53 to 1.32 when the objective changes from 50X to 100X. The dramatic variation of spectra was attributed to the collection angle in different objectives. With resonant coupling between gap plasmon mode and bright/dark exciton, their corresponding emission pattern is considerably altered by the plasmonic feature of gap mode. For this reason, I employed numerical simulation to study angular radiation pattern on gap mode in NPoM nanocavity through field transformation method replied on reciprocity arguments on the near field to far field transformation (NFFT)[126]. Unlike transverse mode, gap mode behaves like vertical bonding dipole mode in dimer nanostructure[42,43]. The radiation pattern on gap mode presents a cone-like emission shape (Figure 5.3 (c)). It slightly differs from the donut-like radiation pattern of the vertical dipole. As the presence of metal mirror introduces anisotropy of the dielectric environment, the radiation pattern is strongly reformed. In consideration of large negative dielectric function in metal and small positive dielectric constant in air, the vertical dipole of NPoM thus trends to radiate into the air rather than the metal mirror. The gap plasmon mode consequently radiates as a cone-link pattern toward the air side. By comparing the collection efficiency of gap mode under various NA shown in Figure 5.3 (d), the dramatic discrepancy can be observed. Since the dark exciton in NPoM is an out-of-plane dipole finely interacted with gap plasmon mode, the corresponding emission pattern mostly

obeys the gap plasmon radiation pattern. Consequently, the emission of dark exciton in WSe_2-NPoM system can only be selectively collected by a large NA objective in normal incidence PL spectroscopy. Meanwhile, due to the limited coupling between in-plane bright and gap mode, the corresponding radiation pattern exhibits a partial gap plasmon radiation pattern with keeping partial feature of in-plane dipole radiation. This clarifies the significant distinction of observed spectrums under 50X and 100X objectives' collection.

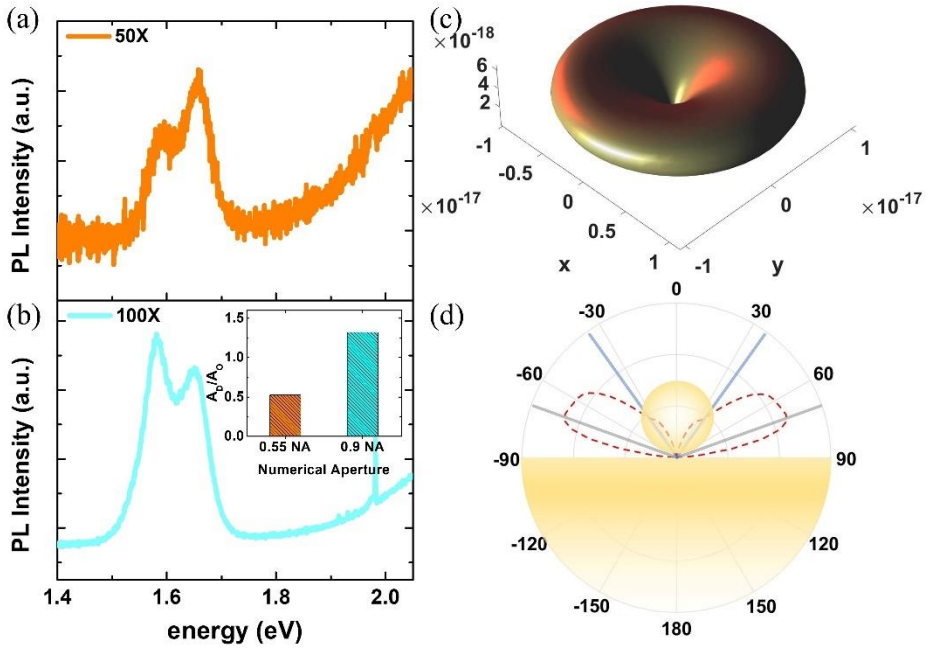

Figure 5.3 (a, b) PL spectra for a single etched WSe_2-NPoM nanocavity with (a) 50X objective (0.55 NA) and (b) 100X objective (0.9 NA) for excitation and collection. Insert shows the intensity ratio between the dark exciton to bright exciton at difference numerical aperture in experiment; (c) 3D simulation result of gap mode (1.6 eV) radiation pattern in NPoM; (d) 2D simulation result of gap mode (1.6 eV) radiation pattern in NPoM. Grey (Blue) line indicates the collection angle of 100X objective (50X objective).

5.3 Statistical Studies on Dark Exciton Emission Coupled with NPoM

To further study the two excitonic resonances in Figure 5.1 (e), I utilized double Lorentz fitting on the spectra of multiple etched WSe_2-NPoM nanocavities to conduct a statistical analysis on the corresponding radiation properties across various nanocavities. Figure 5.4 (a) presents the statistical emission energy of two distinct excitons states across various nanocavities. Consistent with the previous results in Figure 5.1 (e), the average energy difference between those two excitons states is ~ 60 meV. Curiously, the fluctuation of the dark exciton energy in PL spectrum is clearly larger than the bright exciton's. I believe the distinct sensitivity to dielectric screening between bright and dark exciton is the main cause of such a phenomenon. Considering the out-of-plane dipole nature of dark exciton, the dark exciton is anticipated to experience stronger influence from the local dielectric environment. Consequently, a small local variation of the dielectric environment has a considerable modification of dark exciton energy. The dielectric screening phenomenon might also lead to the derivation of the measured energy difference to the previously reported value. The PL enhancement from a coupling between gap plasmon mode in NPoM and dark exciton has been illustrated in Figure 5.4 (b). Across the statistical analysis of the intensity ratio of the dark exciton to bright exciton (A_D/A_O), a Lorentz like distribution with a peak at 20 meV detuning between dark exciton energy and plasmon energy was discovered. The ~ 100 meV linewidth of the resonant like feature in Figure 5.4 (b)

approximates to the measured linewidth in DF scattering of NPoM (Figure 5.1 (c)). It suggests that resonant like distribution of intensity ratio A_D/A_O originated from the gap plasmon mode resonant Purcell enhancement on dark exciton radiation. The small energy detuning between dark exciton and plasmon energy in resonance enhancement might arise from the small resonance mismatch between the near field and far field optical response which frequently exists in the large nanostructure.

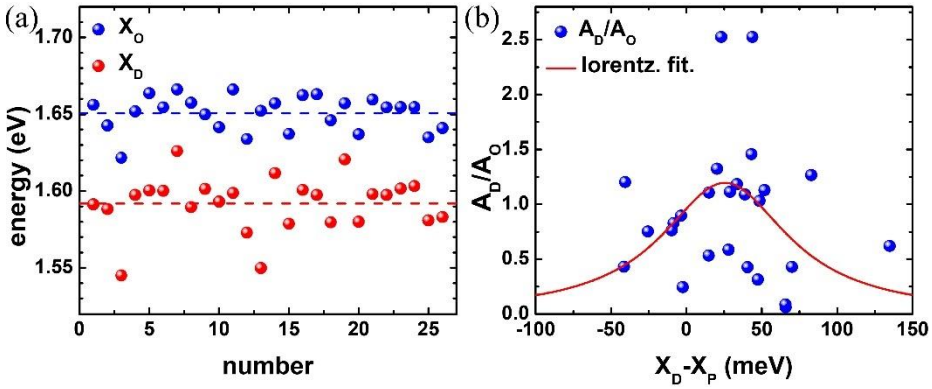

Figure 5.4 (a) Statistics of excitonic emission energy of both bright and dark exciton; (b) Ratio of the dark exciton to bright exciton emission intensity across energy detuning between plasmon energy and dark exciton energy.

5.4 Conclusion

In summary, I introduced an alternative nanoplasmonics approach to brighten the dark exciton in a WSe_2 ML at room temperature by sandwiching the ion etched WSe_2 ML inside a NPoM nanocavity. I unveiled that the gap mode of NPoM with a vertical plasmonic dipole moment consists of efficient coupling with the dark excitons of WSe_2 ML and leads to a strong PL due to enhanced radiative decay of the out-of-plane dipole inside the coupled nanocavity system, making the dark

excitons optically observable at room temperature. By varying the numerical aperture through switching objectives and employing a double Lorentz fitting model, I determined the emission properties of the bright and dark excitons including radiation pattern, emission energy, intensity and linewidth, matching with the theoretical understanding of plasmon-modulated radiation and radiative decay of a dipole located in the NPoM nanocavity. The findings open up flexibility in controlling excitonic emissions and probe the fine structures in the energy levels in TMDCs ML and find potential applications in polariton systems, paving the way for employing the dark excitons of TMDCs for nanophotonics and optoelectronic devices.

Chapter 6 Conclusion and Outlook

In this thesis, I demonstrated the studies on the coupling phenomenon of exciton in TMDC and plasmon mode in various colloidal plasmonic cavities. The spectroscopy ranging from the DF scattering to PL measurement were performed to fully understand the details of coupling phenomenon ranging from 1) role of dark exciton in Rabi oscillation of bright exciton and plasmon states, 2) Purcell enhanced LDOS of both bright exciton and quenching PL in poor antenna efficiency. 3) brightening dark exciton inWSe_2 in ultra-compact plasmonic structure.

To study the role of dark exciton in bright exciton based polariton, I carried out thermal tuning DF spectroscopy on WS_2-Au@Ag NC and MoS_2-Au@Ag NC systems which consisted of reversal order of energy level in dark exciton and bright exciton states. The DF spectroscopy revealed the rising coupling tendency in WS_2 based polariton and lessening coupling in MoS_2 based polariton under the elevated temperature circumstance. In the meantime, the $\Delta R/R_0$ spectroscopy revealed a similar phenomenon one excitonic oscillator strength in pristine WS_2 and MoS_2 ML. FEM numerical simulation was performed to check the validity of the experimental results which demonstrated nice agreement. The consistence between phonological model, experiment and simulation suggested the existence of underly physics on the anomalous tendency over those two polariton systems.

To understand the phenomenon of exciton dynamics, I introduced a two level model which was based on thermodynamics. Owing to the reverse order of bright and dark exciton states, bright exciton in WS_2 ML gained oscillator strength and bright exciton in MoS_2 ML lost oscillator strength under elevated temperatures. This phenomenon hence altered the thermal tendency of corresponding polariton systems to induce thermally robust WS_2 based polariton and fragile MoS_2 based polariton.

Besides the coupling phenomenon between horizontal plasmon mode and bright exciton, I performed PL spectroscopy on MoS_2-NPoM to explore other novel phenomena of vertical gap mode and bright exciton. To explore the hidden properties of MoS_2-NPoM in details, I utilized ALD to deposition equal thickness Al_2O_3 layers pair to distance MoS_2 from the AUNS and Au mirror under proper distance. An optimal spacer thickness (5 nm) was discovered through tuning the thickness of Al_2O_3 layers by controlling the cycle number of the deposition process. Numerical FDTD was performed to study the potential resonance of saturated PL enhancement. The results of the numerical study suggested that the rapidly decay optical antenna efficiency for in-plane exciton overwhelmed the saturated Purcell factor of the in-plane dipole at small spacing MoS_2-NPoM nanostructure. This clarified the necessity of proper engineering of the vertical plasmon mode and in-plane dipole to realize the strongest PL enhancement.

In light of the experimental observed PL quenching of bright exciton and potential enhancing dark exciton emission, I anticipated ultrasmall gap in NPoM can be utilized to brighten dark exciton radiation which was extremely challenging to be observed in room temperature conditions. As a demonstration, I performed the PL spectroscopy with switching objectives of various numerical apertures to confirm both directionality and spectrum of dark exciton emission in WSe_2-NPoM. FEM numerical studies have confirmed the consistency with the experimental results. It suggests another alternative scheme to realize dark exciton emission under room temperature condition.

Throughout this thesis, TMDC MLs have demonstrated fruitful excitonic responses which are able to couple with various plasmonic cavities. It opens up the numerical opportunity in forming novel phenomena ranging from strong coupling to enlightening dark exciton emission at room temperature. Further studies about mixing plasmonics and excitons in TMDC are expected in future to explore the additional novel phenomenon and even integrate into photonics circuit for actual applications.

Appendix

Transfer Matrix Study on the Differential Reflectance of a TMDC ML

I consider a pristine TMDC ML (region 2) sandwiched with two semi-infinite materials, air (region 1) and sapphire substrate (region 3). In $\Delta R/R_0$ measurement, since incident light transmits through the uniaxial principle axis of MoS_2 (WS_2), only in-plane dielectric permittivity of MoS_2 (WS_2) determines the impedance in reflection or transmission. Employing the transfer matrix method (TMM), the reflectance from the TMDC corresponds:

$$r = -\frac{(Z_3 - Z_2)(Z_2 + Z_1)e^{ik_2 a} + (Z_3 + Z_2)(Z_2 - Z_1)e^{-ik_2 a}}{(Z_3 - Z_2)(Z_2 - Z_1)e^{ik_2 a} + (Z_3 + Z_2)(Z_2 + Z_1)e^{-ik_2 a}} \tag{S1}$$

where $Z_i = (\mu_i\mu_0/\varepsilon_i\varepsilon_0)^{1/2}$ (i = 1, 2, 3) is the impedance of each region, k_2 and a the light wavevector and the TMDC ML thickness, ε_i and μ_i the relative permittivity and relative permeability. Considering all materials in the structure are non-magnetic in the optical regime, so μ_i = 1. Then Eq. (S1) is further rewritten:

$$r = -\frac{(\sqrt{\varepsilon_3} - \sqrt{\varepsilon_2})(\sqrt{\varepsilon_2} + \sqrt{\varepsilon_1})e^{i\sqrt{\varepsilon_2}k_0 a} + (\sqrt{\varepsilon_3} + \sqrt{\varepsilon_2})(\sqrt{\varepsilon_2} - \sqrt{\varepsilon_1})e^{-i\sqrt{\varepsilon_2}k_0 a}}{(\sqrt{\varepsilon_3} - \sqrt{\varepsilon_2})(\sqrt{\varepsilon_2} - \sqrt{\varepsilon_1})e^{i\sqrt{\varepsilon_2}k_0 a} + (\sqrt{\varepsilon_3} + \sqrt{\varepsilon_2})(\sqrt{\varepsilon_2} + \sqrt{\varepsilon_1})e^{-i\sqrt{\varepsilon_2}k_0 a}} \tag{S2}$$

As the thickness of TMDC ML is smaller than the wavelength of interest, $k_0 a \ll 1$. To simplify $k_0 a = \Delta$ and to take a first-order approximation of Δ, I can reduce Eq. (S2) as:

$$r$$

$$\approx -\frac{(\sqrt{\varepsilon_3}-\sqrt{\varepsilon_2})(\sqrt{\varepsilon_2}+\sqrt{\varepsilon_1})(1+\sqrt{\varepsilon_2}\Delta)+(\sqrt{\varepsilon_3}+\sqrt{\varepsilon_2})(\sqrt{\varepsilon_2}-\sqrt{\varepsilon_1})(1-\sqrt{\varepsilon_2}\Delta)}{(\sqrt{\varepsilon_3}-\sqrt{\varepsilon_2})(\sqrt{\varepsilon_2}-\sqrt{\varepsilon_1})(1+\sqrt{\varepsilon_2}\Delta)+(\sqrt{\varepsilon_3}+\sqrt{\varepsilon_2})(\sqrt{\varepsilon_2}+\sqrt{\varepsilon_1})(1-\sqrt{\varepsilon_2}\Delta)} \tag{S3}$$

By having several algebraic steps, simplify Eq. (S3) as follows:

$$r=\frac{\varepsilon_1-\varepsilon_3+2i\Delta(\sqrt{\varepsilon_1}\varepsilon_2-\sqrt{\varepsilon_1}\varepsilon_3)-\Delta^2(\varepsilon_1\varepsilon_3-\varepsilon_2^2)}{(\sqrt{\varepsilon_1}+\sqrt{\varepsilon_3})^2+\Delta^2(\sqrt{\varepsilon_1\varepsilon_3}+\varepsilon_2)^2} \tag{S4}$$

Based on the previous Δ argument, a second approximation was employed to eliminate the terms including Δ^2, Eq. (S4) becomes:

$$r\approx\frac{\sqrt{\varepsilon_1}-\sqrt{\varepsilon_3}}{\sqrt{\varepsilon_1}+\sqrt{\varepsilon_3}}+\frac{\sqrt{\varepsilon_1}\varepsilon_2-\sqrt{\varepsilon_1}\varepsilon_3}{(\sqrt{\varepsilon_1}+\sqrt{\varepsilon_3})^2}2ik_0a \tag{S5}$$

Defining $r_0=\left(\sqrt{\varepsilon_1}-\sqrt{\varepsilon_3}\right)/\left(\sqrt{\varepsilon_1}+\sqrt{\varepsilon_3}\right)$, $b=2\sqrt{\varepsilon_1}/\left(\sqrt{\varepsilon_1}+\sqrt{\varepsilon_3}\right)^2$, and $-b\varepsilon_3=d$, to obtain:

$$r=r_0+i\Delta b\varepsilon_2+i\Delta d \tag{S6}$$

where $\varepsilon_2=\varepsilon_2'+\varepsilon_2''$. Through several steps of simplifications:

$$R=r^2=r_0^2-2\Delta b\varepsilon_2''r_0+\Delta^2b^2[\varepsilon_2''^2+(\varepsilon_2'-\varepsilon_3)^2] \tag{S7}$$

eliminate Δ^2 related terms, one finally obtains:

$$\frac{\Delta R}{R_o}=\frac{R-R_o}{R_o}=-\frac{2\Delta b\varepsilon_2''r_0}{r_0^2}=-\frac{2\Delta b\varepsilon_2''r_0}{r_0^2} \tag{S8}$$

where R_0 is the reflectance from the substrate without TMDC ML. Lastly, consider the permittivity of WS_2/MoS_2 ML with two/three Lorentz resonators in the measured spectral region. By representing energy and thickness in a unit of eV and nm, the differential reflectance $\Delta R/R_0$ is defined as:

$$\frac{\Delta R}{R_O} = -\frac{\pi E}{310} a_{nm} \frac{b}{r_O} \left[\sum_{n=1}^{N} f_n \frac{E_n^2 \Gamma_n E}{(E_n^2 - E^2) + E^2 \Gamma_n^2} \right] \tag{S9}$$

which can be applied to fit the experimental spectrums and extract Lorentz parameters including resonance energy, damping rate and oscillator strength

COM Fitting Parameter of MoS_2 and WS_2 Coupled Polariton Systems

T (°C)	**A**	E_A **(eV)**	Γ_A **(eV)**	E_B **(eV)**	Γ_B **(eV)**	E_{pl} **(eV)**	Γ_{pl} **(eV)**	κ_A **(eV)**	κ_B **(eV)**
25	0.00118	1.88113	0.05893	2.03771	0.16521	1.96069	0.19707	0.03116	0.06204
35	0.00119	1.87536	0.06006	2.03112	0.17263	1.95934	0.19816	0.03085	0.0636
45	0.00116	1.87013	0.0612	2.02826	0.18005	1.95916	0.19925	0.02989	0.06419
55	0.00112	1.86504	0.06234	2.02345	0.18747	1.95852	0.20034	0.02972	0.06564
65	0.00119	1.86419	0.06348	2.01965	0.19489	1.95716	0.20143	0.02877	0.06489
75	0.00116	1.85837	0.06462	2.01394	0.20231	1.95484	0.20252	0.02771	0.06551
85	0.00119	1.85192	0.06576	2.00898	0.20973	1.95687	0.20361	0.02672	0.06687

95	0.00111	1.84536	0.0669	2.00023	0.21715	1.94854	0.2047	0.02744	0.0681
105	0.00114	1.84278	0.06803	2.00051	0.22457	1.95289	0.20579	0.02494	0.06741
115	0.00111	1.84016	0.06917	1.99943	0.23199	1.95941	0.20688	0.02278	0.06632
125	0.00112	1.83335	0.07031	1.99231	0.23941	1.95109	0.20797	0.02363	0.06839
135	0.00102	1.82653	0.07145	1.98423	0.24683	1.94408	0.20906	0.02543	0.07037
145	0.00112	1.81704	0.07259	1.98493	0.25425	1.95201	0.21015	0.02118	0.06832
155	0.0011	1.81635	0.07373	1.98007	0.26167	1.9506	0.21124	0.01979	0.06857
165	0.00104	1.8059	0.07486	1.97704	0.26909	1.94961	0.21233	0.01808	0.06804

Table A1 COM fitting parameter of MoS_2 polariton system

T (^oC)	**A**	**E_A (eV)**	**Γ_A (eV)**	**E_{pl} (eV)**	**Γ_{pl} (eV)**	**κ (eV)**
25	1.79E-04	2.02088	0.06467	2.00914	0.19707	0.0362
35	1.77E-04	2.02117	0.06682	2.01272	0.19816	0.03563
45	1.90E-04	2.01509	0.06897	2.01338	0.19925	0.03563
55	2.10E-04	2.01087	0.07111	2.01007	0.20034	0.03661
65	2.11E-04	2.00685	0.07326	2.01019	0.20143	0.03717
75	2.29E-04	2.00237	0.0754	2.0124	0.20252	0.03683
85	2.13E-04	1.99602	0.07755	2.00775	0.20361	0.03781
95	2.12E-04	1.9916	0.0797	2.00686	0.2047	0.03863
105	1.88E-04	1.98637	0.08184	2.00509	0.20579	0.03892
115	1.99E-04	1.98257	0.08399	2.00868	0.20688	0.03784

125	2.08E-04	1.97906	0.08613	2.0103	0.20797	0.03756
135	2.11E-04	1.97231	0.08828	2.00504	0.20906	0.03949
145	2.22E-04	1.9701	0.09043	2.00616	0.21015	0.03852
155	2.27E-04	1.96771	0.09257	2.00704	0.21124	0.03972
165	2.21E-04	1.96177	0.09472	2.00193	0.21233	0.04098

Table A2 COM fitting parameter of WS_2 polariton system

Reference

(1) Hugall, J. T.; Singh, A.; VanHulst, N. F.Plasmonic Cavity Coupling. *ACS Photonics* **2018**, *5* (1), 43–53.

(2) Vasa, P.; Lienau, C.Strong Light − Matter Interaction in Quantum Emitter/Metal Hybrid Nanostructures. *ACS Photonics* **2018**, *5*, 2–23.

(3) Baranov, D. G.; Cuadra, J.; Antosiewicz, T. J.; Shegai, T.Novel Nanostructures and Materials for Strong Light − Matter Interactions. *ACS Photonics* **2018**, *5*, 24–42.

(4) Nanoantennas, S.Single-Photon Nanoantennas. *ACS Photonics* **2017**, *4*, 710–722.

(5) Marquier, F.; Sauvan, C.; Greffet, J. J.Revisiting Quantum Optics with Surface Plasmons and Plasmonic Resonators. *ACS Photonics* **2017**, *4* (9), 2091–2101.

(6) Chikkaraddy, R.; DeNijs, B.; Benz, F.; Barrow, S. J.; Scherman, O. A.; Rosta, E.; Demetriadou, A.; Fox, P.; Hess, O.; Baumberg, J. J.Single-Molecule Strong Coupling at Room Temperature in Plasmonic Nanocavities. *Nature* **2016**, *535* (7610), 127–130.

(7) Kasprzak, J.; Richard, M.; Kundermann, S.; Baas, A.; Jeambrun, P.; Keeling, J. M. J.; Marchetti, F. M.; Szymánska, M. H.; André, R.; Staehli,

J. L.; et al.Bose-Einstein Condensation of Exciton Polaritons. *Nature* **2006**, *443* (7110), 409–414.

(8) Plumhof, J. D.; Stöferle, T.; Mai, L.; Scherf, U.; Mahrt, R. F.Room-Temperature Bose – Einstein Condensation of Cavity Exciton – Polaritons in a Polymer. *Nat. Mater.* **2014**, *13* (March), 247–252.

(9) Menon, V. M.; Deych, L. I.; Lisyansky, A. A.Towards Polaritonic Logic Circuits. *Nat. Photonics* **2010**, *4*, 345–346.

(10) Zhang, B.; Wang, Z.; Brodbeck, S.; Schneider, C.; Kamp, M.; Ho, S.Zero-Dimensional Polariton Laser in a Subwavelength Grating-Based Vertical Microcavity. *Light Sci. Appl.* **2014**, *3* (e135), 1–5.

(11) Kéna-Cohen, S.; Forrest, S. R.Room-Temperature Polariton Lasing in an Organic Single-Crystal Microcavity. *Nat. Photonics* **2010**, *4* (6), 371–375.

(12) Kim, S.; Zhang, B.; Wang, Z.; Fischer, J.; Brodbeck, S.; Kamp, M.; Schneider, C.; Höfling, S.; Deng, H.Coherent Polariton Laser. *Phys. Rev. X* **2016**, *6* (011026), 1–9.

(13) Flick, J.; Rivera, N.; Narang, P.Strong Light-Matter Coupling in Quantum Chemistry and Quantum Photonics. *Nanophotonics* **2018**, *7* (9), 1479–1501.

(14) Hennessy, K.; Badolato, A.; Winger, M.; Gerace, D.; Atatüre, M.; Gulde, S.; Fält, S.; Hu, E. L.; Imamoğlu, A.Quantum Nature of a Strongly Coupled Single Quantum Dot-Cavity System. *Nature* **2007**, *445* (7130), 896–899.

(15) Biagioni, P.; Huang, J.; Hecht, B.Nanoantennas for Visible and Infrared Radiation. *Reports Prog. Phys. Nanoantennas* **2012**, *75*, 024402.

(16) Törmö, P.; Barnes, W. L.Strong Coupling between Surface Plasmon Polaritons and Emitters: A Review. *Reports Prog. Phys.* **2015**, *78* (1).

(17) Physik, S.; Mfinchen, D. U.Excitation of Nonradiative Surface Plasma Waves in Silver by the Method of Frustrated Total Reflection. *Zeitschrift ffir Phys.* **1968**, *216*, 398–410.

(18) Physik, A.Radiative Decay of Non Radiative Surface Plasmons Excited by Light. *Z. Naturforsch.* **1968**, *23* (a), 2135–2136.

(19) London, T.; Philosophical, D.On a Remarkable Case of Uneven Distribution of Light in a Diffraction Grating Spectrum. *London, Edinburgh, Dublin Philos. Mag. J. Sci.* **1902**, *4* (21), 396–402.

(20) Barnes, W. L.; Preist, T. W.; Kitson, S. C.; Sambles, J. R.Physical Origin of Photonic Energy Gaps in the Propagation of Surface Plasmons on Gratings. *Phys. Rev. B* **1996**, *54* (9), 6227–6244.

(21) Bohren, C. F.; Huffman, D. R.*Absorption and Scattering of Light by Small Particles*; 1998.

(22) Hutter, B. E.; Fendler, J. H.Exploitation of Localized Surface Plasmon Resonance. *Adv. Mater.* **2004**, *16* (19), 1685–1706.

(23) Funston, A. M.; Novo, C.; Mulvaney, P.; Liz-marza, L. M.Modelling the

Optical Response of Gold Nanoparticles. *Chem. Soc. Rev.* **2008**, *37*, 1792–1805.

(24) Hightower, R. L.Resonant Mie Scattering from a Layered Sphere. *Appl. Opt.* **1988**, *27* (23), 4850–4855.

(25) Larkin, B. K.Scattering of Electromagnetic Waves from Concentric Infinite Cylinders. *J. Opt. Soc. Am.* **1961**, *51* (5), 506–508.

(26) Kaloss, M.; Broscius, C.; Nienhuis, A. W.; Foroni, L.; Kaneko, Y.; Perutz, M. F.; Loos, U.; Ludwig, W. D.; Rehg, J. E.; Goorha, R. M.; et al.A Hybridization Model for the Plasmon Response of Complex Nanostructures. *SC* **2003**, *302* (October), 419–423.

(27) Nordlander, P.; Oubre, C.; Prodan, E.; Li, K.; Stockman, M. I.Plasmon Hybridization in Nanoparticle Dimers. *Nano Lett.* **2004**, *4* (5), 899–903.

(28) Zhang, Q.; Cai, X.; Yu, X.; Carregal-romero, S.; Parak, W. J.Electron Energy-Loss Spectroscopy of Spatial Nonlocality and Quantum Tunneling Effects in the Bright and Dark Plasmon Modes of Gold Nanosphere Dimers. *Adv. Qauntum Technol.* **2018**, *1800016*, 1–12.

(29) Baur, S.; Sanders, S.; Manjavacas, A.Hybridization of Lattice Resonances. *ACS Nano* **2018**, *12*, 1618–1629.

(30) You, A.; Be, M. A. Y.; In, I.Plasmon Hybridization in Spherical Nanoparticles. *J. Chem. Phys.* **2004**, *120* (5444).

(31) Benz, F.; Chikkaraddy, R.; Salmon, A.; Ohadi, H.; Nijs, B.De; Mertens, J.; Carnegie, C.; Bowman, R. W.; Baumberg, J. J.SERS of Individual Nanoparticles on a Mirror: Size Does Matter, but so Does Shape. *J. Phys. Chem. Lett.* **2016**, *7*, 2264–2269.

(32) Sigle, D. O.; Hugall, J. T.; Ithurria, S.; Dubertret, B.; Baumberg, J. J.Probing Confined Phonon Modes in Individual CdSe Nanoplatelets Using Surface-Enhanced Raman Scattering. *Phys. Rev. Lett.* **2014**, *113* (087402), 1–5.

(33) Chen, S.; Zhang, Y.; Shih, T.; Yang, W.; Hu, S.; Hu, X.; Li, J.; Ren, B.; Mao, B.; Yang, Z.; et al.Plasmon-Induced Magnetic Resonance Enhanced Raman Spectroscopy. *Nano Lett.* **2018**, *18* (4), 2209–2216.

(34) Mertens, J.; Kleemann, M.; Chikkaraddy, R.; Narang, P.; Baumberg, J. J.How Light Is Emitted by Plasmonic Metals. *Nano Lett.* **2017**, *17*, 2568–2574.

(35) Kleemann, M. E.; Chikkaraddy, R.; Alexeev, E. M.; Kos, D.; Carnegie, C.; Deacon, W.; DePury, A. C.; Große, C.; DeNijs, B.; Mertens, J.; et al.Strong-Coupling of WSe2in Ultra-Compact Plasmonic Nanocavities at Room Temperature. *Nat. Commun.* **2017**, *8* (1).

(36) Gittinger, M.; Höflich, K.; Smirnov, V.; Kollmann, H.; Lienau, C.Strongly Coupled , High-Quality Plasmonic Dimer Antennas Fabricated Using a Sketch-and-Peel Technique. *Nanophotonics* **2020**, *9* (2), 401–412.

(37) Chen, W.; Zhang, S.; Kang, M.; Liu, W.; Ou, Z.; Li, Y.; Zhang, Y.; Guan, Z.; Xu, H.Probing the Limits of Plasmonic Enhancement Using a Two-Dimensional Atomic Crystal Probe. *Light Sci. Appl.* **2018**, *7* (56).

(38) Nordlander, P.; Prodan, E.Plasmon Hybridization in Nanoparticles near Metallic Surfaces. *Nano Lett.* **2004**, *4* (11), 2209–2213.

(39) Le, F.; Lwin, N. Z.; Steele, J. M.; Ka, M.Plasmons in the Metallic Nanoparticle − Film System as a Tunable Impurity Problem. *Nano Lett.* **2005**, *5* (10), 2009–2013.

(40) Nijs, B.De; Bowman, R. W.; Herrmann, L. O.; Benz, F.; Barrow, S. J.; Mertens, J.; Sigle, D. O.; Chikkaraddy, R.; Eiden, A.; Ferrari, A.; et al.Unfolding the Contents of Sub-Nm Plasmonic Gaps Using Normalising Plasmon Resonance Spectroscopy. *Faraday Discuss.* **2015**, *178*, 185–193.

(41) Mertens, J.; Eiden, A. L.; Sigle, D. O.; Huang, F.; Lombardo, A.; Sun, Z.; Sundaram, R. S.; Colli, A.; Tserkezis, C.; Aizpurua, J.; et al.Controlling Subnanometer Gaps in Plasmonic Dimers Using Graphene. *Nano Lett.* **2013**, *13*, 5033–5038.

(42) Li, G.-C.; Zhang, Y.-L.; Lei, D. Y.Hybrid Plasmonic Gap Modes in Metal Film-Coupled Dimers and Their Physical Origins Revealed by Polarization Resolved Dark Field Spectroscopy. *Nanoscale* **2016**, *8* (13), 7119–7126.

(43) Zhang, Q.; Li, G. C.; Lo, T. W.; Lei, D. Y.Polarization-Resolved Optical

Response of Plasmonic Particle-on-Film Nanocavities. *J. Opt. (United Kingdom)* **2018**, *20* (2), 024010.

(44) Chikkaraddy, R.; Turek, V. A.; Kongsuwan, N.; Benz, F.; Carnegie, C.; Goor, T.Van De; Nijs, B.De; Demetriadou, A.; Hess, O.; Keyser, U. F.; et al.Mapping Nanoscale Hotspots with Single-Molecule Emitters Assembled into Plasmonic Nanocavities Using DNA Origami. *Nano Lett.* **2018**, *18* (1), 405–411.

(45) Cormier, S.; Ding, T.; Turek, V.; Baumberg, J. J.Actuating Single Nano-Oscillators with Light. *Adv. Opt. Mater.* **2018**, *1701281*, 1–5.

(46) Hill, R. T.; Mock, J. J.; Hucknall, A.; Wolter, S. D.; Jokerst, N. M.; Smith, D. R.; Al, H. E. T.Plasmon Ruler with Angstrom Length Resolution. *ACS Nano* **2012**, No. 10, 9237–9246.

(47) Mock, J. J.; Hill, R. T.; Degiron, A.; Zauscher, S.; Chilkoti, A.; Smith, D. R.Distance-Dependent Plasmon Resonant Coupling between a Gold Nanoparticle and Gold Film 2008. *Nano Lett.* **2008**, *8* (8), 2245–2252.

(48) Ciracì, C.; Hill, R. T.; Mock, J. J.; Urzhumov, Y.; Maier, S. A.; Pendry, J. B.; Chilkoti, A.; Smith, D. R.Probing the Ultimate Limits of Plasmonic Enhancement. *Science (80-.).* **2012**, *337* (August), 1072–1075.

(49) Scholl, J. A.; Garc, A.; Koh, A. L.; Dionne, J. A.Observation of Quantum Tunneling between Two Plasmonic Nanoparticles. *Nano Lett.* **2013**, *13*,

564–569.

(50) Chernikov, A.; Berkelbach, T. C.; Hill, H. M.; Rigosi, A.; Li, Y.; Aslan, O. B.; Reichman, D. R.; Hybertsen, M. S.; Heinz, T. F.Exciton Binding Energy and Nonhydrogenic Rydberg Series in Monolayer WS2. *Phys. Rev. Lett.* **2014**, *076802* (August), 1–5.

(51) Zhu, B.; Chen, X.; Cui, X.Exciton Binding Energy of Monolayer WS2. *Sci. Rep.* **2015**, *5*.

(52) Mak, K. F.; Lee, C.; Hone, J.; Shan, J.; Heinz, T. F.Atomically Thin MoS2: A New Direct-Gap Semiconductor. *Phys. Rev. Lett.* **2010**, *105* (13), 2–5.

(53) Xiao, D.; Liu, G.; Feng, W.; Xu, X.; Yao, W.Coupled Spin and Valley Physics in Monolayers of MoS2 and Other Group-VI Dichalcogenides. *Phys. Rev. Lett.* **2012**, *196802* (May), 1–5.

(54) Zeng, H.; Dai, J.; Yao, W.; Xiao, D.; Cui, X.Valley Polarization in MoS2 Monolayers by Optical Pumping. *Nat. Mater.* **2012**, *7* (June), 490–493.

(55) Xu, X.; Yao, W.; Xiao, D.; Heinz, T. F.Spin and Pseudospins in Layered Transition Metal Dichalcogenides. *Nat. Phys.* **2014**, *10* (May), 343–350.

(56) Wang, G.; Heinz, T. F.Colloquium : Excitons in Atomically Thin Transition Metal Dichalcogenides. *Rev. Mod. Phys.* **2018**, *90* (2), 21001.

(57) Ye, Z.; Cao, T.; Brien, K. O.; Zhu, H.; Yin, X.; Wang, Y.; Louie, S. G.; Zhang, X.Probing Excitonic Dark States in Single-Layer Tungsten

Disulphide. *Nature* **2014**, *513* (7517), 214–218.

(58) Wang, G.; Marie, X.; Gerber, I.; Amand, T.; Lagarde, D.; Bouet, L.; Vidal, M.; Balocchi, A.; Urbaszek, B.Giant Enhancement of the Optical Second-Harmonic Emission of WSe 2 Monolayers by Laser Excitation at Exciton Resonances. *Phys. Rev. Lett.* **2015**, *097403* (MARCH), 1–6.

(59) Xiao, J.; Ye, Z.; Wang, Y.; Zhu, H.; Wang, Y.; Zhang, X.Nonlinear Optical Selection Rule Based on Valley-Exciton Locking in Monolayer Ws 2. *Light Sci. Appl.* **2015**, No. August, 1–6.

(60) Li, Y.; Chernikov, A.; Zhang, X.; Rigosi, A.; Hill, H. M.; Van DerZande, A. M.; Chenet, D. A.; Shih, E. M.; Hone, J.; Heinz, T. F.Measurement of the Optical Dielectric Function of Monolayer Transition-Metal Dichalcogenides: MoS2, MoSe2, WS2, and WSe2. *Phys. Rev. B - Condens. Matter Mater. Phys.* **2014**, *90* (20), 1–6.

(61) Arora, A.; Koperski, M.; Nogajewski, K.; Marcus, J.; Faugeras, C.; Potemski, M.Excitonic Resonances in Thin Films of WSe2: From Monolayer to Bulk Material. *Nanoscale* **2015**, *7*, 10421–10429.

(62) Arora, A.; Nogajewski, K.; Molas, M. R.; Koperski, M.; Potemski, M.Exciton Band Structure in Layered MoSe2: From a Monolayer to the Bulk Limit. *Nanoscale* **2015**, *7*, 20769–20775.

(63) Kozawa, D.; Kumar, R.; Carvalho, A.; Amara, K. K.; Zhao, W.; Wang, S.;

Toh, M.; Ribeiro, R. M.; Neto, A. H. C.; Matsuda, K.; et al.Photocarrier Relaxation Pathway in Two-Dimensional Semiconducting Transition Metal Dichalcogenides. *Nat. Commun.* **2014**, *r* (4543), 1–7.

(64) Verre, R.; Baranov, D. G.; Munkhbat, B.; Cuadra, J.; Käll, M.; Shegai, T.Transition Metal Dichalcogenide Nanodisks as High-Index Dielectric Mie Nanoresonators. *Nat. Nanotechnol.* **2019**, *14* (July), 679–684.

(65) Green, T. D.; Baranov, D. G.; Munkhbat, B.; Verre, R.; Shegai, T.; Käll1, M.Optical Material Anisotropy in High-Index Transition Metal Dichalcogenide Mie Nanoresonators. *Optica* **2020**, *7* (6), 680–686.

(66) Zhang, H.; Abhiraman, B.; Zhang, Q.; Miao, J.; Jo, K.; Roccasecca, S.; Knight, M. W.; Davoyan, A. R.; Jariwala, D.Hybrid Exciton-Plasmon-Polaritons in van Der Waals Semiconductor Gratings. *Nat. Commun.* **2020**, *11* (3552), 1–9.

(67) Zhang, X. X.; You, Y.; Zhao, S. Y. F.; Heinz, T. F.Experimental Evidence for Dark Excitons in Monolayer WSe2. *Phys. Rev. Lett.* **2015**, *115* (25), 1–6.

(68) Slobodeniuk, A. O.; Basko, D. M.Spin-Flip Processes and Radiative Decay of Dark Intravalley Excitons in Transition Metal Dichalcogenide Monolayers. *2D Mater.* **2016**, *3* (3), 035009.

(69) Zhang, X. X.; Cao, T.; Lu, Z.; Lin, Y. C.; Zhang, F.; Wang, Y.; Li, Z.; Hone,

J. C.; Robinson, J. A.; Smirnov, D.; et al.Magnetic Brightening and Control of Dark Excitons in Monolayer WSe 2. *Nat. Nanotechnol.* **2017**, *12* (9), 883–888.

(70) Molas, M. R.; Faugeras, C.; Slobodeniuk, A. O.; Nogajewski, K.; Bartos, M.; Basko, D. M.; Potemski, M.Brightening of Dark Excitons in Monolayers of Semiconducting Transition Metal Dichalcogenides. *2D Mater.* **2017**, *4* (2), 021003.

(71) Wang, G.; Robert, C.; Glazov, M. M.; Cadiz, F.; Courtade, E.; Amand, T.; Lagarde, D.; Taniguchi, T.; Watanabe, K.; Urbaszek, B.; et al.In-Plane Propagation of Light in Transition Metal Dichalcogenide Monolayers: Optical Selection Rules. *Phys. Rev. Lett.* **2017**, *119* (4), 1–7.

(72) Zhou, Y.; Scuri, G.; Wild, D. S.; High, A. A.; Dibos, A.; Jauregui, L. A.; Shu, C.; DeGreve, K.; Pistunova, K.; Joe, A. Y.; et al.Probing Dark Excitons in Atomically Thin Semiconductors via Near-Field Coupling to Surface Plasmon Polaritons. *Nat. Nanotechnol.* **2017**, *12* (9), 856–860.

(73) Lu, Z.; Rhodes, D.; Li, Z.; Tuan, D.Van; Jiang, Y.; Ludwig, J.Magnetic Field Mixing and Splitting of Bright and Dark Excitons in Monolayer MoSe 2. *2D Mater.* **2020**, *7* (015017).

(74) Molas, M. R.; Slobodeniuk, A. O.; Kazimierczuk, T.; Nogajewski, K.; Bartos, M.; Kapu, P.; Oreszczuk, K.; Watanabe, K.; Taniguchi, T.; Faugeras, C.; et al.Probing and Manipulating Valley Coherence of Dark Excitons in

Monolayer WSe 2. *Phys. Rev. Lett.* **2019**, *096803*, 1–6.

(75) Xu, Y.; Lo, T. W.; Zhang, L.; Lei, D.The Preparation, Characterization and Application of Ultra-Smooth, Low-Loss Plasmonics Noble Metal Films. *Sci. Sin. Phys. Mech. Astron.* **2019**, *49* (12), 124206.

(76) Nagpal, P.; Lindquist, N. C.; Oh, S.-H.; Norris, D. J.Ultrasmooth Patterned Metals for Plasmonics and Metamaterials. *Science (80-.).* **2014**, *594* (2009), 594–597.

(77) Mcpeak, K. M.; Jayanti, S.V; Kress, S. J. P.; Meyer, S.; Iotti, S.; Rossinelli, A.; Norris, D. J.Plasmonic Films Can Easily Be Better: Rules and Recipes. *ACS Photonics* **2015**, *2*, 326–333.

(78) Yi, M.; Shen, Z.A Review on Mechanical Exfoliation for the Scalable Production of Graphene. *J. Mater. Chem. A* **2015**, *3*, 11700–11715.

(79) Albrecht, G.; Kaiser, S.; Giessen, H.; Hentschel, M.Refractory Plasmonics without Refractory Materials. *Nano Lett.* **2017**, *17* (10), 6402–6408.

(80) Tame, M. S.; McEnery, K. R.; Özdemir, S. K.; Lee, J.; Maier, S. A.; Kim, M. S.Quantum Plasmonics. *Nat. Phys.* **2013**, *9*, 329–340.

(81) Kimble, H. J.The Quantum Internet. *Nature* **2008**, *453* (7198), 1023–1030.

(82) Sillanpää, M. A.; Park, J. I.; Simmonds, R. W.Coherent Quantum State Storage and Transfer between Two Phase Qubits via a Resonant Cavity. *Nature* **2007**, *449* (7161), 438–442.

(83) Vasilevskiy, M. I.; Santiago-Pérez, D. G.; Trallero-Giner, C.; Peres, N. M. R.; Kavokin, A.Exciton Polaritons in Two-Dimensional Dichalcogenide Layers Placed in a Planar Microcavity: Tunable Interaction between Two Bose-Einstein Condensates. *Phys. Rev. B - Condens. Matter Mater. Phys.* **2015**, *92* (24), 1–11.

(84) Nan, F.; Zhang, Y. F.; Li, X.; Zhang, X. T.; Li, H.; Zhang, X.; Jiang, R.; Wang, J.; Zhang, W.; Zhou, L.; et al.Unusual and Tunable One-Photon Nonlinearity in Gold-Dye Plexcitonic Fano Systems. *Nano Lett.* **2015**, *15* (4), 2705–2710.

(85) Thomas, R.; Thomas, A.; Pullanchery, S.; Joseph, L.; Somasundaran, S. M.; Swathi, R. S.; Gray, S. K.; Thomas, K. G.Plexcitons: The Role of Oscillator Strengths and Spectral Widths in Determining Strong Coupling. *ACS Nano* **2017**, acsnano.7b06589.

(86) Zengin, G.; Wersäll, M.; Nilsson, S.; Antosiewicz, T. J.; Käll, M.; Shegai, T.Realizing Strong Light-Matter Interactions between Single-Nanoparticle Plasmons and Molecular Excitons at Ambient Conditions. *Phys. Rev. Lett.* **2015**, *114* (15), 1–6.

(87) Stete, F.; Koopman, W.; Bargheer, M.Signatures of Strong Coupling on Nanoparticles: Revealing Absorption Anticrossing by Tuning the Dielectric Environment. *ACS Photonics* **2017**, *4* (7), 1669–1676.

(88) Liu, R.; Zhou, Z. K.; Yu, Y. C.; Zhang, T.; Wang, H.; Liu, G.; Wei, Y.;

Chen, H.; Wang, X. H.Strong Light-Matter Interactions in Single Open Plasmonic Nanocavities at the Quantum Optics Limit. *Phys. Rev. Lett.* **2017**, *118* (23), 1–6.

(89) Santhosh, K.; Bitton, O.; Chuntonov, L.; Haran, G.Vacuum Rabi Splitting in a Plasmonic Cavity at the Single Quantum Emitter Limit. *Nat. Commun.* **2016**, *7* (May), 1–5.

(90) Ramasubramaniam, A.Large Excitonic Effects in Monolayers of Molybdenum and Tungsten Dichalcogenides. *Phys. Rev. B - Condens. Matter Mater. Phys.* **2012**, *86* (11), 1–6.

(91) Withers, F.; DelPozo-Zamudio, O.; Schwarz, S.; Dufferwiel, S.; Walker, P. M.; Godde, T.; Rooney, A. P.; Gholinia, A.; Woods, C. R.; Blake, P.; et al.WSe2Light-Emitting Tunneling Transistors with Enhanced Brightness at Room Temperature. *Nano Lett.* **2015**, *15* (12), 8223–8228.

(92) Zhao, W.; Ghorannevis, Z.; Chu, L.; Toh, M.; Kloc, C.; Tan, P.-H.; Eda, G.Evolution of Electronic Structure in Atomically Thin Sheets of WS_2 and WSe_2. *ACS Nano* **2013**, *7* (1), 791–797.

(93) Echeverry, J. P.; Urbaszek, B.; Amand, T.; Marie, X.; Gerber, I. C.Splitting between Bright and Dark Excitons in Transition Metal Dichalcogenide Monolayers. *Phys. Rev. B* **2016**, *93* (12), 1–5.

(94) Park, K. D.; Jiang, T.; Clark, G.; Xu, X.; Raschke, M. B.Radiative Control

of Dark Excitons at Room Temperature by Nano-Optical Antenna-Tip Purcell Effect. *Nat. Nanotechnol.* **2017**, *13* (January), 1–6.

(95) Donnell, K. P. O.; Chen, X.; Chen, X.Temperature Dependence of Semiconductor Band Gaps Temperature Dependence of Semiconductor Band Gaps. *Appl. Phys. Lett.* **1991**, *58* (25), 2924–2926.

(96) Selig, M.; Berghäuser, G.; Raja, A.; Nagler, P.; Schüller, C.; Heinz, T. F.; Korn, T.; Chernikov, A.; Malic, E.; Knorr, A.Excitonic Linewidth and Coherence Lifetime in Monolayer Transition Metal Dichalcogenides. *Nat. Commun.* **2016**, *7* (May).

(97) Moody, G.; Kavir Dass, C.; Hao, K.; Chen, C. H.; Li, L. J.; Singh, A.; Tran, K.; Clark, G.; Xu, X.; Berghäuser, G.; et al.Intrinsic Homogeneous Linewidth and Broadening Mechanisms of Excitons in Monolayer Transition Metal Dichalcogenides. *Nat. Commun.* **2015**, *6* (May), 1–6.

(98) Liu, M.; Pelton, M.; Guyot-Sionnest, P.Reduced Damping of Surface Plasmons at Low Temperatures. *Phys. Rev. B - Condens. Matter Mater. Phys.* **2009**, *79* (3), 1–5.

(99) Zheng, D.; Zhang, S.; Deng, Q.; Kang, M.; Nordlander, P.; Xu, H.Manipulating Coherent Plasmon-Exciton Interaction in a Single Silver Nanorod on Monolayer WSe2. *Nano Lett.* **2017**, *17* (6), 3809–3814.

(100) Lundt, N.; Klembt, S.; Cherotchenko, E.; Betzold, S.; Iff, O.; Nalitov, A.V.;

Klaas, M.; Dietrich, C. P.; Kavokin, A.V.; Höfling, S.; et al.Room-Temperature Tamm-Plasmon Exciton-Polaritons with a WSe2monolayer. *Nat. Commun.* **2016**, *7*.

(101) Cuadra, J.; Baranov, D. G.; Wersäll, M.; Verre, R.; Antosiewicz, T. J.; Shegai, T.Observation of Tunable Charged Exciton Polaritons in Hybrid Monolayer WS2 $-$ Plasmonic Nanoantenna System. *Nano Lett.* **2017**, 1–31.

(102) Wang, S.; Li, S.; Chervy, T.; Shalabney, A.; Azzini, S.; Orgiu, E.; Hutchison, J. A.; Genet, C.; Samorì, P.; Ebbesen, T. W.Coherent Coupling of WS $_2$ Monolayers with Metallic Photonic Nanostructures at Room Temperature. *Nano Lett.* **2016**, *16* (7), 4368–4374.

(103) Wen, J.; Wang, H.; Wang, W.; Deng, Z.; Zhuang, C.; Zhang, Y.; Liu, F.; She, J.; Chen, J.; Chen, H.; et al.Roomerature Strong Light-Matter Interaction with Active Control in Single Plasmonic Nanorod Coupled with Two-Dimensional Atomic Crystals. *Nano Lett.* **2017**, *17* (8), 4689–4697.

(104) Liu, W.; Lee, B.; Naylor, C. H.; Ee, H. S.; Park, J.; Johnson, A. T. C.; Agarwal, R.Strong Exciton-Plasmon Coupling in MoS2Coupled with Plasmonic Lattice. *Nano Lett.* **2016**, *16* (2), 1262–1269.

(105) Lundt, N.; Maryński, A.; Cherotchenko, E.; Pant, A.; Fan, X.; Tongay, S.; Sęk, G.; Kavokin, A.V; Höfling, S.; Schneider, C.Monolayered MoSe $_2$: A Candidate for Room Temperature Polaritonics. *2D Mater.* **2016**, *4* (1),

015006.

(106) Zhang, C.; Wang, H.; Chan, W.; Manolatou, C.; Rana, F.Absorption of Light by Excitons and Trions in Monolayers of Metal Dichalcogenide Mo S2: Experiments and Theory. *Phys. Rev. B - Condens. Matter Mater. Phys.* **2014**, *89* (20), 12–16.

(107) Feist, J.; Garcia-Vidal, F. J.Extraordinary Exciton Conductance Induced by Strong Coupling. *Phys. Rev. Lett.* **2015**, *114* (19), 1–5.

(108) Mollow, B.Power Spectrum of Light Scattered by Two-Level Systems. *Phys. Rev.* **1969**, *188* (5), 1969–1975.

(109) Mollow, B. R.Absorption and Emission Line-Shape Functions for Driven Atoms. *Phys. Rev. A* **1972**, *5* (3), 1522–1527.

(110) Gao, W.; Lee, Y. H.; Jiang, R.; Wang, J.; Liu, T.; Ling, X. Y.Localized and Continuous Tuning of Monolayer MoS2 Photoluminescence Using a Single Shape-Controlled Ag Nanoantenna. *Adv. Mater.* **2016**, *28*, 701–706.

(111) Yip, C. T.; Lo, T. W.; Zhu, S.; Jia, G. Y.; Sun, H.; Lam, C.; Lei, D.Tight-Binding Modeling of Excitonic Response in van Der Waals Stacked 2D Semiconductors. *Nanoscale Horizons* **2019**, *4*, 969–974.

(112) Splendiani, A.; Sun, L.; Zhang, Y.; Li, T.; Kim, J.; Chim, C. Y.; Galli, G.; Wang, F.Emerging Photoluminescence in Monolayer MoS2. *Nano Lett.* **2010**, *10* (4), 1271–1275.

(113) Amani, M.; Lien, D.; Kiriya, D.; Xiao, J.; Azcatl, A.; Noh, J.; Madhvapathy, S. R.; Addou, R.; Dubey, M.; Cho, K.; et al.Near-Unity Photoluminescence Quantum Yield in MoS 2. *Science (80-.).* **2015**, *350* (6264).

(114) Chikkaraddy, R.; Zheng, X.; Benz, F.; Brooks, L. J.; Nijs, B.De; Carnegie, C.; Kleemann, M.; Mertens, J.; Bowman, R. W.; Vandenbosch, G. A. E.; et al.How Ultranarrow Gap Symmetries Control Plasmonic Nanocavity Modes: From Cubes to Spheres in the Nanoparticle-on-Mirror. *ACS Photonics* **2017**, *4*, 469–475.

(115) Li, G. C.; Zhang, Y. L.; Jiang, J.; Luo, Y.; Lei, D. Y.Metal-Substrate-Mediated Plasmon Hybridization in a Nanoparticle Dimer for Photoluminescence Line-Width Shrinking and Intensity Enhancement. *ACS Nano* **2017**, *11* (3), 3067–3080.

(116) Online, V. A.Effects of Surface Roughness of Ag Thin Films on Surface-Enhanced Raman Spectroscopy of Graphene : Spatial Nonlocality and Physisorption. *Nanoscale* **2014**, *6*, 1311–1317.

(117) Smoleński, T.; Kazimierczuk, T.; Goryca, M.; Wojnar, P.; Kossacki, P.Mechanism and Dynamics of Biexciton Formation from a Long-Lived Dark Exciton in a CdTe Quantum Dot. *Phys. Rev. B - Condens. Matter Mater. Phys.* **2015**, *91* (15), 155430.

(118) Combescot, M.; Betbeder-Matibet, O.; Combescot, R.Bose-Einstein Condensation in Semiconductors: The Key Role of Dark Excitons. *Phys.*

Rev. Lett. **2007**, *99* (17), 176403.

(119) Poem, E.; Kodriano, Y.; Tradonsky, C.; Lindner, N. H.; Gerardot, B. D.; Petroff, P. M.; Gershoni, D.Accessing the Dark Exciton with Light. *Nat. Phys.* **2010**, *6* (12), 993–997.

(120) Barbone, M.; Montblanch, A. R.; Kara, D. M.; Palacios-berraquero, C.; Cadore, A. R.; Fazio, D.De; Pingault, B.; Mostaani, E.; Li, H.; Chen, B.; et al.Charge-Tuneable Biexciton Complexes in Monolayer WSe2. *Nat. Commun.* **2018**, *9* (3721).

(121) You, Y.; Zhang, X.; Berkelbach, T. C.; Hybertsen, M. S.; Reichman, D. R.; Heinz, T. F.Observation of Biexcitons in Monolayer WSe2. *Nat. Phys.* **2015**, *11* (June), 477–482.

(122) Ye, Z.; Waldecker, L.; Ma, E. Y.; Rhodes, D.; Antony, A.; Kim, B.; Zhang, X.; Deng, M.; Jiang, Y.; Lu, Z.; et al.Efficient Generation of Neutral and Charged Biexcitons in Encapsulated WSe2 Monolayers. *Nat. Commun.* **2018**, *9* (3718).

(123) Robert, C.; Amand, T.; Cadiz, F.; Lagarde, D.; Courtade, E.; Manca, M.; Taniguchi, T.; Watanabe, K.; Urbaszek, B.; Marie, X.Fine Structure and Lifetime of Dark Excitons in Transition Metal Dichalcogenide Monolayers. *Phys. Rev. B* **2017**, *96* (155423), 1–8.

(124) Peng, G.; Lo, P.; Li, W.; Huang, Y.; Chen, Y.; Lee, C.; Yang, C.; Cheng,

S.Distinctive Signatures of the Spin- and Momentum-Forbidden Dark Exciton States in the Photoluminescence of Strained WSe2 Monolayers under Thermalization. *Nano Lett.* **2019**, *19*, 2299–2312.

(125) Moody, G.; Tran, K.; Lu, X.; Autry, T.; Fraser, J. M.; Mirin, R. P.; Yang, L.; Li, X.; Silverman, K. L.Microsecond Valley Lifetime of Defect-Bound Excitons in Monolayer WSe2. *Phys. Rev. Lett.* **2018**, *121* (5), 57403.

(126) Yang, J.; Hugonin, J.; Lalanne, P.Near-to-Far Field Transformations for Radiative and Guided Waves. *ACS Photonics* **2016**, *3*, 395–402.